

Explicit habit-prediction in the Lagrangian super-particle ice microphysics model McSnow

Jan-Niklas Welss¹, Christoph Siewert², and Axel Seifert²

¹Johannes Gutenberg Universität Mainz

²Deutscher Wetterdienst

June 7, 2023

Abstract

The Monte-Carlo ice microphysics model McSnow is extended by an explicit habit prediction scheme, combined with the hydrodynamic theory of \citeauthor{Boehm1992a}.

\citeauthor{Boehm1992a}'s original cylindrical shape assumption for prolates is compared against recent lab results, showing that interpolation between cylinder and prolate yields the best agreement.

For constant temperature and supersaturation, the predicted mass, size, and density agree well with the laboratory results, and a comparison with real clouds using the polarizability ratio shows regimes capable of improvement.

An updated form of the inherent growth function to describe the primary habit growth tendencies is proposed and combined with a habit-dependent ventilation coefficient.

The modifications contrast the results from general mass size relations and significantly impact the main ice microphysical processes. Depending on the thermodynamic regime, ice habits significantly alter depositional growth and affect aggregation and riming.

1 **Explicit habit-prediction in the Lagrangian**
2 **super-particle ice microphysics model McSnow**

3 **Jan-Niklas Welss^{1,2}, C. Siewert¹, A. Seifert¹**

4 ¹Deutscher Wetterdienst, Frankfurt, Germany

5 ²Institute for Atmospheric Physics, Johannes Gutenberg University Mainz, Mainz, Germany

6 **Key Points:**

- 7 • McSnow is extended by an explicit habit prediction including the revision of cor-
8 responding parameterizations.
9 • A new inherent growth ratio overcoming existing deficiencies is proposed.
10 • The impact of the modifications on the depositional growth, aggregation, and rim-
11 ing is shown for two distinct case studies.

Corresponding author: Jan-Niklas Welss, jwelss@uni-mainz.de

Abstract

The Monte-Carlo ice microphysics model McSnow is extended by an explicit habit prediction scheme, combined with the hydrodynamic theory of Böhm. Böhm’s original cylindrical shape assumption for prolates is compared against recent lab results, showing that interpolation between cylinder and prolate yields the best agreement. For constant temperature and supersaturation, the predicted mass, size, and density agree well with the laboratory results, and a comparison with real clouds using the polarizability ratio shows regimes capable of improvement. An updated form of the inherent growth function to describe the primary habit growth tendencies is proposed and combined with a habit-dependent ventilation coefficient. The modifications contrast the results from general mass size relations and significantly impact the main ice microphysical processes. Depending on the thermodynamic regime, ice habits significantly alter depositional growth and affect aggregation and riming.

Plain Language Summary

The McSnow model was extended to predict the shape of ice crystals. A comparison of the falling behavior of modeled and 3D-printed ice crystals shows a discrepancy that can be improved by interpolation. At constant temperature and supersaturation, simulated crystal properties agree well with laboratory results, and by comparison to real clouds, we have updated the function to describe growth tendencies. Ice shape is shown to have a significant influence on the main microphysical processes.

1 Introduction

Inside clouds, atmospheric conditions are highly variable, often containing gaseous, liquid, and frozen water simultaneously in spatial and temporal heterogeneity (e.g. Morrison et al., 2012). The complex transitions involving all three phases are challenging when trying to describe and understand the microphysical processes within mixed-phase clouds (Morrison et al., 2020). Interactions involving ice crystals are tricky because of the variety of possible shapes. These habit characteristics are critical for the cold phase microphysical processes that influence sedimentation, deposition/sublimation, riming, aggregation, and especially radiative properties. Specialized observational methods to gather information on the rates of ice-microphysical processes are constantly being developed and improved, ranging from ground and in-situ (e.g. Field et al., 2004; Locatelli & Hobbs, 1974) to remote sensing observations (e.g. Dias Neto et al., 2019; Tridon et al., 2019). Classification and categorization of observed ice particles is an ongoing task (Bailey & Hallett, 2009; Kikuchi et al., 2013). This helps to link the occurrence of ice crystal types to specific atmospheric conditions. While these efforts provide data sets covering a variety of variables, they only partially allow attribution of effects to individual processes. Laboratory measurements such as Takahashi et al. (1991) or Connolly et al. (2012) allow process isolation, but lack representation of the full range of atmospheric conditions and especially the transition from isolation to a fully interactive system. As a result, the resulting physical descriptions can become highly specialized and are often only generalizable by assuming certain atmospheric conditions or categorizing ice habit, introducing artificial thresholds. The challenge posed by individual growth histories under changing conditions is to describe the variety of simple (columns, plates) and more complex (branched and polycrystalline) ice habits coexisting with aggregates composed of crystals of different shapes and numbers. Mass-size and mass-area relations may be able to describe the average geometry of certain ice habits (Mitchell, 1996; Auer & Veal, 1970; Um et al., 2015), but cannot represent the natural variety and transitions due to the use of thresholds. Overcoming the threshold between ice categories to allow a natural transition is a goal of modern microphysical schemes (Morrison & Grabowski, 2008; Milbrandt et al., 2021). Previous studies show that it is generally beneficial to explicitly resolve habit

62 development to improve the microphysical representation of ice in models: Jensen et al.
 63 (2017) show an effect of ice habit on the spatial precipitation pattern, Hashino and Tripoli
 64 (2007) find that dendrites extend dendritic growth regions further than atmospheric condi-
 65 tions suggest, and Sulia and Harrington (2011) conclude that the absence of ice habit
 66 underestimates ice growth and cloud glaciation time. Also, only models that resolve the
 67 evolving crystal shapes can make use of the wealth of data provided by radar polarime-
 68 try (Trömel et al., 2021) and combine the approaches to identify gaps in the interpre-
 69 tation of observations as well as in the microphysical descriptions when modeling clouds
 70 and precipitation (von Terzi et al., 2022).

71 To fully evaluate the effects of dynamically developing habits, detailed descriptions
 72 of processes at the particle level are needed. The approach of J.-P. Chen and Lamb (1994b)
 73 simplifies the ice habits of individual crystals as porous spheroids. The scheme predicts
 74 the shape and density of ice particles, helping to depict the natural evolution of ice habits
 75 and minimizing artificial type classification. While no natural crystal resembles a spheroid,
 76 Jayaweera and Cottis (1969) show that spheroids are suitable for representing colum-
 77 nar or plate-like ice crystals. However, even a simplified geometry requires changes in
 78 the process description: Vapor growth depends crucially on the particle shape, which af-
 79 fects the water vapor field around the particle. The theoretical framework of Böhm al-
 80 lows the consideration of ice habits for fall speed and collision effects based on spheroids
 81 (Böhm, 1989, 1992a, 1992b, 1992c, 1994, 1999). Based on investigations for oblates (Pitter
 82 et al., 1974), Hall and Pruppacher (1976) deduce that the ventilation is independent or
 83 only slightly dependent on the particle shape, but recent results suggest that this assump-
 84 tion underestimates the ventilation for prolate particles of larger sizes (Wang and Ji (2000),
 85 Ke et al. (2018) and others). For the collision of ice crystals with droplets, the results
 86 of Wang and Ji (2000) suggest the existence of preferred riming regions depending on
 87 the Reynolds number, which are difficult to represent in the spheroidal approach. Jensen
 88 and Harrington (2015) propose a way to distribute rime on the particle surface perpen-
 89 dicular to the flow in an effort to evaluate the effect of ice habits on the onset of rim-
 90 ing.

91 The likelihood of ice crystal aggregation is enhanced by non-spherical geometry mod-
 92 els because an increased cross-sectional area is a direct factor. However, it is difficult to
 93 describe the geometry of the resulting aggregates because of the many degrees of free-
 94 dom involved in the collision event. Several descriptions attempt to characterize the ge-
 95 ometry of aggregates after collisions (J.-P. Chen & Lamb, 1994a; Shima et al., 2020; Gavze
 96 & Khain, 2022) but a general and accurate parameterization is not yet available.

97 This paper presents the results of the extension of the Monte Carlo ice microphysics
 98 model *McSnow* Brdar and Seifert (2018) by an explicit habit prediction (HP) scheme
 99 using porous spheroids following J.-P. Chen and Lamb (1994b, CL94) and Jensen and
 100 Harrington (2015, JH15) to replace the classical m - D relations. The model uses the com-
 101 plete theoretical framework of Böhm, allowing the consideration of ice habits for fall ve-
 102 locity and collision effects (Sec. 2.2). We show that the original shape assumption for pro-
 103 lates underestimates the fall velocity derived from recent laboratory studies, and pro-
 104 vide an interpolation to overcome the observed mismatch (Sec. 3.1). The original formu-
 105 lation of the ventilation effect (Hall & Pruppacher, 1976) is extended to include a habit-
 106 specific ventilation effect suggested by several studies. We evaluate the performance of
 107 the habit prediction scheme against laboratory results and polarimetric observations, and
 108 propose several changes to overcome identified deficiencies. These include changes to the
 109 Inherent Growth Function (IGF) and the plate branching criterion. For the full model,
 110 we present the effects of explicit habit formation on deposition, riming, and aggregation
 111 in a 1-D snow shaft setup (Sec. 5).

112 2 Habit dependence of microphysical processes

113 This section describes the extensions of *McSnow* (Brdar & Seifert, 2018) regard-
 114 ing the habit prediction scheme, including necessary changes and clarifications encom-
 115 passed by an explicit ice morphology.

116 2.1 Habit prediction

In nature, the geometry and internal structure of ice particles can reach a high de-
 gree of complexity that defies any explicit description. A common approach is the use
 of z axis symmetric spheroids based on the two defining semi-axes a (equatorial) and c
 (polar radius). We can assume that the approximation of oblate and prolate spheroids
 for the two dominant primary habits of plates and columns is superior to fixed mass-size
 (m - D), mass-area (m - A), and size-density (D - ρ) relations because this removes the need
 for categorization of crystal and allows the transition between ice shapes to be consid-
 ered. The aspect ratio ϕ (ratio of polar to equatorial radius) describes the shape of the
 spheroid

$$\phi = \frac{c}{a}, \quad (1)$$

$$V_i = \frac{4}{3}\pi a^3 \phi = \frac{4}{3}\pi a^2 c, \quad (2)$$

$$\rho_{\text{app}} = \frac{m_i}{V_i}. \quad (3)$$

117 To account for possible secondary habit effects such as branching and hollowing, we use
 118 the ice volume V_i and the apparent density ρ_{app} . With the introduction of explicit par-
 119 ticle geometry, the shape changing processes must be adjusted, including vapor depo-
 120 sition, riming, and aggregation. Based on the results of J. Nelson (1998) and Harrington
 121 et al. (2019), we assume that the aspect ratio remains unchanged during sublimation.
 122 Mitra et al. (1990) and Kintea et al. (2015) find a similar behavior for melting, but the
 123 question remains whether water fills gaps revealed by branched or rimed structures, pos-
 124 sibly changing the density of the particles but not necessarily their shape.

125 2.1.1 Deposition/Sublimation

The equation for mass change through vapor deposition and sublimation,

$$\left(\frac{dm_i}{dt}\right)_v = 4\pi C D_v f_v \frac{p_{\text{vap}} - p_{\text{sat},i}}{R_v T} \left(1 + \frac{L_s^2 D_v p_{\text{sat},i}}{K_d R_v^2 T^3}\right)^{-1}, \quad (4)$$

126 considers the shape information mainly via the capacitance C . The other variables are
 127 the vapor diffusivity D_v , the ventilation coefficient f_v , the vapor pressure p_{vap} , the sat-
 128 uration pressure with respect to ice $p_{\text{sat},i}$, as well as the temperature T , the gas constant
 129 of water vapor R_v , the latent heat of sublimation L_s , and the thermal conductivity of
 130 dry air K_d . While J. T. Nelson and Baker (1996) show that the classical capacitance model
 131 cannot evolve faceted crystals because of inconsistent surface boundary conditions, it still
 132 produces relatively accurate estimates for mass and shape evolution. Still, Westbrook
 133 et al. (2008) show that the actual capacitance might depend on the internal structure
 134 of the hydrometeor, eventually causing an overestimation of capacitance for hydrome-
 135 teors of reduced density when using the original formulation of CL94.

Kobayashi (1961) shows that the evolution of primary habits (planar or columnar)
 depends mainly on ambient temperature, while that of secondary habits (branching and
 hollowing) depends on supersaturation. To quantify the temperature regimes favoring
 certain geometries, CL94 derive an inherent growth function Γ (IGF) by collecting labo-
 ratory and in-situ measurements for the temperature range between 0° and -30°C (re-
 spectively $243 - 273\text{K}$) by relating individual growth along the two major axes

$$\Gamma(T) = \frac{d \ln c}{d \ln a}. \quad (5)$$

The change in crystal mass causes an ice volume change

$$dV_i = \frac{1}{\rho_{\text{depo.}}} dm_i , \quad (6)$$

with the deposition density $\rho_{\text{depo.}}$. The spheroid shape does not explicitly allow for secondary habits. To capture branching and hollowing, the volume of the circumscribing spheroid is modified. Physically, the air inside the spheroid lowers the apparent density below ice density. J.-P. Chen and Lamb (1994b) use an empirical formulation for the deposition density based on experimental results of Fukuta (1969). We prefer the direct parameterization of the deposition density using the IGF proposed by Jensen and Harrington (2015, JH15)

$$\rho_{\text{depo}} = \begin{cases} \rho_i \Gamma(T) & , \quad \Gamma < 1 , \\ \rho_i \Gamma^{-1}(T) & , \quad \Gamma \geq 1 . \end{cases} \quad (7)$$

136 For oblates ($\phi < 1$), branching happens only if $v a > \pi D_v c$ (JH15), otherwise $\rho_{\text{depo}} =$
137 ρ_i . For prolates, hollowing happens immediately.

138 Using the same deposition density of branching/hollowing for sublimation may lead
139 to unphysical apparent densities because the IGF is only valid for temperature and su-
140 persaturation during the deposition process. Laboratory measurements suggest that ice
141 particles preserve their shape during sublimation, maintaining a constant aspect ratio
142 (Harrington et al., 2019; J. Nelson, 1998). We use the apparent density for particles un-
143 dergoing sublimation ($\rho_{\text{depo}} = \rho_{\text{app}}$).

Following CL94, we can predict the change in aspect ratio using the IGF

$$d \ln \phi = \frac{\Gamma - 1}{\Gamma + 2} d \ln V_i . \quad (8)$$

144 The evolution of V_i follows from Eqs. (4) and (6). As in previous work (Korolev & Isaac,
145 2003; Lawson et al., 2008; Baran, 2012), we restrict habit development for now to oc-
146 cur only for particles larger than $D \geq 10 \mu m$, since observations suggest that crystals
147 up to this size are approximately spherical.

The ice habit also affects the airflow around the particle and ventilation. The parts of the crystal surface that extend farthest into the flow experience the greatest effect due to increased water vapor advection (J.-P. Chen & Lamb, 1994b). Hall and Pruppacher (1976) suggest a description of the ventilation coefficient by

$$f_v = b_1 + b_2 X_{v,\text{equiv}}^\gamma , \quad (9)$$

the constants b_1 , b_2 , and γ have been generalized from observations for spheres and plates as

$$\begin{array}{llll} b_1 = 1.0, & b_2 = 0.14, & \gamma = 2 & \text{for } X_{v,\text{equiv}} \leq 1 , \\ b_1 = 0.86, & b_2 = 0.28, & \gamma = 1 & \text{for } X_{v,\text{equiv}} > 1 . \end{array}$$

The proposed ventilation is a function of Schmidt N_{Sc} and Reynolds number $N_{\text{Re,equiv}}$

$$X_{v,\text{equiv}} = N_{\text{Sc}}^{\frac{1}{3}} N_{\text{Re}}^{\frac{1}{2}} , \quad (10)$$

$$N_{\text{Sc}} = \frac{\mu_a}{\rho_a D_v} , \quad (11)$$

$$N_{\text{Re,equiv}} = \frac{d_{\text{equiv}} v_t \rho_a}{\mu_a} . \quad (12)$$

The dynamic viscosity μ_a can be described by Sutherland's Law (Sutherland, 1893)

$$\mu_a(T) = \mu_0 \frac{T_0 + T_S}{T + T_S} \left(\frac{T}{T_0} \right)^{3/2} , \quad (13)$$

148 with $\mu_0 = 1.716 \times 10^{-5}$, the melting/freezing point $T_0 = 273.15$ K, and the Suther-
 149 land temperature $T_S = 110.4$ K. The other variables are the air density ρ_a , the volume-
 150 equivalent diameter of a sphere d_{equiv} , and the terminal velocity v_t . Pruppacher and Klett
 151 (1997) collected habit-specific solutions for selected N_{Re} -regimes, but no continuous de-
 152 scription for all habits is known to the authors. We propose a habit-dependent formu-
 153 lation based on several numerical studies in Section 4.1.

Ventilation affects the geometric evolution by favoring the edges of the crystals. To account for this effect, we replace the IGF of Eq. 8 by the ventilation-influenced growth habit Γ^* as proposed by CL94

$$\Gamma^* = \Gamma f^* , \quad (14)$$

where the ratio of the local ventilation coefficients f^* of the respective axis (f_c, f_a)

$$f^* = \frac{f_c}{f_a} \approx \frac{b_1 + b_2 X^\gamma \left(\frac{c}{r_0}\right)^{1/2}}{b_1 + b_2 X^\gamma \left(\frac{a}{r_0}\right)^{1/2}} , \quad (15)$$

154 is used instead of the overall ventilation coefficient f_v . The local ventilation coefficient
 155 compares the local axis dimension to the radius of a sphere r_0 with the same volume.

The maximum dimension is defined as $D = 2 \max(a, c)$. We distinguish between the projected area A , which is relevant for riming and collision processes, and the hydrodynamic area \tilde{A} . The geometric area A of a spheroid is defined as the circumscribing ellipse

$$\begin{aligned} A_{\text{prolate}} &= \pi a c && \text{for prolates,} \\ A_{\text{oblate}} &= \pi a^2 && \text{for oblates,} \end{aligned} \quad (16)$$

while the cross-sectional area \tilde{A} is the effective area presented to the flow (cf. Böhm (1989)). JH15 suggest a linear dependency on ϕ and ρ_{app} to link the degree of branching to the thickness of a plate

$$\begin{aligned} \tilde{A} &= \xi A \\ \xi &= (1 - \phi) \left(\frac{\rho_{\text{app}}}{\rho_i} \right) + \phi && \text{for oblates,} \\ \xi &= 1 && \text{for prolates.} \end{aligned} \quad (17)$$

156 A decrease in cross-sectional area represents flow through the porous structures of the
 157 particle, which in turn reduces flow resistance. Prolates are assumed to be hollow inwards,
 158 so the cross-sectional area is effectively unaffected ($A = \tilde{A}$). In terms of collision prob-
 159 ability, we will see that the theory of Böhm uses boundary layer theory, explicitly con-
 160 sidering the difference between geometric and cross-sectional area via the area ratio q
 161 (cf. Eq. 23), which is similar to ξ above.

162 2.1.2 *Riming*

The distribution of rime along the two major axes is a critical factor in the prediction of ice crystal habit. We assume that particles fall with their largest cross-sectional area perpendicular to the flow, so that rime is always added to the minor axis while preserving the maximum dimension, transforming the habit of the particle towards a quasi-spherical shape. Jensen and Harrington (2015) refer to the work of A. J. Heymsfield (1978) for observations of the aspect ratio of graupel and propose that this quasi-spherical shape translates into an aspect ratio of $\phi = 0.8$ for plates or equivalently $\phi = 1/0.8 = 1.25$ for columns. For prolates with an aspect ratio between $1 < \phi \leq 1.25$, the updated equatorial radius a can be described as

$$a = \sqrt{\frac{V_{\text{tot}} + \frac{\Delta m_{\text{rime}}}{\rho_{\text{rime}}}}{\frac{4\pi}{3} c}} , \quad (18)$$

with V_{tot} the total volume before riming. Analogous, for oblate particles with $0.8 < \phi \leq 1$

$$c = \frac{V_{\text{tot}} + \frac{\Delta m_{\text{rime}}}{\rho_{\text{rime}}}}{\frac{4\pi}{3} a^2} . \quad (19)$$

The choice of a quasi-spherical aspect ratio threshold can lead to an oscillation around these values if simultaneous depositional growth supports the development of a more pronounced habit. These oscillations can be interpreted as a tumbling of the graupel particle, so that the newly added mass is randomly added to one of the axes.

We combine habit prediction with the stochastic riming approach of *McSnow*, introduced by Seifert et al. (2019), since it incorporates the shape properties of the particle into the collision probability using the theory of Böhm via the Stokes number (cf. Sec. 2.2.2). To better understand the feedback between habit information and collision probability, we will take a closer look at the implications of the shape dependence of the collision kernel.

2.1.3 Aggregation

For aggregates, we rely on the diagnostic geometry introduced by Brdar and Seifert (2018) following the empirical power laws for the mass-size-relation of aggregates (Mitchell, 1996, S3: Aggregates of Side Planes, Columns, and Bullets). The formulation and implementation of a more advanced aggregation framework that takes into account the habits and properties of the colliding particles in a self-consistent manner is left for future work (J.-P. Chen & Lamb, 1994a; Shima et al., 2020; Gavze & Khain, 2022). For small numbers of monomers ($N_m < 10$), we expect that this rather simple empirical approach may lead to errors in the estimation of particle properties (Karrer et al., 2021) compared to the explicit ideas above. The approach does not describe the transition from aggregates defined by the shape of a few individual monomer habits to those consisting of many particles.

To describe the aggregation of hydrometeors, we use the Monte-Carlo algorithm of Shima et al. (2009). When using an explicit habit prediction, aggregates and the assumption about the geometry term of the collision kernel K must be taken into account. In classical m - D - and m - A -relations, the maximum dimension D is used to estimate the geometry term (D -Kernel)

$$K_D = \pi \left(\frac{D_1}{2} + \frac{D_2}{2} \right)^2 S E_c |v_1 - v_2| = \pi (r_1 + r_2)^2 S E_c |v_1 - v_2| , \quad (20)$$

where S is the sticking efficiency, E_c is the collision efficiency (see Sec. 2.2.2), and v_n is the terminal fall velocity of the individual particles. The formulation is neutral for the treatment of oblates, but may overestimate the actual collision cross section of a prolate. An alternative is the A -Kernel (Böhm, 1994; Connolly et al., 2012; Karrer et al., 2021), which uses the equivalent radius $r_{n,\text{eq}} = \sqrt{A_n \pi^{-1}}$

$$K_A = \pi \left(\sqrt{A_1 \pi^{-1}} + \sqrt{A_2 \pi^{-1}} \right)^2 S E_c |v_1 - v_2| = \pi (r_{1,\text{eq}} + r_{2,\text{eq}})^2 S E_c |v_1 - v_2| . \quad (21)$$

The overestimation can be determined by the ratio of the maximum dimension of the prolates D_{max} to the equivalent diameter $D_{n,\text{eq}}$ and is proportional to

$$\frac{D_{\text{max}}}{D_{n,\text{eq}}} = \frac{2c}{2\sqrt{A_n \pi^{-1}}} = \frac{c}{\sqrt{a c}} = \sqrt{\frac{c}{a}} = \sqrt{\phi} . \quad (22)$$

We favor the use of the A -kernel when using the habit prediction scheme.

2.2 Review of Boehm's terminal velocity and collision efficiency parameterization

The work of Böhm comprises several publications, making it difficult to extract the parameterizations for terminal velocity and collision efficiency from his original work (Böhm,

190 1989, 1992a, 1992b, 1992c, 1994, 1999). Therefore, we review and summarize his work
 191 and its application to habit prediction. Since Böhm (2004) advised to use the original
 192 equations because they compare better with numerical simulations and field observations,
 193 we exclude the revision of Posselt et al. (2004).

194 **2.2.1 Terminal velocity**

195 The terminal velocity scheme is important for particles with different shapes and
 196 directly affects the depositional growth and the collision kernel. Böhm’s parameteriza-
 197 tion is a generalized and complete framework that makes the following necessary assump-
 198 tions

- 199 • The maximum dimension is oriented in the horizontal plane, as shown for exam-
 200 ple by Westbrook and Sephton (2017) for all simple geometries studied.
- The porosity p in the theory of Böhm is related to the ratio of the cross-sectional
 area \tilde{A} to the circumscribing ellipsis area A_{ce} . It represents the internal structure
 of ice crystals caused by secondary habits

$$p = 1 - q, \quad q = \frac{\tilde{A}}{A_{ce}}. \quad (23)$$

201 The ratio q is not to be confused with the area ratio $A_r = \tilde{A} A_{cc}^{-1}$ which A. J. Heyms-
 202 field and Westbrook (2010) and McCorquodale and Westbrook (2021) define as
 203 the ratio of the cross-sectional area to the circumscribing circle A_{cc} .

- Böhm (1992a) argues that the hydrodynamic behavior of prolate particles is sim-
 ilar to that of cylinders. He suggests

$$q = \frac{4}{\pi} \quad \text{for } \phi > 1.$$

204 This approximation is discussed in detail in Section 3.1.

- 205 • We add the assumption that all particles accelerate immediately to their termi-
 206 nal velocity. See, e.g., Naumann and Seifert (2015) for an alternative approach that
 207 attempts to account for deviations from the terminal fall velocity.

208 Böhm’s parameterization is valid for solid and liquid hydrometeors and is based on a func-
 209 tional dependence of the drag coefficient on the Reynolds number derived from Bound-
 210 ary Layer Theory (BLT). The terminal velocity follows the definition of the Reynolds
 211 number. Both the Reynolds number and the drag coefficient are modified by the aspect
 212 ratio via the Best number (see Eq. A1).

213 Böhm (1992a) showed that the formula is consistent with viscous theory, and by
 214 matching the results from BLT with Oseen’s theory (Oseen, 1927), there is good agree-
 215 ment of inertial drag at low Reynolds numbers. Böhm (1992a) claims that the errors are
 216 generally on the order of $\epsilon \leq 10\%$ for $0 < N_{Re} < 5 \times 10^5$ for the hydrometeor types
 217 studied (raindrops, columnar and planar ice crystals, rimed and unrimed aggregates, var-
 218 ious types of graupel, and hail). The complete parameterization of the fall velocity can
 219 be found in the appendix A1.

220 **2.2.2 Collision efficiency**

Generally, the collision efficiency E_c is defined as the ratio of the actual collision
 cross section to the geometric one (Pruppacher & Klett, 1997)

$$E_c = \frac{x_c^2}{(r_1 + r_2)^2} = \frac{y_s}{\delta}, \quad (24)$$

where x_c is the initial horizontal offset and r_n is the radius of the interacting particles.
 Böhm (1992b) states that the collision efficiency for axisymmetric particles can be de-
 scribed by the ratio of the stop distance of the collected particle y_s and the boundary

layer thickness of the collecting particle δ . For non-axisymmetric particles, the collision efficiency derivation is extended to a generalized form (Böhm, 1992c)

$$E_c = \left(\frac{y_s}{\delta} \right)^{2/j}, \quad (25)$$

with $j = 1$ for a two-dimensional flow (around the prolate) and $j = 2$ for the axisymmetric case. The boundary layer thickness δ can be calculated by

$$\delta = \delta_0 \frac{r}{\sqrt{N_{\text{Re}} \Gamma_\phi}}, \quad (26)$$

221 with $\delta_0 = 3.60$ for oblates and $\delta_0 = 4.54$ for prolates. The habit specific function Γ_ϕ
 222 can be found in the Appendix (Eq. A1c).

By replacing the individual boundary layer by the sum of the boundary layers of the colliding particles and integrating the differential equation from the initial velocity (detailed analysis in the dissertation (Böhm, 1990)), Böhm finds the collision efficiency for the resulting two-body system as

$$E_c = \begin{cases} [H \ln(\cosh \frac{F}{H} + \frac{1+G}{F} \sinh \frac{F}{H}) - G]^{2/j}, & (\frac{F}{H} < 10), \\ H \ln(\frac{F+G}{2F}) + F - G, & (\frac{F}{H} \geq 10). \end{cases} \quad (27)$$

223 The details of the variables used can be found in A2.

To account for the contribution of the surrounding non-frictional flow, Böhm added an approximate analytical solution based on potential flow theory (cf. Böhm (1994)). This extension aims at improving the asymptotic behavior for low Reynolds numbers $N_{\text{Re}} \lesssim 1$. With this modification, the total collision efficiency E is the product of the collision efficiency according to BLT E_c (from above) and the contribution from potential flow theory E_p

$$E = E_c E_p = \begin{cases} E_c \left[\left(\cosh \frac{\Delta_x t_\delta}{c_x} + \frac{1}{\Delta_x} \sinh \frac{\Delta_x t_\delta}{c_x} e^{-t_\delta/c_x} \right) \right]^{-j}, & (b c_y \geq 1), \\ E_c \left[\left(\frac{2 \Delta_x}{1+\Delta_x} e^{-(\Delta_x-1) t_\delta/c_x} \right) \right]^j, & (b c_y \leq 1). \end{cases} \quad (28)$$

224 The full formulations of the variables used in Eq. 28 can also be found in Appendix A2.
 225 For the remainder of the paper, we will refer to the total collision efficiency E as E_c .

226 3 Discussion of Boehm's Theory for habit prediction

227 3.1 Shape assumptions for columns

For particles that change habit, the hydrodynamic assumption in Böhm's theory changes from a symmetric flow around an oblate to an asymmetric flow around a cylinder (cf. dashed lines in Fig. 3). This change in morphology between primary habits may not be fully transferable to natural ice geometries, where complex crystalline features such as capped columns may evolve instead of complete habit changes. It is unclear if and how the spheroidal approach could capture these effects. Recent laboratory results from McCorquodale and Westbrook (2021) provide data for over 80 particle geometries at different aspect ratios. McCorquodale and Westbrook (2021) also evaluate the performance of Böhm's original work (Böhm, 1989, B89) and criticize a general overestimation of the drag coefficient. We expect the modifications from (Böhm, 1992a) to (Böhm, 1999) including the dependency on the shape of the spheroidal to significantly improve the agreement with the lab data. The C_d - N_{Re} relationship of the latest formulation from Böhm is compared with the TRAIL results in Figure 1 and the data points for the *CO1* particle ($\phi = 1.0476$) from Westbrook and Sephton (2017). We re-scale the drag coefficient by the area ratio $A_r^{1/2}$ compensates for the effect of A_r and allow comparison between the data and the derived C_d - N_{Re} -relation of A. J. Heymsfield and Westbrook

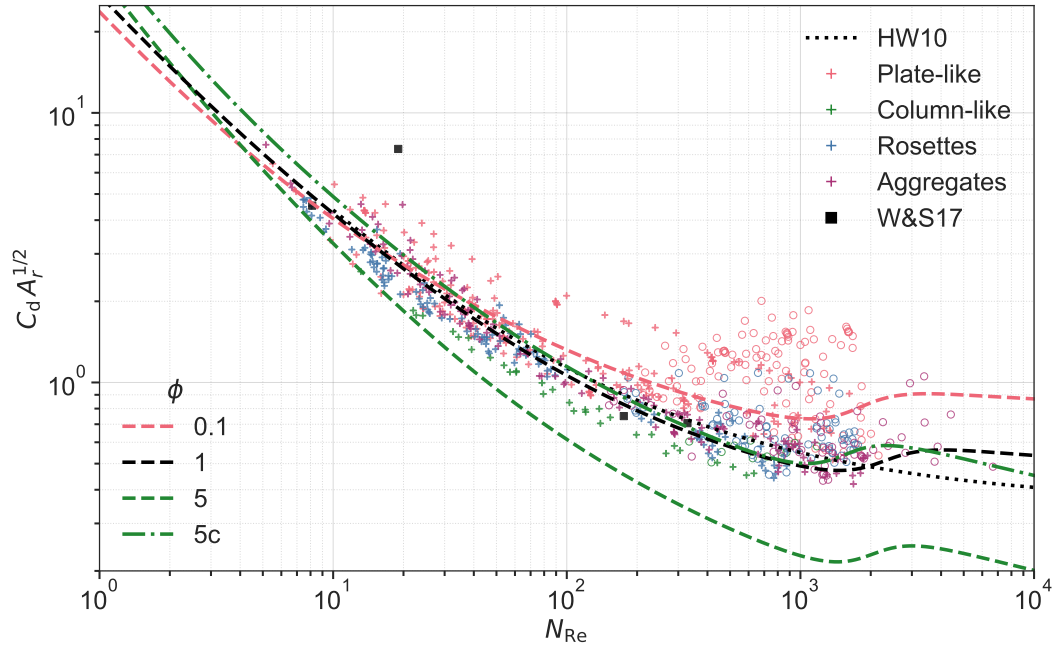


Figure 1. Comparison of measurements of N_{Re} and drag coefficient C_d for ice particle analogues (colored '+'/'o' for steady/unsteady regimes) against the parameterization of Böhm. Black squares mark the data from Westbrook and Sephton (2017, W&S17) for a cylinder with $\phi = 1.0476$. The black dotted line marks the results from A. J. Heymsfield and Westbrook (2010), while the dashed colored lines show the results using the parameterization from Böhm for the corresponding ϕ .

(2010). The dashed and dash-dotted lines show three different ARs (color-coded) representing spherical ($\phi = 1$, black), plate-like ($\phi = 0.1$, red), and columnar/prolate particles ($\phi = 5$, green). Additionally, we include colored markers for the TRAIL results. The area ratio needs special attention when the scheme of Böhm is used for prolate particles, because the definition varies from that of q (Eq. 23). McCorquodale and Westbrook (2021) define the area ratio A_r as

$$A_r = \tilde{A} A_{\text{cc}} = q \phi^{-1}, \quad (29)$$

with $q = 1$ for prolate spheroids and $q = 4\pi^{-1}$ for cylinders. For all other hydrometeor types we assume $A_r = 1$. The laboratory data and the parameterization agree well and the explicit dependence on the aspect ratio of the hydrometeors can capture the geometric effect of the different particle types. The drag coefficient of columnar particles differs significantly between the cylindrical and the prolate approach. At low Re , the prolate curve seems to reproduce the drag coefficient better. However, as Re increases, it greatly underestimates the drag and the cylindrical approach provides a better representation.

To better understand the difference in drag between cylindrical and spheroidal shapes, we compare the ϕ dependence of the parameterization with the laboratory results for prolate particles only. The combined data set consists of particles with $\phi = [1.0476, 2, 3, 5]$, allowing us to estimate the behavior near sphericity and the asymptotic behavior. Starting from low Reynolds numbers $N_{\text{Re}} \approx 10^0$, the two geometries slowly diverge as can be seen in Figure 2. For $N_{\text{Re}} > 10^2$, the prolate geometry agrees well with the two black squares marking the data of $\phi = 1.0476$, but has lower drag coefficients than the measurements for $\phi \geq 2$. The curves using the cylindrical assumption behave in the oppo-

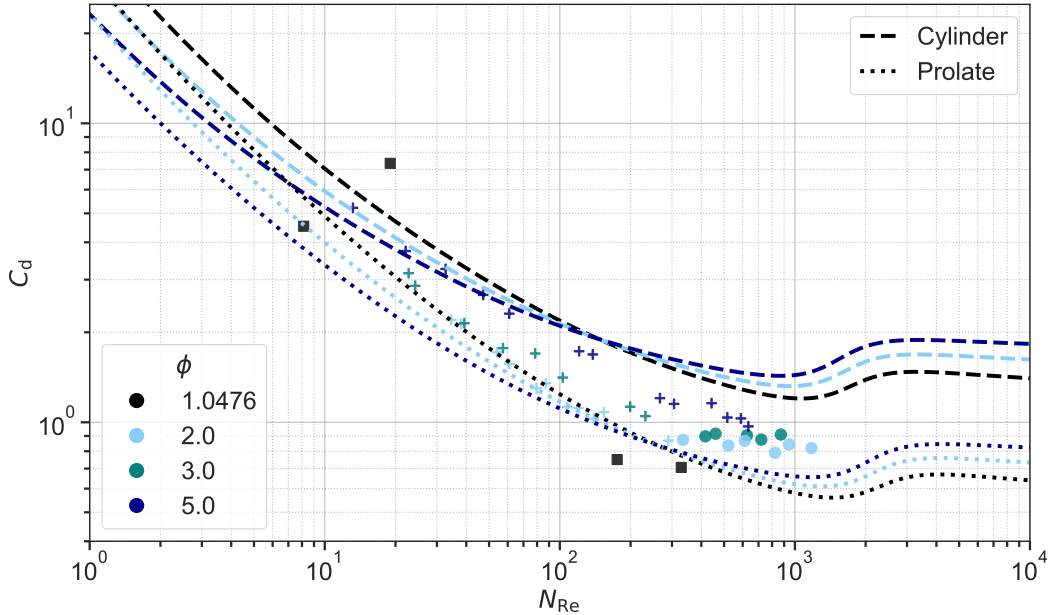


Figure 2. Comparison of N_{Re} and C_d for measured prolate ice particle analogues from McCorquodale and Westbrook (2021) ('+'/'o' for steady/unsteady regimes) and Westbrook and Sephton (2017) (squares) against the parameterization of Böhm for different ϕ (color-coded) and assumed hydrodynamic assumption (short-dashed: prolate, long-dashed: cylinder).

244 site way and predict to high drag coefficients for $\phi \geq 2$ and especially overestimate the
 245 behavior for $\phi = 1.0476$. The majority of the measurements lie between the two assump-
 246 tions. The disagreement for particles near sphericity explains the sudden deceleration
 247 of particles evolving from oblate or spherical particles into prolates when a cylinder is
 248 assumed and suggests a revision of this approach.

Using the original data from McCorquodale and Westbrook (2021), we derive a N_{Re} - C_d relation only for hexagonal columns (HCs) based on the area ratio A_r to describe the shape

$$C_d = A_r^n C_0 (1 + d_0 N_{Re}^{-1/2})^2. \quad (30)$$

The empirical values found are $n = -1/2$, $C_0 = 0.30$, and $d_0 = 7.1$, improving the agreement for HCs over the models of A. J. Heymsfield and Westbrook (2010) and McCorquodale and Westbrook (2021), which are generalized for all particle types (cf. Fig. A1). We use the empirical values obtained for Eq. (30) to extrapolate the behavior to other aspect ratios and corresponding terminal velocities. Particle characteristics are derived by similarity theory for specific data points of hexagonal columns. Figure 3 shows the fall speed as a function of aspect ratio $v_t(\phi)$ for four particles of increasing mass. The black and dark blue line are representative for $Re < 100$ and the light blue and grey line for particles with $100 < Re < 1000$. Comparing the results from Böhm's scheme for the spheroidal (solid) and the cylindrical prolate assumption (dashed), shows the aforementioned deceleration near $\phi = 1$. The fall velocity behavior derived from the data of McCorquodale and Westbrook (2021) suggests a more subtle transition from a prolate to a cylindrical geometry and fits the results of Figure 2. The cylindrical geometry prescribes an edge at the basal surface, but physically the representation of this edge in the hydrodynamic properties is at least questionable in the spheroidal framework of habits. We therefore

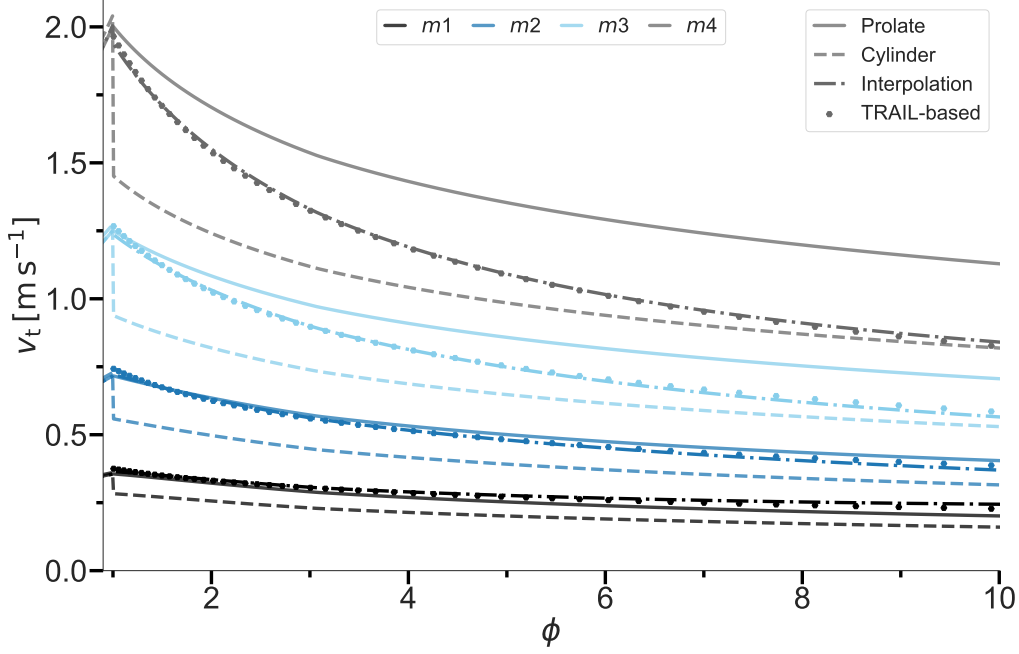


Figure 3. Terminal fall speed v_t dependency on the aspect ratio ϕ for particles with different mass (color-coded), treated as a prolate (solid) or a cylindrical spheroid (dashed), for TRAIL-based data (points), and for an interpolated approach (dash-dotted line, Eq. 31).

advocate an interpolation between the two fall velocities v_{pro} and v_{cyl} using the form

$$v(\phi) = f(\phi) v_{\text{pro}} + (1 - f(\phi)) v_{\text{cyl}}, \quad (31)$$

$$f(\phi) = \beta(m) e^{-\alpha(m)\phi} \quad (32)$$

This function helps to account for the relatively steep decrease in v_t with increasing ϕ , while matching the asymptotic behavior for the cylindrical approach. We propose a simple fit for the mass dependence of $\alpha(m)$ and $\beta(m)$

$$\begin{aligned} g(m) &= a \ln(m) + b, \\ a_\alpha &= 8.60 \times 10^{-2}, & b_\alpha &= 1.722, \\ a_\beta &= 3.08 \times 10^{-2}, & b_\beta &= 1.691. \end{aligned} \quad (33)$$

249 Figure 3 already includes the interpolated fall speed as dash-dotted lines that match the
 250 TRAIL results. The interpolation overcomes the need to choose between cylinder and
 251 prolate geometry, providing a smooth transition from prolate to cylinder-like behavior
 252 of ice columns.

253 3.2 Response to atmospheric conditions

The terminal fall velocity and the collision efficiency of Böhm are derived from using the Reynolds and Best numbers. This introduces a dependency on atmospheric conditions since both numbers depend on the air density ρ_a and the temperature via the dynamic viscosity $\mu(T)$ (Eqs. A1a & 13). Therefore, v_t and E_c must also change with height if a realistic atmospheric profile is assumed. Pinsky et al. (2001) find an increase in collision efficiency of more than a factor of two for a collision of small droplets ($D_1 \approx 30 - 50 \mu\text{m}$ and $D_2 \approx 10 - 20 \mu\text{m}$) between the 1000 and 500 hPa levels. The effect of the

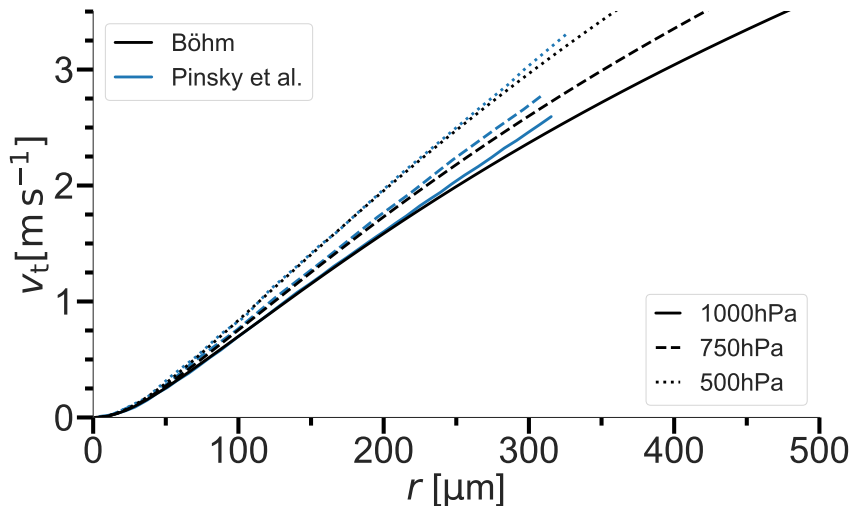


Figure 4. Dependency of v_t on the drop radius for the pressure levels 1000 hPa (solid), 750 hPa (long dashed), 500 hPa (short dashed) for Böhm’s scheme (black) and from Pinsky et al. (2001) (blue lines).

atmospheric conditions decreases with increasing droplet size. They argue that 90 % of the enhancement is due to the sensitivity of E_c to the relative velocity difference and only 10 % to an increase in swept volume. Böhm (1992b) finds an increase in E_c with temperature and pressure on the order of only 10 % for small drops ($r_1 \lesssim 30 \mu\text{m}$) and almost no effect for larger ones. Although we expect the work of Böhm to be generalizable, the contradiction of the two results requires an analysis of the dependence of Böhm’s fall velocity and collision efficiency parameterizations on different atmospheric states for droplets and ice particles. Compared to Pinsky et al. (2001), we change the surface temperature to freezing point to have a physically justified setup for ice particles at $p = 1000 \text{ hPa}$. While this change could affect the results, we argue that the exponential decrease in pressure with height dominates the effect over the linear dependence of temperature. Fig. 4 shows the comparison of terminal velocity by droplet size between the results of Pinsky et al. (2001) and with the scheme of Böhm. Böhm’s scheme predicts comparable results for all pressure levels. Both results show that the terminal velocity for a drop with $r = 300 \mu\text{m}$ is about 25 % greater at 500 hPa than at 1000 hPa. Using the adjustment factor of Beard (1980) allows us to compare the pressure dependence as a function of atmospheric conditions

$$f_{v_t} = \frac{v_t(T, p)}{v_{t,0}(T_0, p_0)}, \quad (34)$$

254 with the reference value of $v_{t,0}$ at $p_0 = 1000 \text{ hPa}$ and $T_0 = 273.15 \text{ K}$. We look at four
 255 different particle types (drop, oblate w. $\phi = 0.25$, prolate w. $\phi = 4$, and graupel w.
 256 $\phi = 1$ and $\rho_r = 800 \text{ kg m}^{-3}$) and five different masses equal to the mass of a sphere
 257 with an equivalent diameter of $D_{\text{eq}} = [20, 50, 100, 200, 500] \mu\text{m}$. In Figure 5 we see that
 258 the adjustment factor is proportional to D and can reach a maximum of about 1.3 at
 259 500 hPa for $D = 500 \mu\text{m}$. The difference between particle types is small, but becomes
 260 more relevant for larger particles.

261 In Figure 6 we analyze the effect of the changing thermodynamic state on the col-
 262 lision efficiency for four different collision pairs: drop-drop (D-D, solid lines), graupel-
 263 drop (G-D, dash-dotted lines), oblate-oblate (O-O, dashed lines), and prolate-prolate (P-
 264 P, dotted lines) collisions. The equivalent diameters of the particles involved are color-

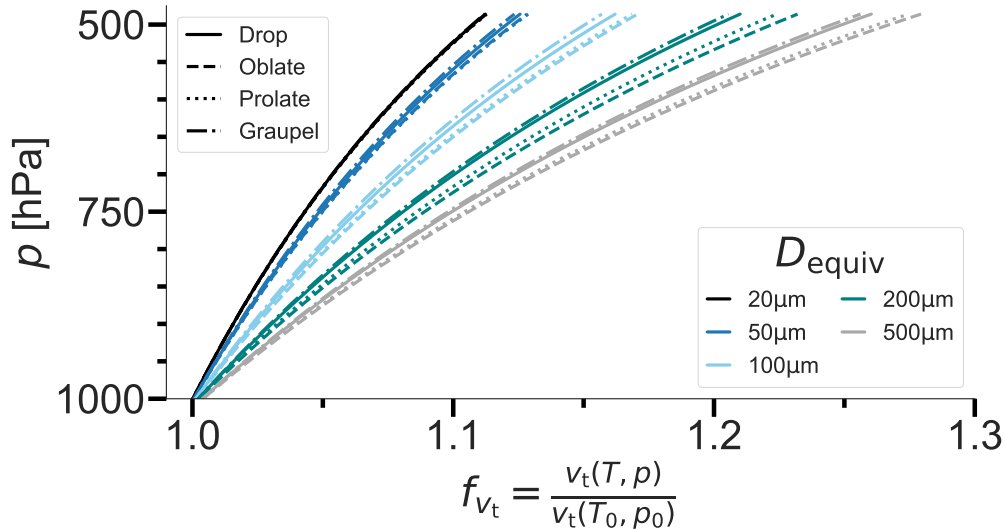


Figure 5. p -profiles of f_{v_t} for drops (solid), oblates (dashed), prolates (dotted), and graupel particles (dash-dotted lines). Color-coded is the equivalent diameter.

265 coded and include the size range used for the terminal velocity. The impact is inversely
 266 proportional to the mass/size and much smaller than for v_t , not exceeding 1.12. We can
 267 therefore specify the statement of Pinsky et al. (2001): for small particles, the change
 268 in collision efficiency itself dominates the collision behavior. The impact is higher for large
 269 particles ($\leq 30\%$), where the change in terminal velocity dominates the atmospheric depen-
 270 dence of the collision kernel. Looking at pairs with similar fall velocities, where the
 271 collision efficiency rapidly approaches zero, we observe adjustment factors greater than
 272 two, as observed by Pinsky et al. (2001) (not shown). The combined effect of atmospheric
 273 conditions on terminal velocity and collision efficiency is shown in Figure 7 via the ad-
 274 justment factor of the collision kernel K . The impact is strongest for the collision of small
 275 particles where the onset of effective collision causes strong difference in collision efficiency.
 276 For all collisions of larger particles, the total amplification does not exceed 2.5% and can
 277 be considered negligible.

278 3.3 Habit impact on riming efficiency

279 While Böhm compares and calibrates his theory for the collision efficiency with re-
 280 sults of Schlamp et al. (1975), Martin et al. (1981) and Reinking (1979), more recent re-
 281 sults of e.g. Wang and Ji (2000) are available. These are improved with respect to the
 282 shape of the particles investigated and the accuracy of the flow field, including unsteady
 283 features. Therefore, their results are suitable to evaluate the validity of Böhm (1992a)'s
 284 theory for collision events of spheroids with spherical droplets up to radii of $r = 100\ \mu\text{m}$.
 285 In Figure 8, the analytical collision efficiencies of Böhm are plotted against the simula-
 286 tion of Wang and Ji (2000) for given geometries of oblates, cylinders, and broadly branched
 287 crystals. The cylindrical shape is the most difficult to compare due to the mismatch be-
 288 tween the actual and spheroidal shape, combined with the asymmetry of the flow.

289 The results for the oblates are in good agreement with respect to the onset, max-
 290 ima and cut-offs of all eight particles (Fig. 8a). The direct comparison for the cylinder
 291 (Fig. 8b) shows a slightly delayed onset and higher maxima for curves following the theo-
 292 ry of Böhm. The cut-offs are shifted to higher collected droplet radii compared to Wang
 293 and Ji (2000). Note that terminal velocity interpolation is applied. For branched crys-

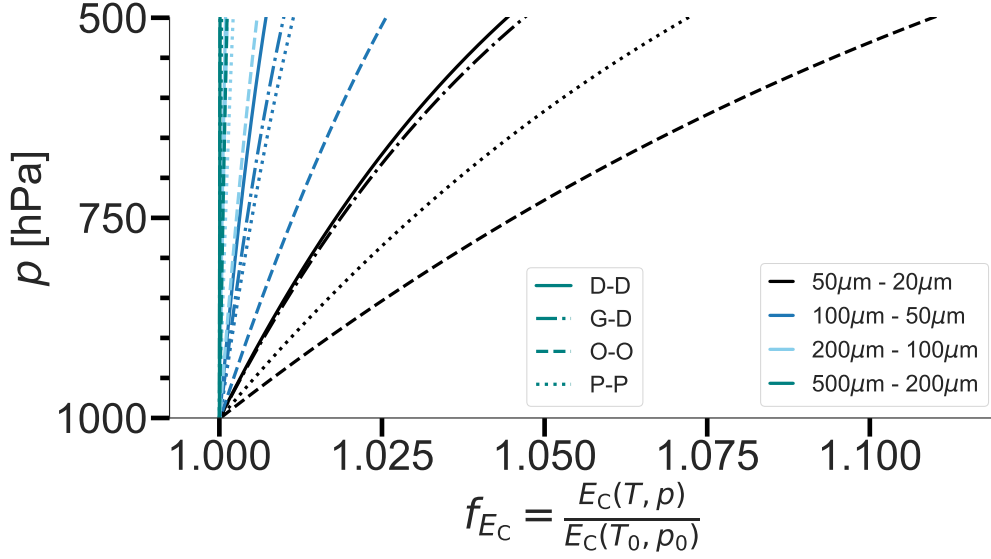


Figure 6. p -profiles of f_{Ec} for a drop-drop (D-D, solid), graupel-droplet (G-D, dash-dotted lines), an oblate-oblate (O-O, dashed), and a prolate-prolate collision (P-P, dotted). Color-coded is the equivalent diameter of the colliding particles.

294 tals (Fig. 8c) the onset and maximum are quite close. Only the cut-off radii differ, es-
 295 pecially for larger crystals. Nevertheless, the overall similarity of the results is satisfac-
 296 tory considering the theoretical assumptions. We conclude that the theory of Böhm pro-
 297 vides a suitable framework for parameterizing the collision efficiency of primary habits
 298 compared to numerical simulations.

299 4 Revision of Theory

300 4.1 Shape-dependent ventilation

301 Several studies present formulations for habit-specific ventilation coefficients based
 302 on the underlying geometry, which may differ substantially from Hall and Pruppacher
 303 (1976, HP76) (Prolate: Wang and Ji (2000, WJ00), Ke et al. (2018, Ke18), Kiwitt et al.
 304 (2022, K22), Y. Chen et al. (2021), Oblates: Pitter et al. (1974, P74), Ji and Wang (1999,
 305 J99), Wang (2021, W21), Nettesheim and Wang (2018, NW17), spheres: Woo and Hami-
 306 elec (1971, WH71), Whitaker (1972)).

The left side of Figure 9 shows a collection of these data sets as well as three pro-
 posed fits of the dependence of ventilation on X_v for spheres (Hall & Pruppacher, 1976,
 solid), dendrites (Nettesheim & Wang, 2018, NW17, long dashed), and columns (Ji &
 Wang, 1999, JW99, short dashed). The formulation of Hall and Pruppacher (1976) shows
 reasonable behavior for (nearly) spherical particles, but especially for prolate particles,
 large underestimations of the ventilation coefficient are given (up to 3 for a given X_v).
 Using the collected data set, we modify the formulation of Hall and Pruppacher (1976,
 cf. Eq. 30) by adding a ϕ -dependent term to the ventilation coefficient

$$\begin{aligned}
 f_{v,\text{prolate}} &= f_v + c_1 X_{v,\text{equiv}} \phi, & \text{for } \phi > 1, & \quad c_1 = 2.8 \times 10^{-2}, \\
 f_{v,\text{oblate}} &= f_v + c_2 X_{v,\text{equiv}}^{3/2} \phi^{-1}, & \text{for } \phi < 1, & \quad c_2 = 2.8 \times 10^{-3}.
 \end{aligned}
 \tag{35}$$

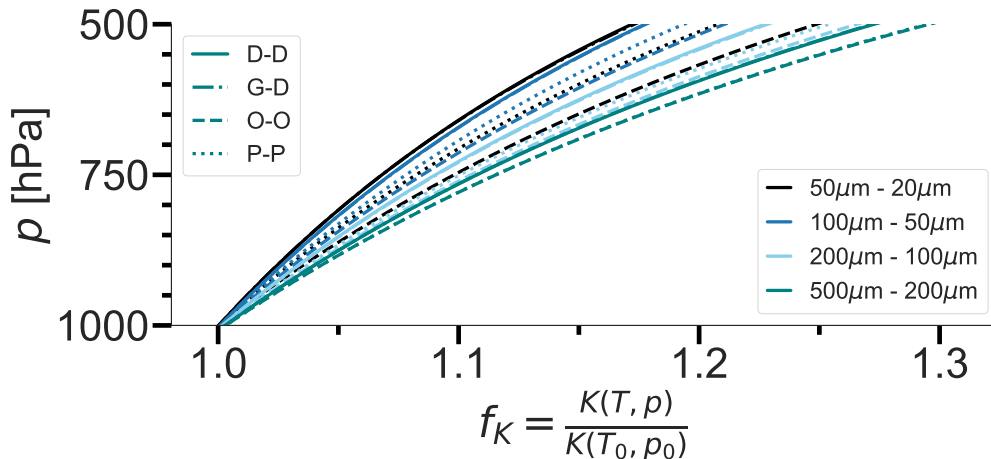


Figure 7. p -profiles of f_K for a drop-drop (D-D, solid), graupel-droplet (G-D, dash-dotted lines), an oblate-oblate (O-O, dashed), and a prolate-prolate collision (P-P, dotted). Color-coded is the equivalent diameter of the colliding particles.

307 Good agreement with the data can be found for all geometries (right side of Figure 9).
 308 It is important to note that we have not introduced any feedback between this shape-
 309 dependent (overall) ventilation coefficient (Eq. 9) and the effect of ventilation on the in-
 310 herent growth function (Eq. 15). The latter only uses the generalized form of Hall and
 311 Pruppacher (1976) and considers the habit effect individually.

312 4.2 Inherent Growth Function

313 The IGF, as introduced by CL94, can describe primary and secondary habit devel-
 314 opment in the spheroidal framework (e.g. Jensen & Harrington, 2015; Sulia & Har-
 315 rington, 2011; Shima et al., 2020)). While providing a fundamental physical description
 316 of the growth ratio of the a - to c -axis, the original fit of observational and laboratory re-
 317 sults has some inconsistencies when compared with more recent laboratory (Connolly
 318 et al., 2012) or modeling studies (Sheridan et al., 2009; Hashino & Tripoli, 2007) for cer-
 319 tain temperature regimes.

320 In this section, we will evaluate the results using the original IGF, point out its de-
 321 ficiencies, and propose another version of the IGF based on observational evidence that
 322 corrects some of the shortcomings.

323 4.2.1 Original version of Chen & Lamb

324 Takahashi et al. (1991, TH91) provide a set of laboratory measurements that quan-
 325 tify the depositional growth of ice crystals at constant temperature ($T \in [250 \text{ K} - 270 \text{ K}]$)
 326 and water saturation. Because of the high quality measurements of the mass, density,
 327 and geometry of individual ice crystals, J.-P. Chen and Lamb (1994b) use the TH91 ex-
 328 periments as a benchmark to validate their habit prediction scheme. Figure 10 repro-
 329 duces Figures 7-9 of J.-P. Chen and Lamb (1994b) using results from the HP scheme
 330 without (black) and with the new habit-dependent ventilation coefficient (green lines).
 331 It also includes the result with a diagnostic geometry for monomers using the empiri-
 332 cal m - D relationship of Mitchell (1996) for aggregates of side planes, columns, and bul-
 333 lets (S3, long dashed lines) and a strictly spherical geometry (short dashed lines). In the
 334 lab experiment, the particles freeze from a droplet distribution and the size/weight shows

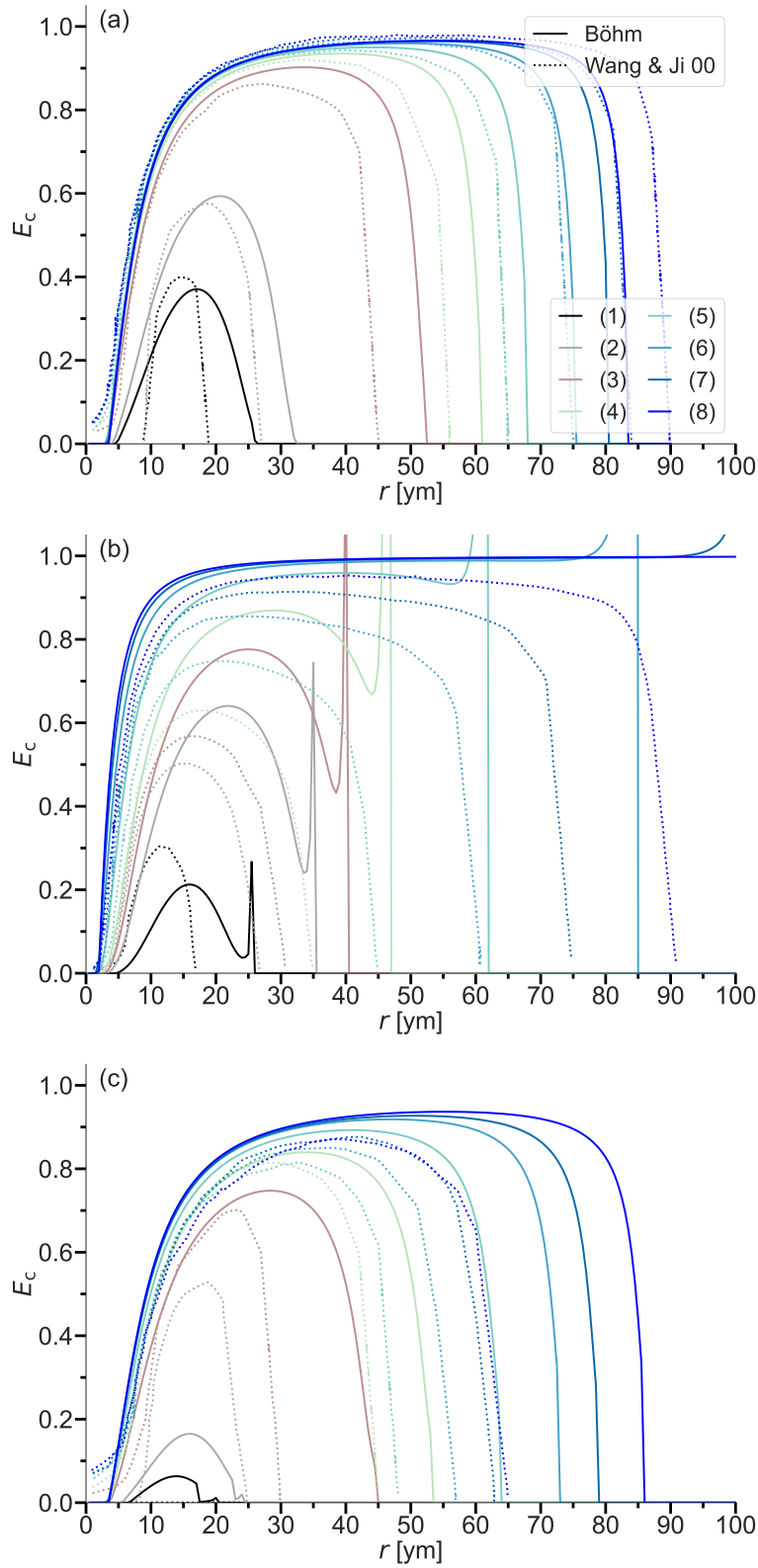


Figure 8. Collision efficiencies of a) thin oblates, b) cylinders, and c) broadly branched crystals with spheres. Particle dimensions and reference numerical simulations of Wang and Ji (2000).

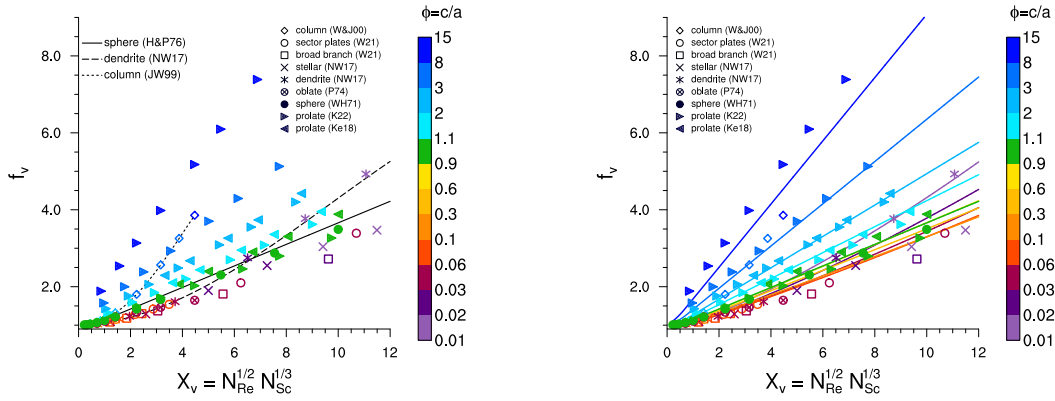


Figure 9. Left: Data points and functional dependencies of $f_v(X_v)$ for several studies. Right: Proposed functional habit-dependent description $f_v(\phi)$. The aspect ratio of the assumed particles is color-coded.

slight variations. In the simulations, an initial radius similar to the maximum of the droplet distribution of $r_{\text{start}} = 2 \mu\text{m}$ (Takahashi & Fukuta, 1988) shows overall good agreement with the laboratory data and compares significantly better than the m - D -relationship of Mitchell. The difference in the initial radius is considered small compared to the uncertainties of the measurements and the model assumptions.

For the limiting case of spherical development at $\Gamma = 1$ for temperatures $T \in [253 \text{ K}, 263 \text{ K}]$, the habit prediction is in agreement with the results for spherical particles, and the laboratory results show slightly lighter crystals. In the columnar regime, $T \in [248 \text{ K} - 252 \text{ K}]$ (cold) and $T \in [263 \text{ K} - 268 \text{ K}]$ (warm), the prolates are heavier. For the oblate maximum around $T = 258 \text{ K}$ they are lighter than laboratory data suggest. Since $X_{v,\text{equiv}}$ does not exceed 1.5 for all particles studied, we see only a slight enhancement of the deposited mass for all non-spherical growth regimes when the habit-dependent ventilation coefficient is included. As expected, prolates are more influenced than oblates, but not enough to change the geometry or density significantly (Fig. 10b&c). From here on, all results will include the habit-dependent ventilation coefficient.

The differences between our model and the laboratory data for particle mass are due to the predicted geometry, too high/low apparent density, or a combination of both. Therefore, Figure 10 (b) and (c) show that within the warm columnar regime, prolates tend to grow to larger aspect ratios than suggested by the laboratory data. Nevertheless, the eventual hollowing captured by the deposition density parameterization is representative. The axis length of oblate growing particles follows the results for the a axis, while showing an inability to represent strongly branched, thin dendritic crystals. This feature is due to the spheroidal assumption and the initial spherical growth up to $D \geq 10 \mu\text{m}$, leading to an overestimation of the c axis size.

If all particles were allowed to grow habit-specifically immediately after nucleation it would reduce the differences observed for the oblate geometry, but leads to unnatural aspect ratios in the columnar regime. The coupling of IGF and deposition density leads to branching for the entire oblate regime and does not reproduce the sharp density minimum for branching particles observed by TH91.

Particles within the cold columnar regime ($T < 253 \text{ K}$) evolve prolate features with a secondary maximum, while TH91 observe nearly spherical or only slightly prolate particles. The habit description becomes ambiguous for the temperature range due to the increased occurrence of polycrystals (based on field observations e.g. Um et al. (2015)). The complex shape of polycrystals and their density cannot be adequately captured by the spheroidal approach. However, model agreement with laboratory data on ice mass deposition is improved by the explicit habit prediction and habit-dependent ventilation.

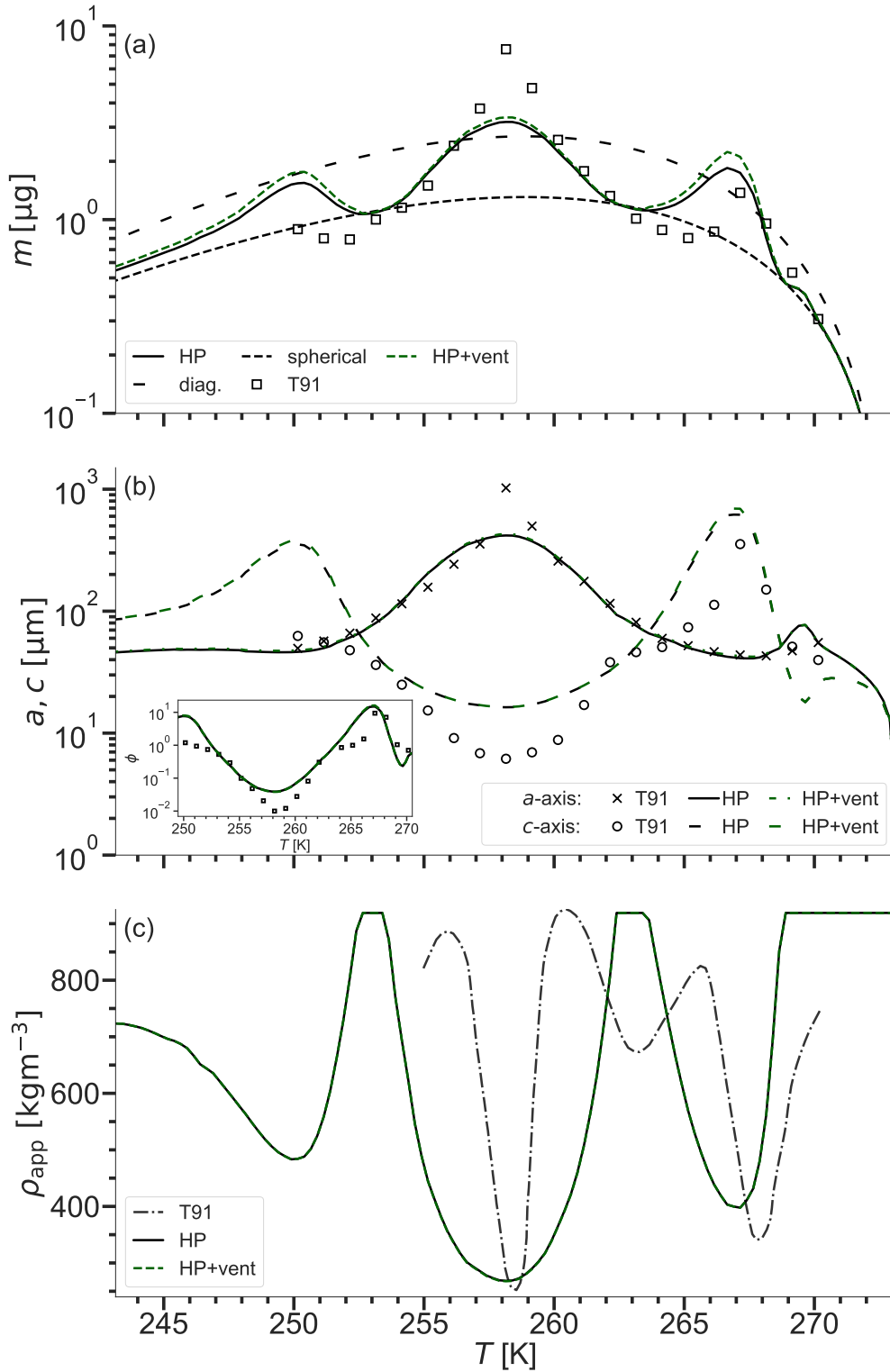


Figure 10. T -dependence of (a) m , (b) geometry (a -, c -axis, ϕ), and (c) ρ_{app} after 10 min of vapor deposition. The black line shows results for the baseline HP, green lines include the habit-dependent ventilation coefficient, and the markers show results of Takahashi et al. (1991, TH91). (a) includes a line for a particle with a diagnostic geometry (diag., long dashed) and that for a spherical crystal (short dashed).

371

4.2.2 Polarimetric signal of model results

372

373

374

375

376

377

378

379

380

381

382

383

384

385

386

387

388

389

390

391

392

393

394

395

396

397

398

399

400

401

402

403

404

405

406

407

408

To further analyze the modeled results, we use the methods proposed by Myagkov, Seifert, Wandinger, et al. (2016) to calculate the polarizability ratio for the different temperature regimes. Myagkov, Seifert, Bauer-Pfundstein, and Wandinger (2016) combines the methods of Melnikov and Straka (2013) and Matrosov et al. (2012) to obtain the polarizability ratio ρ_e (PR) from a 35 GHz cloud radar with a hybrid polarimetric configuration. The PR is based on the particle shape and its dielectric properties and can be used to retrieve information about the environmental conditions under which particles develop certain habits and apparent densities. For their analysis, only particles near cloud top are considered since these observed characteristics developed in local conditions and particle mixtures are unlikely. Myagkov, Seifert, Wandinger, et al. (2016) show that observed PRs are similar to those obtained from the free fall chamber of Takahashi et al. (1991) within the uncertainties of the (temperature) measurements. The PR analysis provides insight into the functional coupling between geometry and density via the IGF (Eq. 7). It is important to note that the sensitivity of the PR to a change in geometry is higher for high particle densities (see Fig. 2 of Myagkov, Seifert, Wandinger, et al. (2016)).

Figure 11 compares the PRs of TH91 (open grey triangles, all growth times), observations near cloud tops (Myagkov, Seifert, Wandinger, et al., 2016, black squares), and the results after three and ten minutes of simulated growth with HP (pluses/circles, color indicates app. density). We show two different time steps of *McSnow* to distinguish between primary and secondary habit effects of oblates: after three minutes, only primary habits develop, so that particles reach a maximum PR before branching. The qualitative results of the HP compare well with TH91 and observations. Particles with the most extreme PRs do not develop in *McSnow*, and their transition between regimes appears to be shifted.

For the maximum in the warm prolate regime, the particles appear to have the correct aspect ratio (Fig. 10(b)) with a slightly lower PR than the observations. This finding suggests that the warm prolate maximum of the IGF may cause excessive hollowing. In addition, the maximum may be too broad, causing an offset in the transition regime.

Oblates that turn out not to be thin enough (cf. Fig. 10b)) result in a PR that (after three minutes) is not as low as suggested by the observations, but is qualitatively consistent. The strong branching of the particles throughout the oblate-favoring regime leads to an overestimated reduction of the PR for the simulated particles. According to this analysis, it seems necessary to postpone branching to later stages of particle evolution.

Warm oblates ($269 < T < 273$ K) and the cold prolate maximum ($T < 252$ K) cannot be fully evaluated due to a lack of observational data points. However, existing laboratory measurements suggest that these maxima may be overestimated. The above deficiencies for the specific regimes are:

409

410

411

412

1. oblate minimum around $T = 269$ K is too low,
2. prolate maximum around $T = 267$ K too high m with too low ρ_{app} ,
3. crystals around $T = 258$ K not thin enough ,
4. cold prolate/polycrystal regime exhibits has too high m and ϕ .

413

4.2.3 Updated Inherent Growth Function

414

415

416

417

418

419

420

421

To overcome the above deficiencies, we propose a modification of the IGF and related assumptions to improve the habit-dependent particle growth. Starting from point one, there is no clear evidence for a strong oblate minimum at $T = 269$ K, either from the observations shown above or from other sources such as Bailey and Hallett (2009). We therefore use the values suggested by Sei and Gonda (1989). Future retrievals may be useful to evaluate this change.

Point two can be addressed by reducing the IGF maximum around $T = 267$ K by 25% and fitting the curve to $\Gamma = 1$ at the appropriate temperatures. This change should

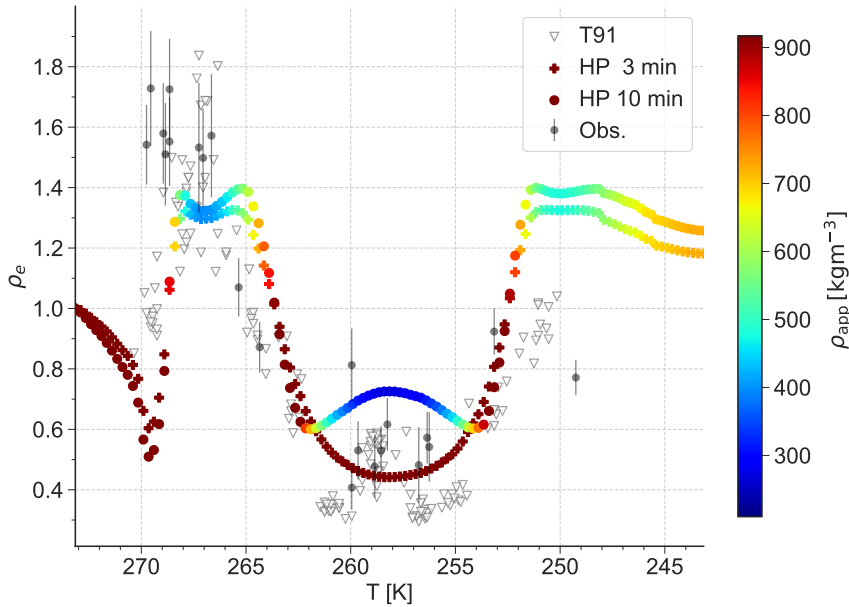


Figure 11. T -dependence of polarizability ratios ρ_e for ice crystals grown in the free-fall chamber (open grey triangles), with HP ([+] for $t = 3$ min, [•] for $t = 10$ min), and observed near cloud tops (black squares, error bars represent ± 1 standard deviation). Color-coded is the particle's apparent density ρ_{app} .

422 result in slightly shorter, lighter, but denser columns that better match the TH91 data.
 423 For PR, the geometric change is (partially) offset by an increase in density.

424 In the oblate growth regime, the IGF initially produces the correct geometries (cf.
 425 3 min results), but branching seems to occur too early and for a relatively wide range
 426 of planar particles. Comparing the simulated density with the wind tunnel results (Fig. 10c),
 427 we see that particles branch only for a narrow temperature range. So instead of chang-
 428 ing the IGF, we change the branching criterion to better resemble the onset of branch-
 429 ing. In the formulation of JH15, branching does not occur before $a \geq 100 \mu\text{m}$. Here,
 430 we assume that particles branch when $a \geq 200 \mu\text{m}$, effectively delaying the onset of branch-
 431 ing.

432 For the final point, we merge the time-dependent growth rates of TH91 (Tab. 2 of
 433 Takahashi et al., 1991) with the results of Sheridan (2008) and Sheridan et al. (2009).
 434 Connolly et al. (2012) also report a discrepancy between observed and modeled crystals
 435 for the regime around $T = 253 \text{ K}$ using CL94's IGF, but they assume oblate growth
 436 for colder temperatures. Due to the dominance of polycrystals, it becomes difficult to
 437 generalize these habits to either prolate or oblate spheroids. The advantage of assumed
 438 columnar growth is the immediate hollowing, which effectively reduces the apparent den-
 439 sity, whereas if oblate growth is assumed, the branching criterion of JH15 is not met be-
 440 cause the particles remain nearly spherical.

441 Figure 12 shows the original IGF (black) and our proposed version (blue line) combin-
 442 ing the above modifications, together with the diagnosed Inherent Growth Ratios of
 443 Takahashi et al. (1991) (red and black dots). In Figure 13, results of the depositional growth
 444 experiment using the new IGF (blue lines) are compared with the original results (black
 445 lines) for mass, axis measure, and apparent density. Using the new IGF, the accumu-

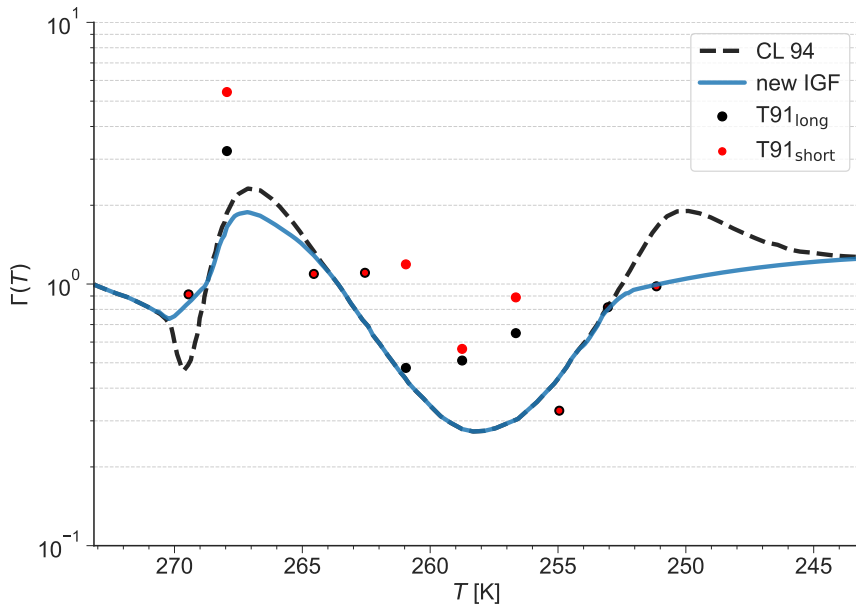


Figure 12. Inherent Growth Function of CL94 and our new formulation as a function of temperature. Explicit values of Takahashi et al. (1991) are marked as red and black dots.

446 lated mass is decreased for the warm prolate peak as well as in the polycrystalline regime,
 447 removing the secondary peak (colder $T = 253$ K) (Fig. 13a). In terms of geometry, the
 448 changes induced by the modified IGF are suitable for both prolate regimes. There is no
 449 modification of the IGF in the oblate regime around $T = 258$ K. The reduction of the
 450 warm oblate ϕ minimum is in good agreement with the laboratory results. The result-
 451 ing changes in particle density are negligible.

452 A second experiment includes the modified IGF, combined with the modified branch-
 453 ing criterion of $a \geq 200 \mu\text{m}$ introduced above (IGF2+, red lines). The lower limit of
 454 $D > 10 \mu\text{m}$ for habit development can be physically justified by the studies mentioned
 455 above, but at the same time it prevents the development of very thin oblates observed
 456 by Takahashi et al. (1991). In this setup we therefore remove the limiter and allow free
 457 evolution after nucleation, which gives the best agreement with TH91. The modifications
 458 result in more mass being deposited around $T = 258$ K, bringing the results closer to
 459 the TH91 measurements. In terms of geometry, the transition from the oblate to the poly-
 460 crystalline regime as well as the shape of the oblates are very similar to the measurements.
 461 The coupling of the IGF and the deposition density leads to subsequent changes in the
 462 apparent density. It seems difficult to assess the change in apparent density, but the nar-
 463 rowed oblate minimum seems justified, while the warm prolate minimum might overes-
 464 timate the particle density. To evaluate the combined effect of shape and density, we an-
 465alyze the PR with the updated IGF including the additional modifications. Figure 14
 466 confirms that this setup can remove the major deficiencies between the laboratory mea-
 467 surements and the simulation. The warm oblate regime shows higher PRs, while the warm
 468 prolate maximum is slightly closer to the majority of observational data due to the in-
 469terplay of geometry and density (less hollowing). Nevertheless, the highest PRs cannot
 470 be matched. This discrepancy can be attributed to the parameterization of the hollow-
 471 ing, since the AR is well matched. In the cold oblate regime, delayed branching signif-

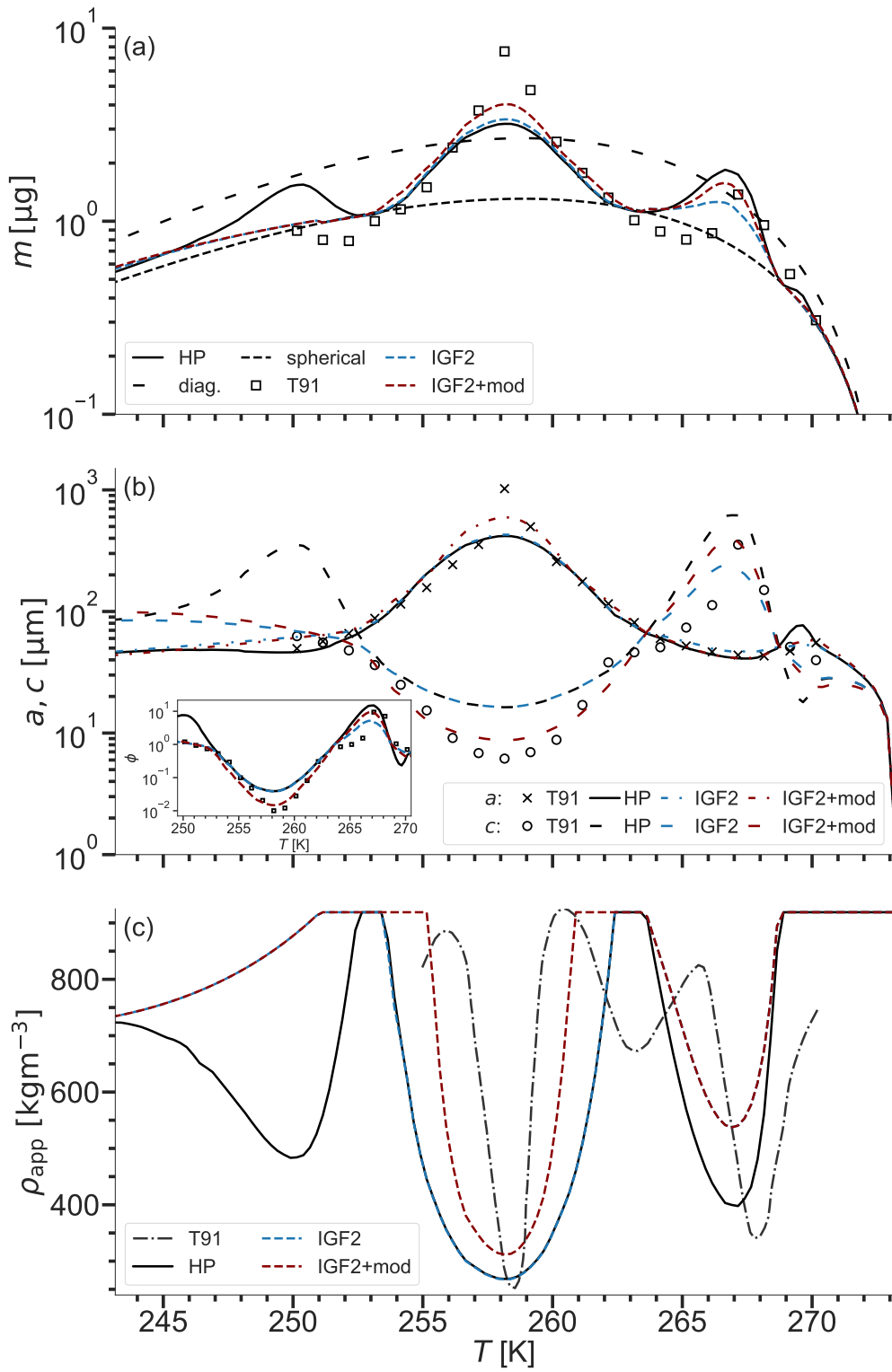


Figure 13. As Fig. 10 but also compared with the results of the updated IGF (blue) and of the updated IGF including branching modification (IGF2+, red).

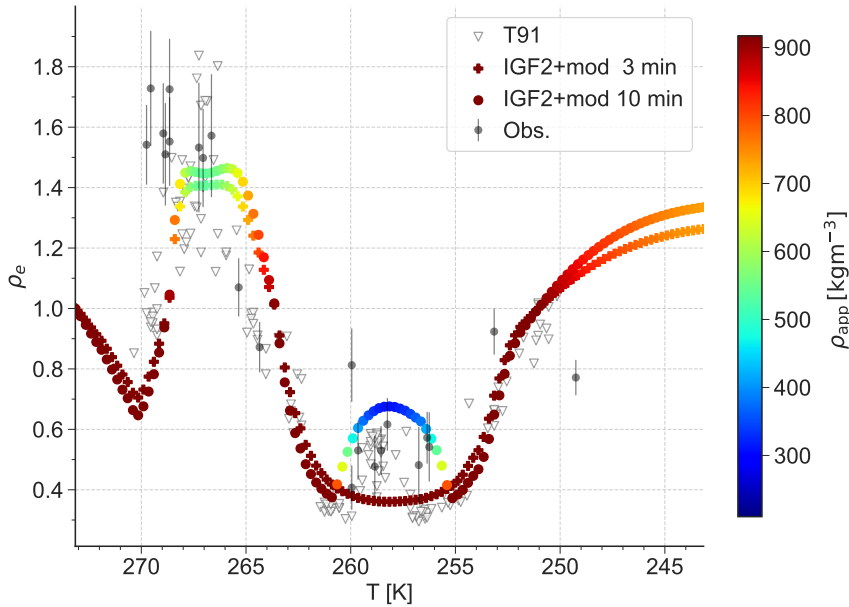


Figure 14. As Fig. 11 but with the new IGF and altered branching criterion.

472 icantly improves the agreement of the PR with the observational and T91 results. The
 473 evolution of particles with very low PRs ($\rho_e < 0.4$) can be observed after three min-
 474 utes, as suggested by the measurements. The same is true for the increase in PR due to
 475 strong branching around $T = 258$ K. Finally, the transition from oblate to polycrys-
 476 tals seems to agree better with the results of T91 and Myagkov, Seifert, Wandinger, et
 477 al. (2016). For possible further modifications of this version of the IGF, more retrieved
 478 observational or laboratory data are needed. In particular, the regimes that are sparsely
 479 populated by measurements (such as the polycrystalline region) could be of great benef-
 480 it to such a detrimental function as the IGF.

481 5 Case study exhibiting sensitivities

482 Habit prediction has a pronounced impact on many microphysical processes and
 483 can introduce variability among particles by abandoning static m - D and v_t -relations. *Mc-*
 484 *Snow* is unique in the sense that it combines the habit prediction scheme of J.-P. Chen
 485 and Lamb (1994b) and Jensen and Harrington (2015) with the full set of parameteriza-
 486 tions of Böhm. Using Böhm's framework for the parameterization of particle properties
 487 allows a physically consistent and mathematically continuous description of the habit
 488 dependency of most microphysical processes. The effect of habit prediction on particles
 489 at constant temperature has been shown in Figure 10, but this setup can only serve as
 490 a limiting case. In real clouds, hydrometeors experience different thermodynamic con-
 491 ditions and change the conditions themselves by absorbing/releasing water and latent
 492 heat. We soften the constraints implied by the laboratory setting by focusing on a setup
 493 where particles fall through a one-dimensional column (rain/snow shaft) with a prescribed
 494 atmospheric profile. The model setup (Fig. 15) is defined to mimic different sections in-
 495 side a cloud where certain relevant ice-microphysical processes dominate. In the upper
 496 part, depositional growth of small particles should govern the evolution. The ice mass

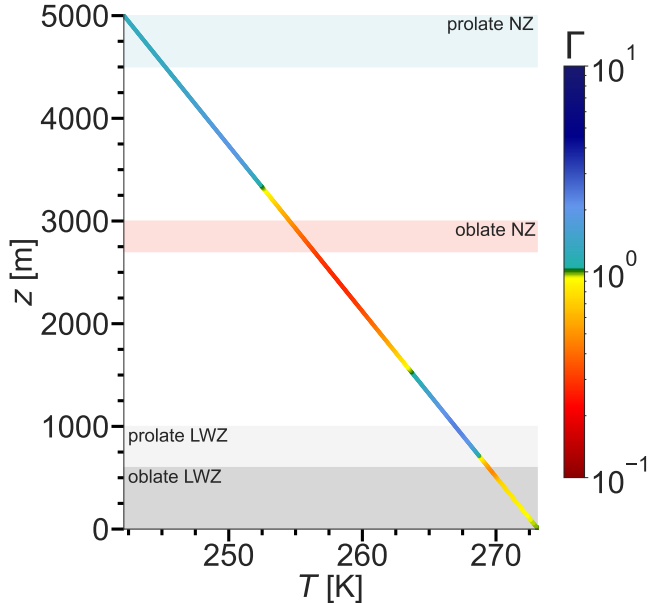


Figure 15. Background atmosphere for the 1-D model simulations incl. the vertical profiles of temperature and corresponding IGF. The nucleation (NZ) and liquid water zones (LWZ) are situated in the shaded regions for the respective cases.

497 accumulated by deposition changes the shape and fall velocity. Both terminal velocity
 498 and geometry are linked to the likelihood of collision events and change the onset of ag-
 499 gregation and how effective it is. In the lower part of the profile, both monomers and
 500 aggregates encounter a liquid water zone (LWZ) where the impact of the ice habit on
 501 the effectiveness of riming is examined.

502 5.1 Setup

503 Similar as in Brdar and Seifert (2018), the temperature profile is constructed using
 504 the surface temperature of $T_{\text{surf}} = 273 \text{ K}$ and a constant lapse rate of $\gamma = 0.0062 \text{ Km}^{-1}$.
 505 The domain height is case specific with $z_{\text{top}} = 5000 \text{ m}$ ($T_{\text{top}} = 242 \text{ K}$) for a prolate
 506 and $z_{\text{top}} = 3000 \text{ m}$ ($T_{\text{top}} = 254.4 \text{ K}$) for an oblate favoring regime. Water vapor, liq-
 507 uid water, and temperature are assumed to be constant and not increased or decreased
 508 by any microphysical process.

509 In the upper 80% of the (case-specific) domain, particles grow solely by vapor de-
 510 positional growth and aggregation at a supersaturation of 5%. In the lower 20%, the
 511 regime is dominated by riming due to a liquid water zone ($LWC = 0.2 \text{ gm}^{-3}$), which
 512 enhances particle growth and in turn increases the probability of aggregation. We do not
 513 impose a subsaturated regime because the habit-specific effect is small and possible ag-
 514 gregation events become unlikely due to decreasing particle size. The initial properties
 515 (mass and size) of the ice crystals are drawn from a gamma distribution with a mean
 516 mass equal to the mass of a spherical ice particle with a diameter of $D = 10 \mu\text{m}$, the
 517 initial aspect ratio is set to $\text{phi} = 1$. Particles are generated at a constant nucleation
 518 rate within a nucleation zone that spans 10% of the total domain height. A random ini-
 519 tialization height has a positive effect on the variance of the developed particle habits
 520 due to the different atmospheric conditions compared to constant nucleation at the do-
 521 main top. Particles larger than $D > 10 \mu\text{m}$ are initialized with a density derived from

empirical mass-area relations to avoid underestimating the actual particle geometry and overestimating the fall velocity.

We integrate the model over 10 h to reach a steady state, and all statistical quantities are averaged over the last 5 h. Riming is treated by the stochastic riming scheme (cf. Brdar & Seifert, 2018; Brangi et al., 2020) which makes use of the theory of Böhm for terminal velocity and collision efficiency.

Sheridan et al. (2009) shows that habit development is strongly controlled by conditions shortly after nucleation, when relative changes in mass and shape are most pronounced. Numerical models of the atmosphere typically assume uniform thermodynamic conditions within a grid cell. Especially in regions where the IGF shows strong gradients, the uniform treatment leads to different habits as if the actual thermodynamic conditions at the position of the particles were assumed. In Large Eddy Simulation (LES) and Numerical Weather Prediction (NWP) models the vertical spacing inside clouds can easily exceed $\Delta z = 50$ m (Dziekan et al., 2019; Shima et al., 2020), which already results in a temperature difference between the lower and upper edge of the cell of $\Delta T \geq 0.3$ K (assuming the above temperature gradient). Hence, we strongly recommend an interpolation of the atmospheric state to the particle position, making the habit evolution independent of the resolution of the atmospheric grid.

5.2 Deposition

The results in Figure 10 imply a change in deposition rate due to the habit prediction and the preceding dependencies on capacitance, ventilation, and fall velocity. To study the effect of particle habits without the complex feedback between ice microphysical processes, we suppress aggregation and remove the liquid water layer for the time being. We focus on a prolate and an oblate favoring initial growth scenario as archetypes for typically observed monomer cases and show why it is important to consider ice habits.

5.2.1 Prognostic geometry vs. m - D -relationship

Figure 16 illustrates the diversity of particle properties induced by the temperature dependence (original IGF of CL94) of the habit evolution of the mass, velocity, and density of individual crystals relative to their maximum dimension. Since there is no complete set of empirical formulations, we use individual relations for the variables: mass-size of Mitchell (1996), velocity of A. Heymsfield (1972, Tab. 3), and apparent density from Pruppacher and Klett (1997) for comparison.

Unless otherwise stated, we compare the results of the explicit habit prediction with those of simulations using the diagnostic geometry for monomers and aggregates as introduced by Brdar and Seifert (2018) using the power law of Mitchell (1996) for aggregates of side planes, columns, and bullets.

Like Shima et al. (2020), we use the normalized mass of the ice particles

$$\bar{m} = \frac{m}{\rho_i \frac{\pi}{6} D^3}, \quad D = 2 \max(a, c) . \quad (36)$$

The terminal velocity has been normalized to surface conditions $v_{t,0}$ to remove the direct atmospheric effect (see Sec. 3.2) and ease comparison with the empirical equations of A. Heymsfield (1972) that assume a reference pressure of $p = 1000$ hPa.

The empirical mass-size-relations for aggregates, plates, columns, or broadly branched crystals of M96 may be able to estimate an average behavior of the mass-size spectrum for certain diameter ranges, but the variations caused by local temperature and supersaturation effects seem impossible to describe with prescribed thresholds or a mixture of static relations. Depending on the nucleation conditions prescribed by the initialization height and mass, the particles develop different characteristics for the same maximum dimension. For larger maximum dimensions, we see that the diagnostic geometry of aggregates tends to underestimate the prolate and overestimate the oblate particle mass, demonstrating the weakness of using the diagnostic approach for the differ-

ent regimes. Habit-specific relationships do not significantly improve the agreement, and to use them additional thresholds based on particle properties would have to be defined. This strongly emphasizes the importance of the HP for predicting ice growth in clouds.

Specifically for the mass of prolate particles, a sharp increase around $D = 0.4$ mm can be observed, accompanied by an increase in velocity and apparent density. This behavior cannot be matched by the slope of any empirical relation and exhibits a caveat of the deposition density description for secondary habits as formulated by JH15: the deposition density is generally dependent on the surrounding conditions and is assumed to approach ice density for the transition from prolate-favoring to oblate-favoring conditions (and vice versa) ($\Gamma \rightarrow 1 \Rightarrow \rho_{\text{app}} \rightarrow \rho_i$, cf. Eq. 7). Because the columns cannot satisfy the branching criterion of JH15, they grow with ice density not only when in regions that mandate spherical growth, but also when falling in oblate-favoring conditions where the addition of high-density mass causes acceleration (Fig. 16(b)). Coupled with the comparatively short residence times in habit-forming regimes due to high fall velocities, columns do not substantially change the habit they initially formed under conditions close to their nucleation height. The deposition density for habits growing in unfavorable conditions is unknown. Comparison with the empirical relation for apparent density suggests that the assumption of secondary habits (immediate onset and subsequent degree of hollowing) may be overstated.

Particles nucleated under oblate-favoring conditions can form relatively small ARs once they begin to branch. The development of a large area presented to the flow increases the drag, leading to an almost constant terminal velocity at large diameters. This feedback positively supports habit development in the prevailing atmospheric conditions. Compared with the empirical relation of the apparent density of dendrites, the onset of branching seems premature and further motivates our changes to the branching criterion. Oblates that fall into conditions of higher deposition density experience an increase in apparent density. It is unclear if this behavior can be physically motivated or is a feature of the coupling between IGF and deposition density. Hashino and Tripoli (2007) hypothesize that dendritic arms grow under prolate-favoring conditions due to an increased ventilation effect along the tips, while there is no current theory for columns. Future laboratory experiments may help to better understand this behavior and motivate a modified treatment of the modeled particles, but for now, we stick with the secondary habit treatment proposed by JH15.

To get a quantitative impression of the average effect of the habit prediction, Figure 17 shows the vertical profiles of mass flux, deposition rate, and mass-weighted terminal velocity \bar{v}_t . A comparison of particles following the m - D -relation of aggregates from Mitchell (1996, solid lines) with the original formulation of cylindrical hydrodynamic behavior of Böhm (1992a) (long-dashed, HP) shows that the habit prediction significantly reduces mass flux (precipitation rate, Fig. 17a). The diagnostic geometry predicts larger areas for particles of a certain maximum dimension than those of prolate spheroids of the habit prediction. This drastically increases the deposition rate (Fig. 17b) via the increased capacitance, while leading to lower fall velocities for the same mass (Fig. 17c). Slower particles prolong the residence time, leading to even more depositional growth that cannot be compensated for by the increased ventilation effect for the fast columnar particles. In turn, particles that follow the m - D -relationship can develop up to twice the mass flux of particles that develop a habit.

Using the interpolation for the velocity of prolates increases the observed difference and further reduces the mass flux due to the effective acceleration of the particles (see section 3.1). Upcoming results will only use the interpolated fall velocity for prolates due to consistency with laboratory results.

The behavior of particles nucleated under oblate-favoring conditions qualifies the results of the simplified experimental setup of Takahashi et al.: Plates generate more mass than particles with a diagnostic geometry, but the effect is less pronounced than for prolates. Even at higher masses, oblates have a slightly longer residence time than particles without a habit. The development of thin plates or dendritic structures increases

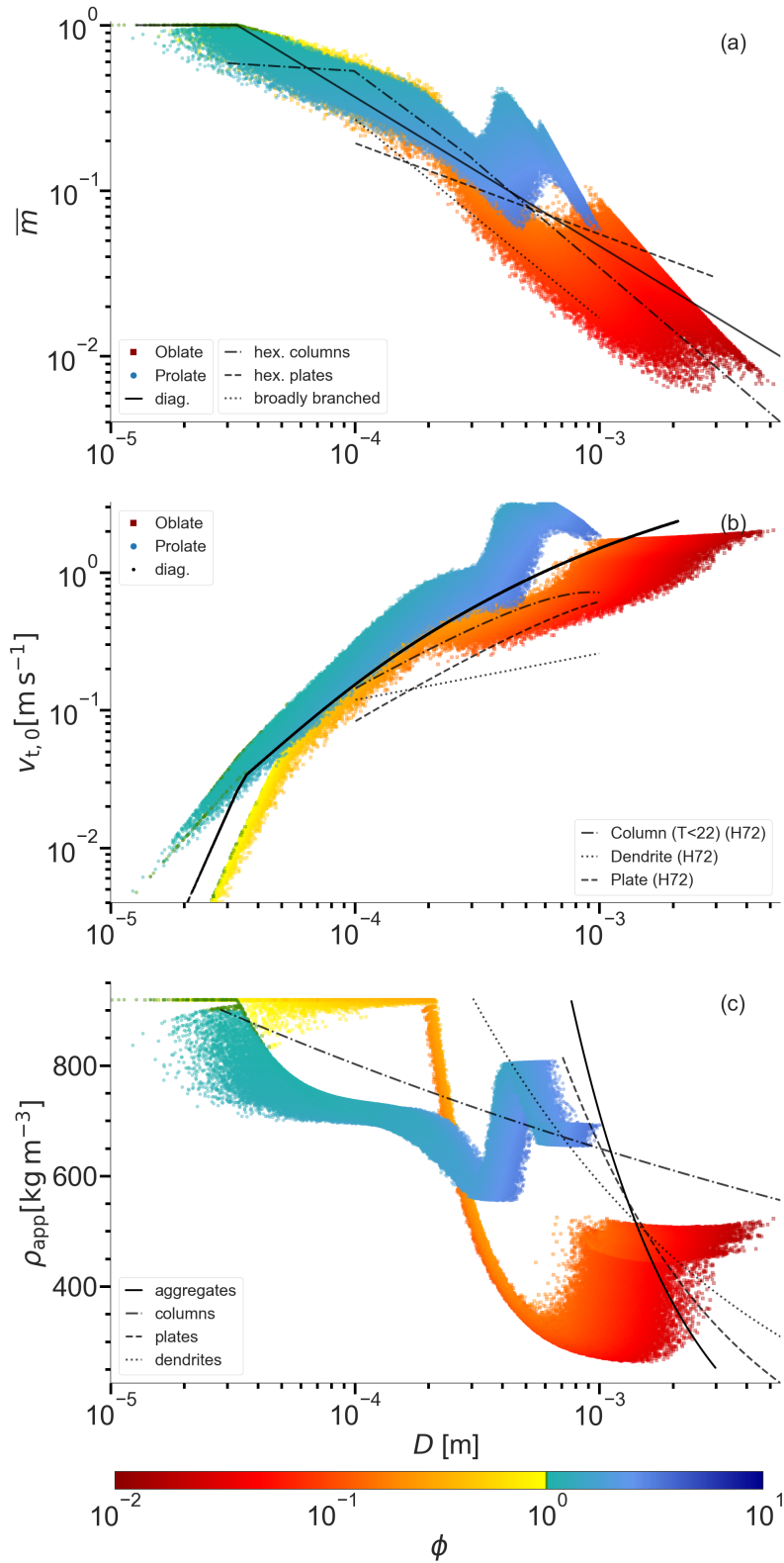


Figure 16. \bar{m} - D (a), $v_{t,0}$ - D (b), and ρ_{app} - D -relations (c) for the steady state of the simulation. Markers represent the simulations using a diagnostic geometry and an explicit habit prediction. The particles AR ϕ is color-coded. Lines in (a) are empirical relations of Mitchell (1996), in (b) of A. Heymsfield (1972), and in (c) from Pruppacher and Klett (1997).

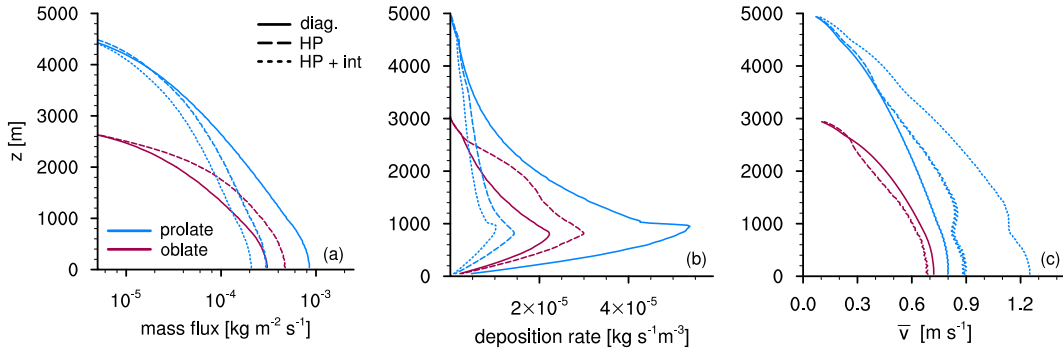


Figure 17. Comparison of vertical profiles of (a) mass flux, (b) deposition rate, and (c) mass-weighted velocity \bar{v} for particles nucleated in a prolate (blue, $\Delta z_{\text{nuc}} = 4500 - 5000$ m) and an oblate (red, $\Delta z_{\text{nuc}} = 2700 - 3000$ m) regime using a diagnostic geometry (solid), habit prediction with cylinder (dashed), and habit prediction with interpolated velocity for prolates (short-dashed).

625 the surface area, causing a positive feedback on capacitance and ventilation, amplified
 626 by habit-dependent ventilation, increasing the deposition rate.

627 An opposite effect on the first-order variables of the two categories of habits can
 628 be observed: the HP effectively causes an increase in precipitation mass for oblate par-
 629 ticles and a decrease for prolate particles (such as the mass flux/precipitation).

5.2.2 Updated IGF

630
 631 While we do not expect the effect of the updated habit scheme to be nearly as pro-
 632 nounced as in the isolated laboratory setup of Takahashi et al., the changes may initial-
 633 ize altered habit developments. In particular, particles nucleated in the cold prolate regime
 634 remain more spherical and are therefore more prone to primary habit change. Figure 18
 635 shows the changes in both growth regimes caused by the modifications of the IGF, in-
 636 cluding the branching criterion. The flattening of the prolate maximum in the cold regime
 637 ($T < 253$ K) leads to the evolution of fast falling crystals because their AR remains close
 638 to sphericity and their apparent density is comparatively high, improving the agreement
 639 with the empirical relation of the apparent density of columns. These crystals short resi-
 640 dence times result in reduced total depositional growth and maximum dimension, and
 641 ultimately shorter lifetimes as they fall out as precipitation.

642 The change in branching criterion delays the development of porous structures for
 643 plates, and the more compact shape results in an initially increased terminal fall veloc-
 644 ity. As soon as strong branching sets in, v_t reaches lower velocities as for the original branch-
 645 ing criterion closer to the empirical relation for dendrites of A. Heymsfield (1972). The
 646 delayed onset of branching agrees well with the empirical relation for the apparent den-
 647 sity of dendrites.

648 Generally, the modifications to the IGF and branching criterion show the desired
 649 impact on mass and apparent density while terminal velocities are fairly high.

650 The average vertical profiles in Figure 19 allow to summarize the quantitative behav-
 651 ior: The mass flux for plates following the original IGF is significantly increased compar-
 652 ed to the diagnostic counterpart. For the updated formulation, the mass flux is similar
 653 to that of particles without explicit habits. This highlights the importance of the ini-
 654 tial growth phase, where the exact onset of branching significantly affects the particle
 655 characteristics. The new IGF causes a decrease in mass flux for both the columnar and
 656 prolate cases compared to the original IGF configuration for similar reasons: While pro-
 657 lates remain more spherical and less hollow, oblates branch later and the more compact

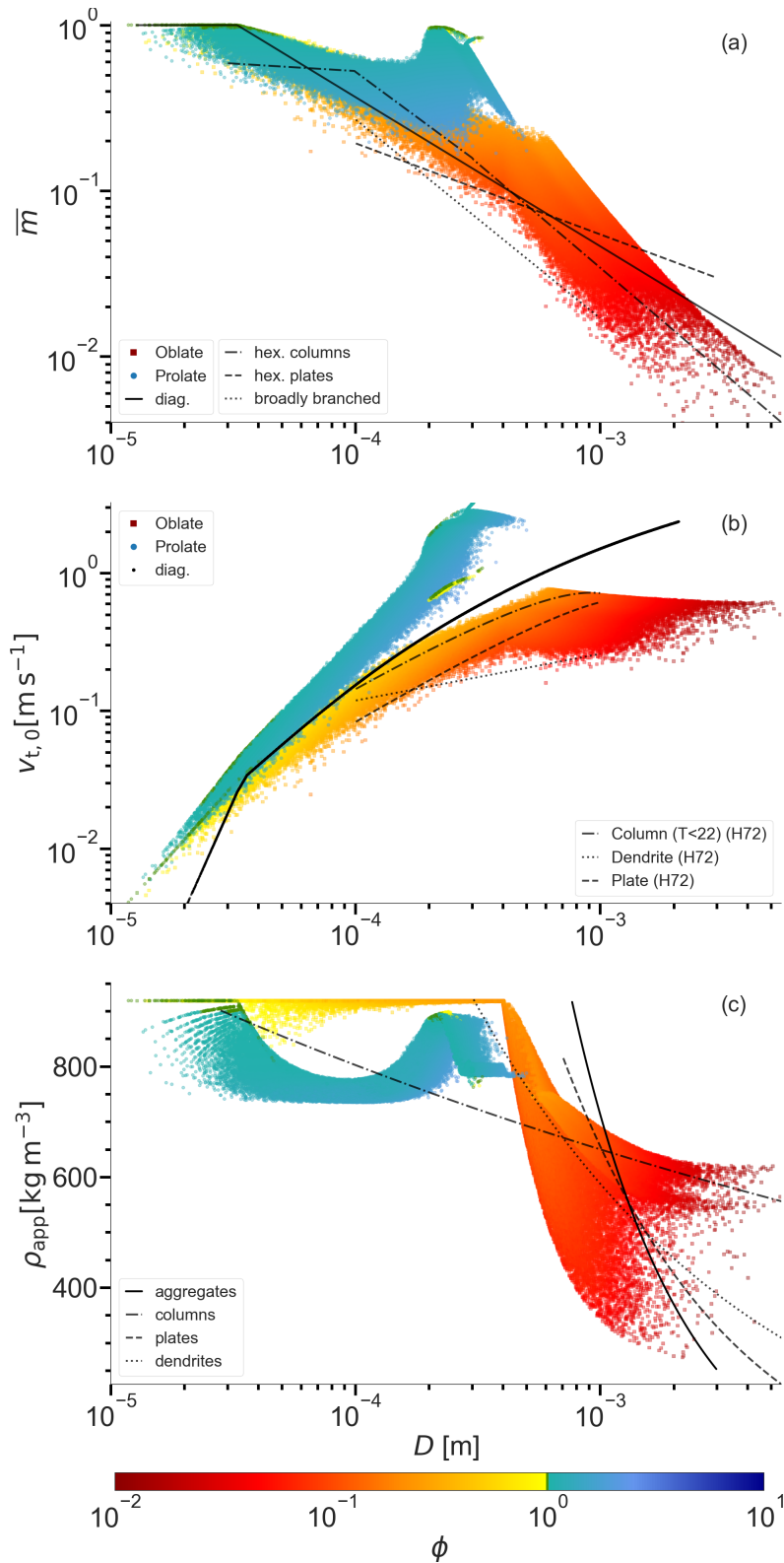


Figure 18. Same as Fig. 16 but using the updated IGF configuration. Lines in (a) are empirical relations of Mitchell (1996), in (b) of A. Heymsfield (1972), and in (c) from Pruppacher and Klett (1997).

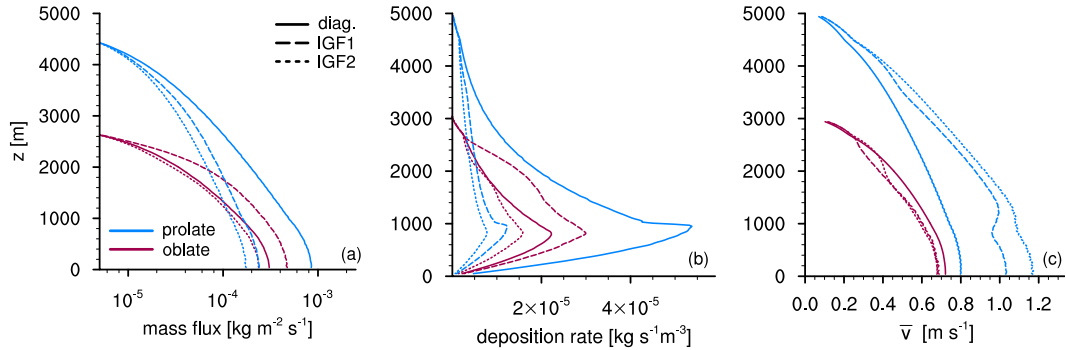


Figure 19. Comparison of vertical profiles of (a) mass flux, (b) deposition rate, and (c) mass-weighted velocity \bar{v} for particles nucleated in a prolate regime (blue, $\Delta z_{\text{nuc}} = 4500 - 5000$ m) and an oblate regime (red, $\Delta z_{\text{nuc}} = 2700 - 3000$ m) using a diagnostic geometry (solid), HP with original IGF (dashed), and HP with updated IGF (short-dashed).

658 geometry shortens the residence time. This can only be seen by comparing Fig. 16 and
 659 18 because the mass-weighted velocity (Fig 19c) does not show the effect of the lighter
 660 particles. The effect of the two IGF versions on habit development is visualized in Fig-
 661 ure 20. For reference, lines are plotted for ϕ - D -relations from Auer and Veal (1970), as-
 662 suming the corresponding nucleation temperature (columnar (dash-dotted) $T < 253$ K,
 663 Plc (dashed): $256 \text{ K} < T < 260 \text{ K}$). The ARs of the prolates developed for the origi-
 664 nal IGF (blue) are similar to those expected from the empirical relations in the corre-
 665 sponding temperature range. Using the new IGF instead, columnar particles develop sim-
 666 ilar ARs for lower D due to the removal of the size constraint on habit development, but
 667 for larger D their ARs are less pronounced and some particles even change their habit
 668 (highlighted in light blue). The classification of these particles is difficult, but they could
 669 be interpreted as complex polycrystals like capped columns. If they are polycrystals, this
 670 raises the question of the apparent density treatment. It seems unlikely that Eq. 7 can
 671 describe the development of secondary habits for polycrystalline structures, since for spheri-
 672 city the deposition densities are at or around ice density.

673 By removing the size constraint on habit development, planar particles (red) are
 674 able to develop strong aspect ratios close to $\phi = 10^{-2}$ (lower right corner) for the up-
 675 dated IGF including modifications. For very large D , the aspect ratios are similar to those
 676 expected from the empirical relation for dendrites.

677 We can conclude that the changes to the IGF and the branching criterion reduce
 678 the mass flux for both scenarios while allowing the development of very thin plates. It
 679 remains an open question how to deal with particles that change their habit, since the
 680 spheroidal approach is limited to simple geometries.

681 5.3 Aggregation

682 The three main factors influencing the aggregation process are the geometric area
 683 A , the fall velocity difference $\Delta v = |v_1 - v_2|$, and the collision efficiency E_c , which de-
 684 pends on the difference in v_t . The habit prediction scheme affects all of the above fac-
 685 tors by introducing variability in particle shape and density, broadening the velocity spec-
 686 trum, and potentially changing the cross sectional area. Here, we use the formulation
 687 from Mitchell (1988) for sticking efficiency, which prescribes piecewise linear values for
 688 temperature ranges. Intuitively, the habit prediction is expected to lead to altered, habit-
 689 specific aggregation rates that feedback on depositional growth. Figure 21 shows the ver-
 690 tical profiles of number density (left column) and mass flux (right column) for the oblate
 691 (top row) and prolate (bottom row) cases, separated into monomers and aggregates. The

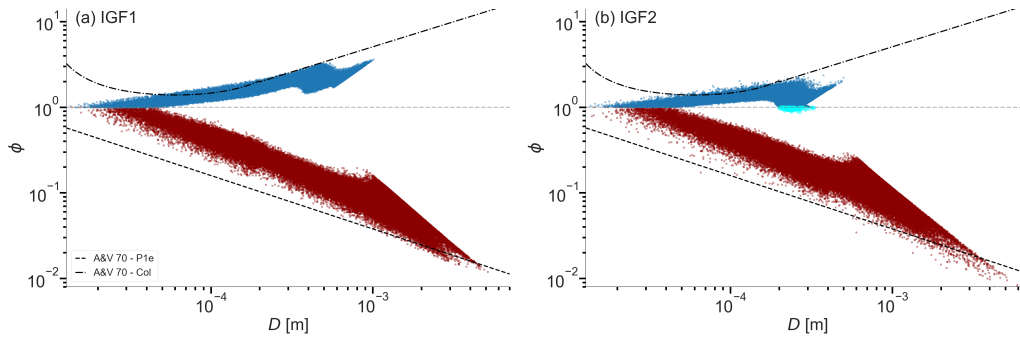


Figure 20. ϕ - D -relations of the two cases for the original IGF (a) and the updated version with modifications (b). The black lines are empirical relations from Auer and Veal (1970).

vertical number density profiles show that the different descriptions of depositional growth and geometry have critical effects on aggregation. The development of dendritic crystals causes an earlier and stronger initial aggregation rate compared to particles without HP and is strongest for the original IGF (crystals branch earlier). Both IGF configurations show a reduction in monomer number density, but the earlier branching critically influences the onset of aggregation and the additional collection of both monomers and aggregates further down. This causes the mass flux for the original IGF to be dominated by aggregates. The number of aggregates for the modified IGF is almost independent of height, indicating that aggregates mainly collect other monomers rather than self-collection of monomers or aggregates. Analysis of the number of monomers per aggregate confirms that mostly large monomers are collected, while smaller crystals rarely aggregate (not shown). Oblate particles grow efficiently by vapor growth and their collection by aggregation does not transfer its positive effects to the aggregates because we assume that their geometry is reduced to the m - D power law. This leads to a reduction in the total mass flux when the HP is compared to the classical m - D -relationship, indicating the effect of the simplified aggregation geometry that immediately forgets the monomer information. A difference between the two IGF configurations for the composition of the total mass flux at the surface is present: for the original IGF, the mass flux is dominated by aggregates and close to equality for the new configuration. The higher total number density leads to more depositional growth because the supersaturation is fixed. If there would be an interactive feedback between hydrometeors and the atmosphere, higher number densities would lead to a faster depletion of the supersaturation.

The prolate case shows the opposite behavior: the reduced depositional growth compared to particles without explicit habit, caused by shorter residence times, leads to smaller cross sectional areas, which in turn decreases the aggregation rates. Particles with a diagnostic geometry, on the other hand, start to aggregate efficiently in the lower half of the domain, where the sticking efficiency is high, so that the number densities of monomers and aggregates constantly decrease and large aggregates form. Aggregates dominate the mass flux when no habits can develop, while for the HP the mass flux is defined by that of the monomers.

The habit prediction has a significant impact on the aggregation of the cases studied. The impact depends on the dominant primary habit, but could be overestimated because in the specific cases no different primary habits coexist that would lead to potentially high aggregation rates.

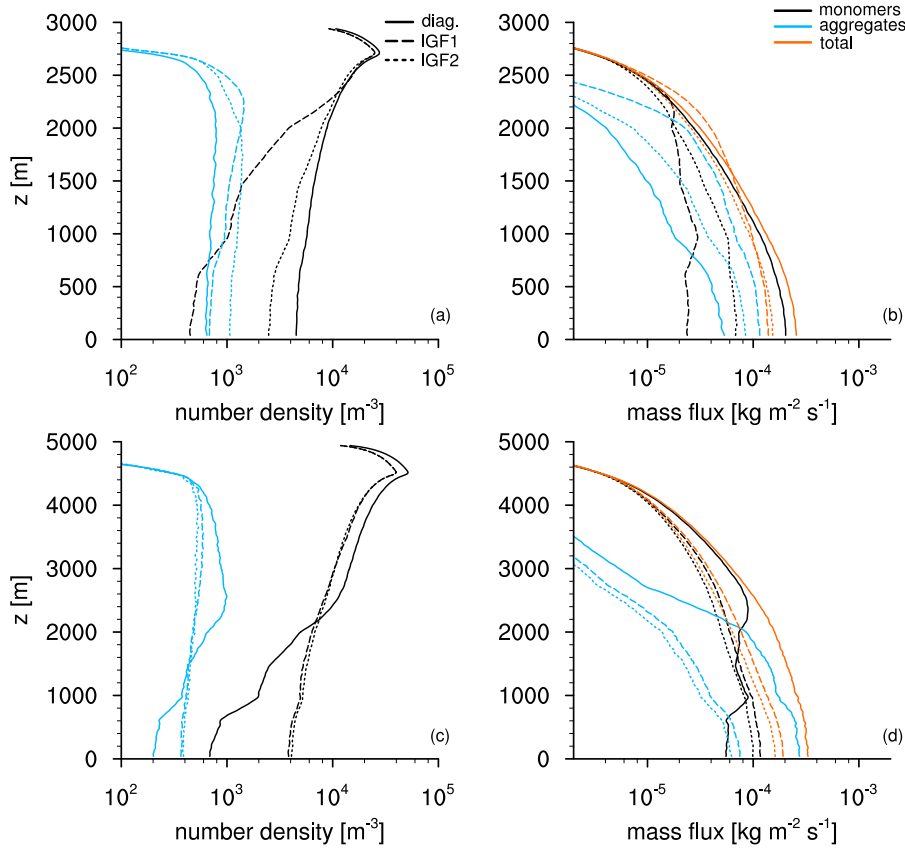


Figure 21. Vertical profiles of number density (a & c) and mass flux (b & d) for monomers (black) and aggregates (blue) for the oblate (top row) and prolate (bottom row) nucleation regimes using a diagnostic geometry (solid), HP with original IGF (dashed), and HP with updated IGF (short-dashed) with deposition and aggregation enabled.

726

5.4 Riming

727

Finally, we enable riming by specifying a liquid water zone in the bottom 20% of the domain (Fig. 22). Particles are classified as rimed as soon as they contain rime mass. For low LWCs, the transition from prolate/oblate monomers may be slow, and habit effects caused by deposition may persist, but high LWCs lead to effective rounding of particles, which can then be described by m - D -relations for rimed particles or graupel (as shown by Jensen and Harrington (2015)).

733

734

735

736

737

738

739

740

741

742

743

744

For the chosen conditions, all particles are large enough to rime immediately upon reaching the LWZ, regardless of configuration. Riming increases the mass and area of the particles while accelerating them, increasing the rate of aggregation and leading to a further decrease in number density. The immediate effect of the added rime mass is to fill the porous structures before effectively increasing the maximum dimension. For particles that do not develop a habit, this leads to a dominance of the acceleration effect over the geometric change. Regardless of the primary habit, particles that are allowed to evolve habits are effectively dragged toward sphericity by the assumption that riming only increases the minor dimension (see Eq. 18 & 19). Therefore, riming accelerates the most pronounced evolved habit through mass growth and rounding. IGF configuration has a weak effect on riming compared to deposition and aggregation. Only for prolates following the original IGF can a more pronounced decrease in number density

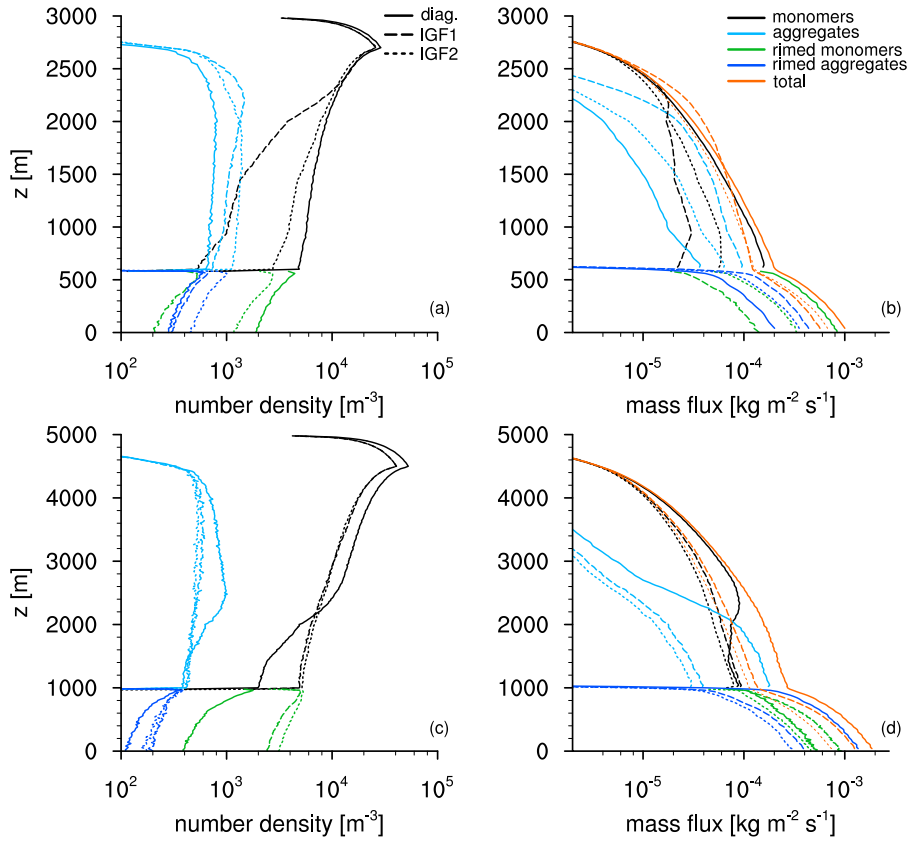


Figure 22. Vertical profiles of number density (a & c) and mass flux (b & d) for monomers (black), aggregates (black), rimed monomers (green), and rimed aggregates (dark blue) for the oblate (top row) and prolate nucleation regimes (bottom row) using a diagnostic geometry (solid), HP with original IGF (dashed), and HP with updated IGF (short-dashed) with all processes enabled.

745 in the LWZ be observed, because the cross-sectional area is more effectively changed by
 746 rounding when more pronounced ARs have developed.

747 6 Conclusion

748 The LPM *McSnow* has been expanded by an extended version of the habit prediction
 749 scheme of Jensen and Harrington (2015), based on the work of J.-P. Chen and Lamb
 750 (1994b). The comprehensive hydrodynamic description of porous spheroids by Böhm adds
 751 parameterizations regarding terminal velocity and collision efficiency. We propose a mass-
 752 dependent interpolation of the terminal velocity between prolate and cylindrical parti-
 753 cles based on the laboratory results of McCorquodale and Westbrook (2021), which over-
 754 comes the massive deceleration resulting from the cylindrical assumption of Böhm when
 755 transitioning from spherical to prolate or vice versa. A shape-dependent ventilation co-
 756 efficient has been introduced that combines the results of a collection of recent studies
 757 on ventilation of different geometries. While the effect on depositional growth is found
 758 to be in the range of a few percent for small particles, for larger particles the ventilation
 759 coefficients can increase by a factor of two compared to spheres. The habit prediction
 760 scheme in its original version was shown to be in good agreement with individual parti-
 761 cle measurements from Takahashi et al. (1991), but also has deficiencies, including the
 762 polycrystalline regime, the warm prolate maximum, and the branching criterion used for

763 oblate particles. A comparison with an independent method using the polarizability ra-
 764 tio of Myagkov, Seifert, Bauer-Pfundstein, and Wandinger (2016) confirmed these find-
 765 ings. Hence, we propose a modified version of the IGF combined with a modified branch-
 766 ing criterion. These modifications were found to improve the results under constant con-
 767 ditions in an appropriate way. The importance of explicit habit prediction for deposi-
 768 tion, aggregation and, in part, riming was demonstrated in a simplified 1-D snow shaft
 769 simulation. Columnar particles fall faster than their counterparts without explicit habits,
 770 and the shortened residence time leads to less ice mass, independent of the IGF config-
 771 uration. The reduced mass translates into rather weak aspect ratios and the resulting
 772 smaller cross-sectional areas significantly reduce the aggregation rate. However, riming
 773 is highly effective and partially enhances aggregation due to the assumed effective round-
 774 ing increasing the cross-sectional area. For the original IGF configuration, this effect is
 775 most pronounced because of the more pronounced ARs that develop due to the prolate
 776 maximum around the nucleation temperature.

777 The deposition rate of the plates is significantly increased compared to the *m-D*-
 778 particles for the original IGF at lower fall velocities, especially for large particles, result-
 779 ing in a higher mass flux. The planar geometry has a positive effect on the aggregation
 780 rate, with the opposite effect observed for prolates. The habit effect is partially mitigated
 781 when using the modified branching criterion: particles branch later, stay denser, accel-
 782 erate more, and grow slower than for the original IGF. In turn, the aggregation rates de-
 783 crease, but are still higher than when no habits are formed. It remains an open ques-
 784 tion when oblate particles branch, but the proposed approach showed reasonable results.
 785 Future laboratory studies could be aimed at understanding the deposition behavior un-
 786 der unfavorable habit conditions e.g. oblate particles growing in an environment that
 787 favors prolate growth.

788 Finally, large LWCs rapidly transform planar crystals into rimed particles once they
 789 reach the onset of riming. If the threshold is already exceeded when entering the LWZ,
 790 we do not find a significant effect of habit prediction on riming rates.

791 Given the importance of ice-microphysical processes in mixed-phase clouds, ice habits
 792 are highly influential and affect cloud lifetime. The variability of atmospheric conditions
 793 shapes individual particles whose characteristics cannot be generalized by broad clas-
 794 sifications. The chosen 1-D scenarios can only describe parts of the impact of an explicit
 795 habit prediction on process rates, but they already emphasize that it is of first order. By
 796 design, the setup does not allow the atmosphere to change dynamically, but these effects
 797 should play a role in the competition for water vapor and ultimately alter precipitation
 798 rates. More sophisticated atmospheric simulations could be set up to try to reproduce
 799 the interactions between different habits that are present simultaneously. Coupling *Mc-*
 800 *Snow* with the ICON model (Zängl et al., 2015) is a next step in achieving such realis-
 801 tic atmospheric simulations.

802 In addition, the detailed information on particle properties shall be compared with
 803 polarimetric measurements to show the validity of the model and to be used as a numer-
 804 ical laboratory to study microphysical processes in clouds.

805 Appendix A Böhm's theory

806 In the following, the reader can find the sets of equations of Böhm's theory to cal-
 807 culate the terminal velocity and collision efficiency using BLT.

808 A1 Terminal fall velocity

809 For both oblate and prolate particles, Böhm defines the characteristic length scale
 810 as the equatorial diameter $d_{\text{char}} = 2a$ instead of the maximum dimension (also men-

811 tioned by (Shima et al., 2020)).

$$X(m, \phi, q) = \frac{8 m_i g \rho_a}{\pi \mu^2 \max(\phi; 1) \max(q^{1/4}; q)}, \quad (\text{A1a})$$

$$k(\phi) = \min \left(\max(0.82 + 0.18 \phi; 0.85); \left(0.37 + \frac{0.63}{\phi} \right); \frac{1.33}{\max(\log \phi; 0) + 1.19} \right), \quad (\text{A1b})$$

$$\Gamma_\phi = \max \left(1; \min(1.98; 3.76 - 8.41 \phi + 9.18 \phi^2 - 3.53 \phi^3) \right), \quad (\text{A1c})$$

$$C_{\text{DP,S}} = \max \left(0.292 k \Gamma_\phi; 0.492 - \frac{0.2}{\sqrt{\phi}} \right), \quad (\text{A1d})$$

$$C_{\text{DP}} = \max(1; q(1.46q - 0.46)) C_{\text{DP,S}}, \quad (\text{A1e})$$

$$C'_{\text{DP}} = C_{\text{DP}} \frac{1 + (X/X_0)^2}{1 + 1.6(X/X_0)^2}, \quad \text{with } X_0 = \begin{cases} 2.8 \times 10^6, & \text{ice particles,} \\ 6.7 \times 10^6, & \text{water particles,} \end{cases} \quad (\text{A1f})$$

$$C_{\text{D0}} = 4.5 k^2 \max(\phi; 1), \quad (\text{A1g})$$

$$\beta = \left[1 + \frac{C_{\text{D0}} - C_{\text{DP}}}{6k} \left(\frac{X'}{C'_{\text{DP}}} \right)^{1/2} \right]^{1/2} - 1, \quad (\text{A1h})$$

$$\gamma = \frac{C_{\text{D0}} - C_{\text{DP}}}{4 C_{\text{DP}}}, \quad (\text{A1i})$$

$$N_{\text{Re}} = \frac{6k}{C'_{\text{DP}}} \beta^2 \left[1 + \frac{2\beta e^{-\beta\gamma}}{(2+\beta)(1+\beta)} \right], \quad (\text{A1j})$$

$$C_{\text{DI}} = \frac{X}{N_{\text{Re}}^2} - \frac{24k}{N_{\text{Re}}}, \quad (\text{A1k})$$

$$v_t = \frac{\mu N_{\text{Re}}}{\rho_a d_{\text{char}}}. \quad (\text{A1l})$$

812 The used variables are the Best number X , the turbulence modified Best number X' ,
 813 the dynamic viscosity μ , the air density ρ_a , the viscous shape parameter k , a function
 814 regarding the aspect ratio Γ_ϕ , the drag coefficient $C_{\text{DP,S}}$, the drag coefficient fitted for
 815 prolates C_{DP} , the Oseen drag coefficient C_{D0} , the inertial drag coefficient C_{DI} , the char-
 816 acteristic length scale d_{char} , and some helper variables β, γ . The minimum and maximum
 817 functions are used to constrain transitions from very oblate over quasi-spherical to very
 818 prolate particles. For more details on the derivation, the reader is referred to Böhm (1989)
 819 and Böhm (1992a). The middle term of formula A1c is found with and without the square
 820 root of the aspect ratio in the denominator (see Eq. 13 in (Böhm, 1992a) and Eq. 9 in
 821 (Böhm, 1999)). Analysis indicates that for a consistent transition the version from Böhm
 822 (1992a) should be correct while differences are marginal.

823 A2 Collision efficiency

$$F = \sqrt{G^2 + \frac{C_{\text{I},1} v_{\text{I1}}^2}{C_{\text{DI}}^* |v_1 - v_2|^2}}, \quad (\text{A2a})$$

$$G = \frac{6 \mu_a}{\rho_a r^* |v_1 - v_2| C_{\text{DI}}^*}, \quad (\text{A2b})$$

$$H = \frac{2m^*}{\rho_a \pi r^{*2} C_{\text{DI}}^* \delta}, \quad (\text{A2c})$$

$$v_{\text{I1}} = \frac{2+j}{4} v_1. \quad (\text{A2d})$$

$$(\text{A2e})$$

C_{DI}^* is the inertial drag coefficient with respect to r^* and the initial velocity while $C_{\text{I},1}$ refers to the bigger particle properties. While the latter is determined by Eq. A1l, C_{DI}^* is found by Eq. A1f-g and

$$C_{\text{DI}}^* = C'_{\text{DP}} \left(1 + \frac{4}{\beta} (1 - e^{-\gamma\beta}) \right), \quad (\text{A3})$$

824 to match the value of C_{DI} with the value from Oseen theory at low Reynolds numbers.

825 The two-body system is characterized by the radius r^* , mass m^* , area of intersec-
826 tion A^* , initial velocity v^* , and boundary layer thickness δ_s^*

$$r^* = \frac{r_1 r_2}{r_1 + r_2} = \sqrt{A^*/\pi}, \quad (\text{A4a})$$

$$m^* = \frac{m_1 m_2}{m_1 + m_2}, \quad (\text{A4b})$$

$$A^* = \pi r^{*2} = \frac{A_1 A_2}{\pi (r_{e1} + r_{e2})}, \quad (\text{A4c})$$

$$v^* = \max(|v_1 - v_2|; v_{\min}), \quad (\text{A4d})$$

$$\delta_s^* = \delta_{s1} \sqrt{v_1/v^*} + \delta_{s2} \sqrt{v_2/v^*}. \quad (\text{A4e})$$

827 For v^* , a minimum value is assumed ($v_{\min} = 10^{-10} \text{ m s}^{-1}$) because for equally fast par-
828 ticles the difference would approach zero, leading to a division by zero in Eq. A2a and
829 A2b.

In the case of an oblate particle, the equivalent circular radius r_e is the equatorial radius r but for prolate particles the definition changes to

$$r_e = \left(\frac{4\phi}{\pi} \right)^{1/2} r_1, \quad (\text{A5})$$

830 following the special assumptions of columns to be better approximated by a cylindri-
831 cal shape. In Böhm (1999), he also especially mentions that in case of columns or irreg-
832 ularly shaped aggregates the equivalent circular definition shall be used. In a general-
833 ized form for all particle shapes they can be written as

$$r_e = \sqrt{A/\pi}, \quad (\text{A6a})$$

$$\phi_e = \min(\phi; 1) \frac{r}{r_e}, \quad (\text{A6b})$$

$$q_e = \begin{cases} \pi q/4, & q > 1, \\ q, & q \leq 1, \end{cases} = q \left[1 - \frac{\max(q-1; 0)}{q-1} \left(1 - \frac{\pi}{4} \right) \right]. \quad (\text{A6c})$$

To fully define the shape characteristics of the two-body system, we additionally need to give definitions of the equivalent aspect ratio and porosity. Simple averaging of these quantities might lead to strong over- or underestimation. Hence, we use the radius weighted mean of those characteristics (Böhm, 1999)

$$\xi^* = r^* \left(\frac{\xi_1}{r_{e1}} + \frac{\xi_2}{r_{e2}} \right) \quad (\xi = q, \phi), \quad (\text{A7})$$

834 where the indices refer to the corresponding particle.

For anisotropic particles, the velocity v_1 has to be replaced by a characteristic velocity

$$v'_1 = \begin{cases} \phi_1 v_1 & , \text{for plates,} \\ \frac{3}{4} v_1 & , \text{for columns.} \end{cases} \quad (\text{A8})$$

835 Variables used in the flow correction for potential flow are defined as

$$t_\delta = \begin{cases} \frac{c_y}{\Delta_y} \arctan \frac{\Delta_y}{b c_y - 1}, & (b c_y \geq 1), \\ \frac{c_y}{\Delta_y} (\pi - \arctan \frac{\Delta_y}{1 - b c_y}), & (\frac{1}{2} < b c_y < 1), \end{cases} \quad (\text{A9a})$$

$$c_i = \frac{m_2}{3 k_{2,i} \pi r_2 \eta_a} \quad (i = x, y), \quad (\text{A9b})$$

$$b = \frac{3v}{r_{e,1} \delta_1}, \quad (\text{A9c})$$

$$\Delta_x = \sqrt{2b c_x / j + 1}, \quad (\text{A9d})$$

$$\Delta_y = \sqrt{2b c_y - 1}. \quad (\text{A9e})$$

The shape factor $k_{2,x}$ does not describe the same quantity as in Eq. A1c because this is defined perpendicular to the axis of symmetry in case of a plate or as the arithmetic mean

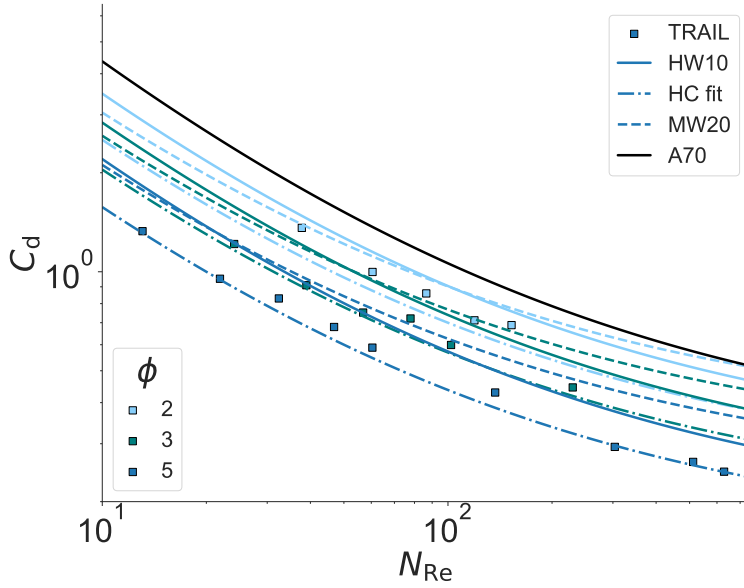


Figure A1. Fits for the $N_{\text{Re}}-C_d$ -relations compared with data of hexagonal columns from TRAIL (colored squares). Black line corresponds to the solution of spheres by Abraham (1970, A70), solid lines are the generalized relation of A. J. Heymsfield and Westbrook (2010, HW10), dashed lines mark results of McCorquodale and Westbrook (2021, MW20), and dash-dotted lines show our fit for hexagonal columns (HC) only. The assumed aspect ratio is color coded

of the two shape factors parallel and perpendicular to the axis for a column. It can be approximated by

$$k_{2,x} \approx \begin{cases} 0.57 + 0.43\phi, & (\phi < 1), \\ k^{1.15}, & (\phi > 1). \end{cases} \quad (\text{A10})$$

836

A3 Shape assumption for columns

837

Figure A1 shows fits of Eq. 30 of Abraham (1970, A70), A. J. Heymsfield and Westbrook (2010, HW10), McCorquodale and Westbrook (2021, MW20), and our fit (HC fit) compared against the TRAIL data for hexagonal columns.

839

840

Appendix B Open Research

841

McSnow is part of the ICON modeling framework and the code is available under two different licenses: A personal non-commercial scientific license, and an institutional license that requires a cooperation agreement with DWD. More details on the licenses and an instruction how to obtain the ICON code can be found at <https://code.mpimet.mpg.de/projects/iconpublic>. Access to the McSnow repository can be granted on request as soon as an ICON license agreement has been signed. Data and post-processing script are available from Zenodo at <https://doi.org/10.5281/zenodo.7900348>. The repository includes a modified copy of the data from McCorquodale and Westbrook (2021) found in the "Supporting Information" section]TRAIL2021b.

849

Acknowledgments

The in-depth analysis of the Böhm parameterization would not have been so fruitful without the data set of the TRAIL campaign. We, therefore, like to thank Christopher D. Westbrook for sharing the data and providing insight. Furthermore, we would like to thank Alexander Myagkov for sharing the routines used to calculate the polarizability ratio from shape and density. This work has been funded by the German Science Foundation (DFG) under grant SE 1784/3-1, project ID 408011764 as part of the DFG priority program SPP 2115 on radar polarimetry.

References

- Abraham, F. F. (1970). Functional dependence of drag coefficient of a sphere on reynolds number. *The Physics of Fluids*, *13*(8), 2194-2195. Retrieved from <https://aip.scitation.org/doi/abs/10.1063/1.1693218> doi: 10.1063/1.1693218
- Auer, A. H., & Veal, D. L. (1970). The dimension of ice crystals in natural clouds. *J. Atmos. Sci.*, *27*(6), 919 - 926. Retrieved from https://journals.ametsoc.org/view/journals/atsc/27/6/1520-0469_1970_027_0919_tdoici_2_0_co_2.xml doi: 10.1175/1520-0469(1970)027<0919:TDOICI>2.0.CO;2
- Bailey, M. P., & Hallett, J. (2009, 9). A comprehensive habit diagram for atmospheric ice crystals: Confirmation from the laboratory, airs ii, and other field studies. *J. Atmos. Sci.*, *66*, 2888-2899. Retrieved from <http://journals.ametsoc.org/doi/abs/10.1175/2009JAS2883.1> doi: 10.1175/2009JAS2883.1
- Baran, A. J. (2012). From the single-scattering properties of ice crystals to climate prediction: A way forward. *Atmos. Res.*, *112*, 45 - 69. Retrieved from <http://www.sciencedirect.com/science/article/pii/S0169809512001160> doi: 10.1016/j.atmosres.2012.04.010
- Beard, K. V. (1980). The effects of altitude and electrical force on the terminal velocity of hydrometeors. *J. Atmos. Sci.*, *37*(6), 1363 - 1374. Retrieved from https://journals.ametsoc.org/view/journals/atsc/37/6/1520-0469_1980_037_1363_teoaae_2_0_co_2.xml doi: 10.1175/1520-0469(1980)037<1363:TEOAAE>2.0.CO;2
- Brdar, S., & Seifert, A. (2018). Mcsnow: A monte-carlo particle model for riming and aggregation of ice particles in a multidimensional microphysical phase space. *J. Adv. Model Earth Sy.*, *10*(1), 187-206. Retrieved from <https://agupubs.onlinelibrary.wiley.com/doi/abs/10.1002/2017MS001167> doi: 10.1002/2017MS001167
- Bringi, V., Seifert, A., Wu, W., Thurai, M., Huang, G. J., & Siewert, C. (2020, 8). Hurricane dorian outer rain band observations and 1d particle model simulations: A case study. *Atmosphere*, *11*, 879. Retrieved from <https://www.mdpi.com/2073-4433/11/8/879/htm> doi: 10.3390/ATMOS11080879
- Böhm, J. P. (1989). A general equation for the terminal fall speed of solid hydrometeors. *J. Atmos. Sci.*, *46*(15), 2419-2427. Retrieved from [https://doi.org/10.1175/1520-0469\(1989\)046<2419:AGEFTT>2.0.CO;2](https://doi.org/10.1175/1520-0469(1989)046<2419:AGEFTT>2.0.CO;2) doi: 10.1175/1520-0469(1989)046<2419:AGEFTT>2.0.CO;2
- Böhm, J. P. (1990). *On the hydrodynamics of cloud and precipitation particles* (Doctoral dissertation, ETH Zurich). doi: 10.3929/ethz-a-000578177
- Böhm, J. P. (1992a). A general hydrodynamic theory for mixed-phase microphysics. part i: drag and fall speed of hydrometeors. *Atmos. Res.*, *27*(4), 253 - 274. Retrieved from <http://www.sciencedirect.com/science/article/pii/S0169809592900359> doi: 10.1016/0169-8095(92)90035-9
- Böhm, J. P. (1992b). A general hydrodynamic theory for mixed-phase microphysics. part ii: collision kernels for coalescence. *Atmos. Res.*, *27*(4), 275 - 290. Retrieved from <http://www.sciencedirect.com/science/article/pii/S0169809592900359>

- 016980959290036A doi: 10.1016/0169-8095(92)90036-A
- 903 Böhm, J. P. (1992c). A general hydrodynamic theory for mixed-phase micro-
 904 physics. part iii: Riming and aggregation. *Atmos. Res.*, *28*(2), 103 - 123.
 905 Retrieved from [http://www.sciencedirect.com/science/article/pii/](http://www.sciencedirect.com/science/article/pii/0169809592900234)
 906 [0169809592900234](http://www.sciencedirect.com/science/article/pii/0169809592900234) doi: 10.1016/0169-8095(92)90023-4
- 907 Böhm, J. P. (1994). Theoretical collision efficiencies for riming and aerosol
 908 impaction. *Atmos. Res.*, *32*(1), 171 - 187. Retrieved from [http://](http://www.sciencedirect.com/science/article/pii/0169809594900582)
 909 www.sciencedirect.com/science/article/pii/0169809594900582 doi:
 910 [10.1016/0169-8095\(94\)90058-2](https://doi.org/10.1016/0169-8095(94)90058-2)
- 911 Böhm, J. P. (1999). Revision and clarification of “a general hydrodynamic theory
 912 for mixed-phase microphysics”. *Atmos. Res.*, *52*(3), 167 - 176. Retrieved from
 913 <http://www.sciencedirect.com/science/article/pii/S0169809599000332>
 914 doi: 10.1016/S0169-8095(99)00033-2
- 915 Böhm, J. P. (2004). Reply to comment on “revision and clarification of ‘a gen-
 916 eral hydrodynamic theory for mixed-phase microphysics’ [böhm j.p., 1999,
 917 *atmos. res.* 52, 167–176]”. *Atmos. Res.*, *69*(3), 289 - 293. Retrieved from
 918 <http://www.sciencedirect.com/science/article/pii/S016980950300125X>
 919 doi: 10.1016/j.atmosres.2003.10.001
- 920 Chen, J.-P., & Lamb, D. (1994a, 09). Simulation of Cloud Microphysical and Chem-
 921 ical Processes Using a Multicomponent Framework. Part I: Description of the
 922 Microphysical Model. *J. Atmos. Sci.*, *51*(18), 2613-2630. Retrieved from
 923 [https://doi.org/10.1175/1520-0469\(1994\)051<2613:SOCMAC>2.0.CO;2](https://doi.org/10.1175/1520-0469(1994)051<2613:SOCMAC>2.0.CO;2)
 924 doi: 10.1175/1520-0469(1994)051(2613:SOCMAC)2.0.CO;2
- 925 Chen, J.-P., & Lamb, D. (1994b). The theoretical basis for the parameterization
 926 of ice crystal habits: Growth by vapor deposition. *J. Atmos. Sci.*, *51*(9), 1206-
 927 1222. Retrieved from [https://doi.org/10.1175/1520-0469\(1994\)051<1206:](https://doi.org/10.1175/1520-0469(1994)051<1206:TTBFTP>2.0.CO;2)
 928 [TTBFTP>2.0.CO;2](https://doi.org/10.1175/1520-0469(1994)051<1206:TTBFTP>2.0.CO;2) doi: 10.1175/1520-0469(1994)051(1206:TTBFTP)2.0.CO;2
- 929 Chen, Y., Jiang, P., Xiong, T., Wei, W., Fang, Z., & Wang, B. (2021, 11). Drag and
 930 heat transfer coefficients for axisymmetric nonspherical particles: A lbm study.
 931 *Chem. Eng. J.*, *424*, 130391. doi: 10.1016/J.CEJ.2021.130391
- 932 Connolly, P. J., Emersic, C., & Field, P. R. (2012). A laboratory investigation into
 933 the aggregation efficiency of small ice crystals. *Atmos. Chem. Phys.*, *12*, 2055-
 934 2076. doi: 10.5194/acp-12-2055-2012
- 935 Dias Neto, J., Kneifel, S., Ori, D., Trömel, S., Handwerker, J., Bohn, B., ... Sim-
 936 mer, C. (2019). The triple-frequency and polarimetric radar experiment for
 937 improving process observations of winter precipitation. *Earth Syst. Sci. Data*,
 938 *11*(2), 845–863. Retrieved from [https://essd.copernicus.org/articles/](https://essd.copernicus.org/articles/11/845/2019/)
 939 [11/845/2019/](https://essd.copernicus.org/articles/11/845/2019/) doi: 10.5194/essd-11-845-2019
- 940 Dziekan, P., Waruszewski, M., & Pawlowska, H. (2019, 7). University of warsaw
 941 lagrangian cloud model (uwlcm) 1.0: a modern large-eddy simulation tool for
 942 warm cloud modeling with lagrangian microphysics. *Geosci. Model Dev.*, *12*,
 943 2587-2606. Retrieved from [https://www.geosci-model-dev.net/12/2587/](https://www.geosci-model-dev.net/12/2587/2019/)
 944 [2019/](https://www.geosci-model-dev.net/12/2587/2019/) doi: 10.5194/gmd-12-2587-2019
- 945 Field, P. R., Hogan, R. J., Brown, P. R. A., Illingworth, A. J., Choulaton, T. W.,
 946 Kaye, P. H., ... Greenaway, R. (2004). Simultaneous radar and aircraft ob-
 947 servations of mixed-phase cloud at the 100 m scale. *Q. J. Roy. Meteor. Soc.*,
 948 *130*(600), 1877-1904. Retrieved from [https://rmets.onlinelibrary.wiley](https://rmets.onlinelibrary.wiley.com/doi/abs/10.1256/qj.03.102)
 949 [.com/doi/abs/10.1256/qj.03.102](https://rmets.onlinelibrary.wiley.com/doi/abs/10.1256/qj.03.102) doi: 10.1256/qj.03.102
- 950 Fukuta, N. (1969). Experimental studies on the growth of small ice crys-
 951 tals. *J. Atmos. Sci.*, *26*(3), 522-531. Retrieved from [https://doi.org/](https://doi.org/10.1175/1520-0469(1969)026<0522:ESOTGO>2.0.CO;2)
 952 [10.1175/1520-0469\(1969\)026<0522:ESOTGO>2.0.CO;2](https://doi.org/10.1175/1520-0469(1969)026<0522:ESOTGO>2.0.CO;2) doi: 10.1175/
 953 [1520-0469\(1969\)026\(0522:ESOTGO\)2.0.CO;2](https://doi.org/10.1175/1520-0469(1969)026<0522:ESOTGO>2.0.CO;2)
- 954 Gavze, E., & Khain, A. (2022). Gravitational collision of small nonspheri-
 955 cal particles: Swept volumes of prolate and oblate spheroids in calm air.
 956 *J. Atmos. Sci.*, *79*(6), 1493 - 1514. Retrieved from <https://journals>
- 957

- 958 .ametsoc.org/view/journals/atsc/79/6/JAS-D-20-0336.1.xml doi:
959 10.1175/JAS-D-20-0336.1
- 960 Hall, W. D., & Pruppacher, H. R. (1976). The survival of ice particles falling
961 from cirrus clouds in subsaturated air. *J. Atmos. Sci.*, *33*(10), 1995-2006.
962 Retrieved from [https://doi.org/10.1175/1520-0469\(1976\)033<1995:
963 TSOIPF>2.0.CO;2](https://doi.org/10.1175/1520-0469(1976)033<1995:TSOIPF>2.0.CO;2) doi: 10.1175/1520-0469(1976)033<1995:TSOIPF>2.0.CO;2
- 964 Harrington, J. Y., Moyle, A., Hanson, L. E., & Morrison, H. (2019). On
965 calculating deposition coefficients and aspect-ratio evolution in approx-
966 imate models of ice crystal vapor growth. *J. Atmos. Sci.*, *76*(6), 1609-
967 1625. Retrieved from <https://doi.org/10.1175/JAS-D-18-0319.1> doi:
968 10.1175/JAS-D-18-0319.1
- 969 Hashino, T., & Tripoli, G. J. (2007). The spectral ice habit prediction sys-
970 tem (ships). part i: Model description and simulation of the vapor de-
971 position process. *J. Atmos. Sci.*, *64*(7), 2210 - 2237. Retrieved from
972 <https://journals.ametsoc.org/view/journals/atsc/64/7/jas3963.1.xml>
973 doi: 10.1175/JAS3963.1
- 974 Heymsfield, A. (1972). Ice crystal terminal velocities. *J. Atmos. Sci.*, *29*,
975 1348-1357. Retrieved from [https://journals.ametsoc.org/view/
976 journals/atsc/29/7/1520-0469_1972_029_1348_ictv_2_0_co_2.xml](https://journals.ametsoc.org/view/journals/atsc/29/7/1520-0469_1972_029_1348_ictv_2_0_co_2.xml) doi:
977 10.1175/1520-0469(1972)029<1348:ICTV>2.0.CO;2
- 978 Heymsfield, A. J. (1978). The characteristics of graupel particles in north-
979 eastern colorado cumulus congestus clouds. *J. Atmos. Sci.*, *35*(2), 284-
980 295. Retrieved from [https://journals.ametsoc.org/doi/abs/10.1175/
981 1520-0469%281978%29035%3C0284%3ATCOGPI%3E2.0.CO%3B2](https://journals.ametsoc.org/doi/abs/10.1175/1520-0469%281978%29035%3C0284%3ATCOGPI%3E2.0.CO%3B2) doi: 10.1175/
982 1520-0469(1978)035<0284:TCOGPI>2.0.CO;2
- 983 Heymsfield, A. J., & Westbrook, C. D. (2010, 08). Advances in the Estimation of
984 Ice Particle Fall Speeds Using Laboratory and Field Measurements. *J. At-
985 mos. Sci.*, *67*(8), 2469-2482. Retrieved from [https://doi.org/10.1175/
986 2010JAS3379.1](https://doi.org/10.1175/2010JAS3379.1) doi: 10.1175/2010JAS3379.1
- 987 Jayaweera, K. O. L. F., & Cottis, R. E. (1969). Fall velocities of plate-like and
988 columnar ice crystals. *Q. J. Roy. Meteor. Soc.*, *95*(406), 703-709. Re-
989 trieved from [https://rmets.onlinelibrary.wiley.com/doi/abs/10.1002/
990 qj.49709540604](https://rmets.onlinelibrary.wiley.com/doi/abs/10.1002/qj.49709540604) doi: 10.1002/qj.49709540604
- 991 Jensen, A. A., & Harrington, J. Y. (2015). Modeling ice crystal aspect ratio evo-
992 lution during riming: A single-particle growth model. *J. Atmos. Sci.*, *72*(7),
993 2569-2590. Retrieved from <https://doi.org/10.1175/JAS-D-14-0297.1> doi:
994 10.1175/JAS-D-14-0297.1
- 995 Jensen, A. A., Harrington, J. Y., Morrison, H., & Milbrandt, J. A. (2017, 6). Pre-
996 dicting ice shape evolution in a bulk microphysics model. *J. Atmos. Sci.*, *74*,
997 2081-2104. Retrieved from [https://journals.ametsoc.org/view/journals/
998 atsc/74/6/jas-d-16-0350.1.xml](https://journals.ametsoc.org/view/journals/atsc/74/6/jas-d-16-0350.1.xml) doi: 10.1175/JAS-D-16-0350.1
- 999 Ji, W., & Wang, P. K. (1999). Ventilation coefficients for falling ice crystals in the
1000 atmosphere at low-intermediate reynolds numbers. *J. Atmos. Sci.*, *56*, 829-836.
1001 doi: 10.1175/1520-0469(1999)056<0829:VCFVIC>2.0.CO;2
- 1002 Karrer, M., Seifert, A., Ori, D., & Kneifel, S. (2021). Improving the representa-
1003 tion of aggregation in a two-moment microphysical scheme with statistics of
1004 multi-frequency doppler radar observations. *Atmos. Chem. Phys.*, *21*(22),
1005 17133-17166. Retrieved from [https://acp.copernicus.org/articles/21/
1006 17133/2021/](https://acp.copernicus.org/articles/21/17133/2021/) doi: 10.5194/acp-21-17133-2021
- 1007 Ke, C., Shu, S., Zhang, H., Yuan, H., & Yang, D. (2018, 2). On the drag coefficient
1008 and averaged nusselt number of an ellipsoidal particle in a fluid. *Powder Tech-
1009 nol.*, *325*, 134-144. doi: 10.1016/J.POWTEC.2017.10.049
- 1010 Kikuchi, K., Kameda, T., Higuchi, K., & Yamashita, A. (2013). A global classifica-
1011 tion of snow crystals, ice crystals, and solid precipitation based on observations
1012 from middle latitudes to polar regions. *Atmos. Res.*, *132-133*, 460-472. Re-

- 1013 trieved from [https://www.sciencedirect.com/science/article/pii/](https://www.sciencedirect.com/science/article/pii/S0169809513001841)
1014 S0169809513001841 doi: 10.1016/j.atmosres.2013.06.006
- 1015 Kintea, D. M., Roisman, I. V., Hauk, T., & Tropea, C. (2015, 9). Shape evolution of
1016 a melting nonspherical particle. *Physical Review E - Statistical, Nonlinear, and*
1017 *Soft Matter Physics*, 92. doi: 10.1103/PhysRevE.92.033012
- 1018 Kiwitt, T., Fröhlich, K., Meinke, M., & Schröder, W. (2022, 4). Nusselt correlation
1019 for ellipsoidal particles. *Int. J. Multiphas. Flow*, 149, 103941. doi: 10.1016/J
1020 .IJMULTIPHASEFLOW.2021.103941
- 1021 Kobayashi, T. (1961). The growth of snow crystals at low supersaturations. *Phi-*
1022 *los. Mag.*, 6(71), 1363-1370. Retrieved from [https://doi.org/10.1080/](https://doi.org/10.1080/14786436108241231)
1023 14786436108241231 doi: 10.1080/14786436108241231
- 1024 Korolev, A., & Isaac, G. (2003). Roundness and aspect ratio of particles in
1025 ice clouds. *J. Atmos. Sci.*, 60(15), 1795-1808. Retrieved from [https://](https://doi.org/10.1175/1520-0469(2003)060<1795:RAAROP>2.0.CO;2)
1026 doi.org/10.1175/1520-0469(2003)060<1795:RAAROP>2.0.CO;2 doi:
1027 10.1175/1520-0469(2003)060<1795:RAAROP>2.0.CO;2
- 1028 Lawson, R. P., Pilon, B., Baker, B., Mo, Q., Jensen, E., Pfister, L., & Bui, P.
1029 (2008). Aircraft measurements of microphysical properties of subvisible cir-
1030 rus in the tropical tropopause layer. *Atmos. Chem. Phys.*, 8(6), 1609–1620.
1031 Retrieved from <https://www.atmos-chem-phys.net/8/1609/2008/> doi:
1032 10.5194/acp-8-1609-2008
- 1033 Locatelli, J. D., & Hobbs, P. V. (1974). Fall speeds and masses of solid precipita-
1034 tion particles. *J. Geophys. Res.*, 79(15), 2185-2197. Retrieved from [https://](https://agupubs.onlinelibrary.wiley.com/doi/abs/10.1029/JC079i015p02185)
1035 agupubs.onlinelibrary.wiley.com/doi/abs/10.1029/JC079i015p02185
1036 doi: 10.1029/JC079i015p02185
- 1037 Martin, J. J., Wang, P. K., Pruppacher, H. R., & Pitter, R. L. (1981). Numerical
1038 study of the effect of electric charges on the efficiency with which planar ice
1039 crystals collect supercooled cloud drops. *J. Atmos. Sci.*, 38(11), 2462-2469.
1040 doi: 10.1175/1520-0469(1981)038<2462:ANSOTE>2.0.CO;2
- 1041 Matrosov, S. Y., Mace, G. G., Marchand, R., Shupe, M. D., Hallar, A. G., & Mc-
1042 cubbin, I. B. (2012, 8). Observations of ice crystal habits with a scan-
1043 ning polarimetric w-band radar at slant linear depolarization ratio mode.
1044 *J. Atmos. Ocean Tech.*, 29, 989-1008. Retrieved from [https://journals](https://journals.ametsoc.org/view/journals/atot/29/8/jtech-d-11-00131_1.xml)
1045 .ametsoc.org/view/journals/atot/29/8/jtech-d-11-00131_1.xml doi:
1046 10.1175/JTECH-D-11-00131.1
- 1047 McCorquodale, M. W., & Westbrook, C. D. (2021). Trail part 2: A comprehensive
1048 assessment of ice particle fall speed parametrisations. *Q. J. Roy. Meteor. Soc.*,
1049 147(734), 605-626. Retrieved from [https://rmets.onlinelibrary.wiley](https://rmets.onlinelibrary.wiley.com/doi/abs/10.1002/qj.3936)
1050 .com/doi/abs/10.1002/qj.3936 doi: 10.1002/qj.3936
- 1051 Melnikov, V., & Straka, J. M. (2013, 8). Axis ratios and flutter angles of cloud ice
1052 particles: Retrievals from radar data. *J. Atmos. Ocean Tech.*, 30, 1691-1703.
1053 Retrieved from [https://journals.ametsoc.org/view/journals/atot/30/8/](https://journals.ametsoc.org/view/journals/atot/30/8/jtech-d-12-00212_1.xml)
1054 jtech-d-12-00212_1.xml doi: 10.1175/JTECH-D-12-00212.1
- 1055 Milbrandt, J. A., Morrison, H., II, D. T. D., & Paukert, M. (2021). A triple-
1056 moment representation of ice in the predicted particle properties (p3) micro-
1057 physics scheme. *J. Atmos. Sci.*, 78(2), 439 - 458. Retrieved from [https://](https://journals.ametsoc.org/view/journals/atoc/78/2/jas-d-20-0084_1.xml)
1058 journals.ametsoc.org/view/journals/atoc/78/2/jas-d-20-0084_1.xml
1059 doi: 10.1175/JAS-D-20-0084.1
- 1060 Mitchell, D. L. (1988). Evolution of snow-size spectra in cyclonic storms. part i:
1061 Snow growth by vapor deposition and aggregation. *J. Atmos. Sci.*, 45, 3431-
1062 3451. doi: 10.1175/1520-0469(1988)045<3431:EOSSSI>2.0.CO;2
- 1063 Mitchell, D. L. (1996). Use of mass- and area-dimensional power laws for deter-
1064 mining precipitation particle terminal velocities. *J. Atmos. Sci.*, 53(12), 1710-
1065 1723. Retrieved from [https://doi.org/10.1175/1520-0469\(1996\)053<1710:](https://doi.org/10.1175/1520-0469(1996)053<1710:UOMAAD>2.0.CO;2)
1066 UOMAAD>2.0.CO;2 doi: 10.1175/1520-0469(1996)053<1710:UOMAAD>2.0.CO;
1067 2

- 1068 Mitra, S. K., Vohl, O., Ahr, M., & Pruppacher, H. R. (1990). A wind tun-
 1069 nel and theoretical study of the melting behavior of atmospheric ice par-
 1070 ticles. iv: Experiment and theory for snow flakes. *J. Atmos. Sci.*, *47*(5),
 1071 584 - 591. Retrieved from [https://journals.ametsoc.org/view/
 1072 journals/atsc/47/5/1520-0469_1990_047_0584_awtats_2_0_co_2.xml](https://journals.ametsoc.org/view/journals/atsc/47/5/1520-0469_1990_047_0584_awtats_2_0_co_2.xml) doi:
 1073 10.1175/1520-0469(1990)047<0584:AWTATS>2.0.CO;2
- 1074 Morrison, H., de Boer, G., Feingold, G., Harrington, J., Shupe, M. D., & Sulia, K.
 1075 (2012, 12). Resilience of persistent arctic mixed-phase clouds. *Nat. Geosci.*, *5*,
 1076 11-17. Retrieved from <https://www.nature.com/articles/ngeo1332> doi:
 1077 10.1038/ngeo1332
- 1078 Morrison, H., & Grabowski, W. W. (2008). A novel approach for represent-
 1079 ing ice microphysics in models: Description and tests using a kinematic
 1080 framework. *J. Atmos. Sci.*, *65*(5), 1528 - 1548. Retrieved from [https://
 1081 journals.ametsoc.org/view/journals/atsc/65/5/2007jas2491.1.xml](https://journals.ametsoc.org/view/journals/atsc/65/5/2007jas2491.1.xml)
 1082 doi: 10.1175/2007JAS2491.1
- 1083 Morrison, H., van Lier-Walqui, M., Fridlind, A. M., Grabowski, W. W., Harrington,
 1084 J. Y., Hoose, C., ... Xue, L. (2020). Confronting the challenge of model-
 1085 ing cloud and precipitation microphysics. *J. Adv. Model Earth Sy.*, *12*(8),
 1086 e2019MS001689. Retrieved from [https://agupubs.onlinelibrary.wiley
 1087 .com/doi/abs/10.1029/2019MS001689](https://agupubs.onlinelibrary.wiley.com/doi/abs/10.1029/2019MS001689) doi: 10.1029/2019MS001689
- 1088 Myagkov, A., Seifert, P., Bauer-Pfundstein, M., & Wandinger, U. (2016, 2). Cloud
 1089 radar with hybrid mode towards estimation of shape and orientation of ice
 1090 crystals. *Atmos. Meas. Tech.*, *9*, 469-489. doi: 10.5194/AMT-9-469-2016
- 1091 Myagkov, A., Seifert, P., Wandinger, U., Bühl, J., & Engelmann, R. (2016, 8). Re-
 1092 lationship between temperature and apparent shape of pristine ice crystals
 1093 derived from polarimetric cloud radar observations during the accept cam-
 1094 paign. *Atmos. Meas. Tech.*, *9*, 3739-3754. doi: 10.5194/AMT-9-3739-2016
- 1095 Naumann, A. K., & Seifert, A. (2015). A lagrangian drop model to study warm rain
 1096 microphysical processes in shallow cumulus. *J. Adv. Model Earth Sy.*, *7*(3),
 1097 1136-1154. Retrieved from [https://agupubs.onlinelibrary.wiley.com/
 1098 doi/abs/10.1002/2015MS000456](https://agupubs.onlinelibrary.wiley.com/doi/abs/10.1002/2015MS000456) doi: 10.1002/2015MS000456
- 1099 Nelson, J. (1998). Sublimation of ice crystals. *J. Atmos. Sci.*, *55*(5), 910-919.
 1100 Retrieved from [https://doi.org/10.1175/1520-0469\(1998\)055<0910:
 1101 SOIC>2.0.CO;2](https://doi.org/10.1175/1520-0469(1998)055<0910:SOIC>2.0.CO;2) doi: 10.1175/1520-0469(1998)055<0910:SOIC>2.0.CO;2
- 1102 Nelson, J. T., & Baker, M. B. (1996). New theoretical framework for studies
 1103 of vapor growth and sublimation of small ice crystals in the atmosphere.
 1104 *J. Geophys. Res.: Atmospheres*, *101*(D3), 7033-7047. Retrieved from
 1105 <https://agupubs.onlinelibrary.wiley.com/doi/abs/10.1029/95JD03162>
 1106 doi: 10.1029/95JD03162
- 1107 Nettesheim, J. J., & Wang, P. K. (2018, 9). A numerical study on the aerody-
 1108 namics of freely falling planar ice crystals. *J. Atmos. Sci.*, *75*, 2849-2865.
 1109 Retrieved from [https://journals.ametsoc.org/view/journals/atsc/75/9/
 1110 jas-d-18-0041.1.xml](https://journals.ametsoc.org/view/journals/atsc/75/9/jas-d-18-0041.1.xml) doi: 10.1175/JAS-D-18-0041.1
- 1111 Oseen, C. W. (1927). *Neuere methoden und ergebnisse in der hydrodynamik*. Akad.
 1112 Verlagsgesellschaft Leipzig. Retrieved from [https://archive.org/details/in
 1113 .ernet.dli.2015.80409](https://archive.org/details/in.ernet.dli.2015.80409)
- 1114 Pinsky, M., Khain, A., & Shapiro, M. (2001). Collision efficiency of drops in a wide
 1115 range of reynolds numbers: Effects of pressure on spectrum evolution. *J. At-
 1116 mos. Sci.*, *58*(7), 742 - 764. Retrieved from [https://journals.ametsoc.org/
 1117 view/journals/atsc/58/7/1520-0469_2001_058_0742_ceodia_2_0_co_2.xml](https://journals.ametsoc.org/view/journals/atsc/58/7/1520-0469_2001_058_0742_ceodia_2_0_co_2.xml)
 1118 doi: 10.1175/1520-0469(2001)058<0742:CEODIA>2.0.CO;2
- 1119 Pitter, R. L., Pruppacher, H. R., & Hamielec, A. E. (1974). A numerical
 1120 study of the effect of forced convection on mass transport from a thin
 1121 oblate spheroid of ice in air. *J. Atmos. Sci.*, *31*, 1058-1066. doi: 10.1175/
 1122 1520-0469(1974)031<1058:ANSOTE>2.0.CO;2

- 1123 Posselt, R., Simmel, M., & Wurzler, S. (2004). Comment on revision and clar-
 1124 ification of “a general hydrodynamic theory for mixed-phase microphysics”
 1125 [böhm, j.p., 1999, *atmos. res.* 52, 167–176]. *Atmos. Res.*, 69(3), 281 - 287.
 1126 Retrieved from [http://www.sciencedirect.com/science/article/pii/](http://www.sciencedirect.com/science/article/pii/S0169809503001248)
 1127 [S0169809503001248](http://www.sciencedirect.com/science/article/pii/S0169809503001248) doi: 10.1016/j.atmosres.2003.03.001
- 1128 Pruppacher, H., & Klett, J. (1997). *Microphysics of clouds and precipitation*.
 1129 Springer Netherlands. doi: 10.1007/978-0-306-48100-0
- 1130 Reinking, R. F. (1979). The onset and early growth of snow crystals by accretion
 1131 of droplets. *J. Atmos. Sci.*, 36, 870 - 881. Retrieved from [https://journals](https://journals.ametsoc.org/view/journals/atms/36/5/1520-0469_1979_036_0870_toaego_2_0_co_2.xml)
 1132 [.ametsoc.org/view/journals/atms/36/5/1520-0469_1979_036_0870_toaego](https://journals.ametsoc.org/view/journals/atms/36/5/1520-0469_1979_036_0870_toaego_2_0_co_2.xml)
 1133 [_2_0_co_2.xml](https://journals.ametsoc.org/view/journals/atms/36/5/1520-0469_1979_036_0870_toaego_2_0_co_2.xml) doi: 10.1175/1520-0469(1979)036<0870:TOAEGO>2.0.CO;2
- 1134 Schlamp, R., Pruppacher, H., & Hamielec, A. (1975). A numerical investi-
 1135 gation of the efficiency with which simple columnar ice crystals collide
 1136 with supercooled water drops. *J. Atmos. Sci.*, 32(12), 2330-2337. doi:
 1137 10.1175/1520-0469(1975)032<2330:ANIOTE>2.0.CO;2
- 1138 Sei, T., & Gonda, T. (1989). The growth mechanism and the habit change of ice
 1139 crystals growing from the vapor phase. *J. Cryst. Growth*, 94(3), 697-707.
 1140 Retrieved from [https://www.sciencedirect.com/science/article/pii/](https://www.sciencedirect.com/science/article/pii/0022024889900948)
 1141 [0022024889900948](https://www.sciencedirect.com/science/article/pii/0022024889900948) doi: 10.1016/0022-0248(89)90094-8
- 1142 Seifert, A., Leinonen, J., Siewert, C., & Kneifel, S. (2019). The geometry of rimed
 1143 aggregate snowflakes: A modeling study. *J. Adv. Model Earth Sy.*, 11(3), 712-
 1144 731. Retrieved from [https://agupubs.onlinelibrary.wiley.com/doi/abs/](https://agupubs.onlinelibrary.wiley.com/doi/abs/10.1029/2018MS001519)
 1145 [10.1029/2018MS001519](https://agupubs.onlinelibrary.wiley.com/doi/abs/10.1029/2018MS001519) doi: 10.1029/2018MS001519
- 1146 Sheridan, L. M. (2008). *Deposition coefficient, habit, and ventilation influences on*
 1147 *cirriform cloud properties* (Master’s thesis, Dept.of Meteorology, The Pennsyl-
 1148 vanian State University). Retrieved from [https://etda.libraries.psu.edu/](https://etda.libraries.psu.edu/catalog/8556)
 1149 [catalog/8556](https://etda.libraries.psu.edu/catalog/8556)
- 1150 Sheridan, L. M., Harrington, J. Y., Lamb, D., & Sulia, K. (2009). Influence of
 1151 ice crystal aspect ratio on the evolution of ice size spectra during vapor
 1152 depositional growth. *J. Atmos. Sci.*, 66(12), 3732-3743. Retrieved from
 1153 <https://doi.org/10.1175/2009JAS3113.1> doi: 10.1175/2009JAS3113.1
- 1154 Shima, S., Kusano, K., Kawano, A., Sugiyama, T., & Kawahara, S. (2009, 7). The
 1155 super-droplet method for the numerical simulation of clouds and precipitation:
 1156 a particle-based and probabilistic microphysics model coupled with a non-
 1157 hydrostatic model. *Q. J. Roy. Meteor. Soc.*, 135, 1307-1320. Retrieved from
 1158 <http://doi.wiley.com/10.1002/qj.441> doi: 10.1002/qj.441
- 1159 Shima, S., Sato, Y., Hashimoto, A., & Misumi, R. (2020). Predicting the mor-
 1160 phology of ice particles in deep convection using the super-droplet method:
 1161 development and evaluation of scale-sdm 0.2.5-2.2.0, -2.2.1, and -2.2.2. *Geosci.*
 1162 *Model Dev.*, 13(9), 4107–4157. Retrieved from [https://gmd.copernicus.org/](https://gmd.copernicus.org/articles/13/4107/2020/)
 1163 [articles/13/4107/2020/](https://gmd.copernicus.org/articles/13/4107/2020/) doi: 10.5194/gmd-13-4107-2020
- 1164 Sulia, K. J., & Harrington, J. Y. (2011, 11). Ice aspect ratio influences on
 1165 mixed-phase clouds: Impacts on phase partitioning in parcel models. *J.*
 1166 *Geophys. Res.: Atmospheres*, 116, 21309. Retrieved from [https://](https://onlinelibrary.wiley.com/doi/full/10.1029/2011JD016298)
 1167 onlinelibrary.wiley.com/doi/full/10.1029/2011JD016298[https://](https://onlinelibrary.wiley.com/doi/abs/10.1029/2011JD016298)
 1168 onlinelibrary.wiley.com/doi/abs/10.1029/2011JD016298[https://](https://agupubs.onlinelibrary.wiley.com/doi/10.1029/2011JD016298)
 1169 agupubs.onlinelibrary.wiley.com/doi/10.1029/2011JD016298 doi:
 1170 10.1029/2011JD016298
- 1171 Sutherland, W. (1893). Lii. the viscosity of gases and molecular force. *The*
 1172 *London, Edinburgh, and Dublin Philosophical Magazine and Journal of*
 1173 *Science*, 36(223), 507-531. Retrieved from [https://doi.org/10.1080/](https://doi.org/10.1080/14786449308620508)
 1174 [14786449308620508](https://doi.org/10.1080/14786449308620508) doi: 10.1080/14786449308620508
- 1175 Takahashi, T., Endoh, T., Wakahama, G., & Fukuta, N. (1991). Vapor diffusional
 1176 growth of free-falling snow crystals between -3 and -23°C. *J. Meteorol. Soc.*
 1177 *Jpn. Ser. II*, 69(1), 15-30. doi: 10.2151/jmsj1965.69.1_15

- 1178 Takahashi, T., & Fukuta, N. (1988). Supercooled cloud tunnel studies on the growth
 1179 of snow crystals between -4 and -20°C. *J. Meteorol. Soc. Jpn. Ser. II*, *66*, 841-
 1180 855. Retrieved from [https://www.jstage.jst.go.jp/article/jmsj1965/66/](https://www.jstage.jst.go.jp/article/jmsj1965/66/6/66_6.841/_article)
 1181 [6/66_6.841/_article](https://www.jstage.jst.go.jp/article/jmsj1965/66/6/66_6.841/_article) doi: 10.2151/jmsj1965.66.6.841
- 1182 Tridon, F., Battaglia, A., Chase, R. J., Turk, F. J., Leinonen, J., Kneifel, S., ...
 1183 Nesbitt, S. W. (2019). The microphysics of stratiform precipitation dur-
 1184 ing olympex: Compatibility between triple-frequency radar and airborne
 1185 in situ observations. *J. Geophys. Res.: Atmospheres*, *124*(15), 8764-8792.
 1186 Retrieved from [https://agupubs.onlinelibrary.wiley.com/doi/abs/](https://agupubs.onlinelibrary.wiley.com/doi/abs/10.1029/2018JD029858)
 1187 [10.1029/2018JD029858](https://agupubs.onlinelibrary.wiley.com/doi/abs/10.1029/2018JD029858) doi: 10.1029/2018JD029858
- 1188 Trömel, S., Simmer, C., Blahak, U., Blanke, A., Doktorowski, S., Ewald, F., ...
 1189 Quaas, J. (2021). Overview: Fusion of radar polarimetry and numerical
 1190 atmospheric modelling towards an improved understanding of cloud and
 1191 precipitation processes. *Atmos. Chem. Phys.*, *21*(23), 17291-17314. Re-
 1192 trieved from <https://acp.copernicus.org/articles/21/17291/2021/> doi:
 1193 [10.5194/acp-21-17291-2021](https://acp.copernicus.org/articles/21/17291/2021/)
- 1194 Um, J., McFarquhar, G. M., Hong, Y. P., Lee, S.-S., Jung, C. H., Lawson, R. P., &
 1195 Mo, Q. (2015). Dimensions and aspect ratios of natural ice crystals. *Atmos.*
 1196 *Chem. Phys.*, *15*(7), 3933-3956. Retrieved from [https://acp.copernicus](https://acp.copernicus.org/articles/15/3933/2015/)
 1197 [.org/articles/15/3933/2015/](https://acp.copernicus.org/articles/15/3933/2015/) doi: 10.5194/acp-15-3933-2015
- 1198 von Terzi, L., Neto, J. D., Ori, D., Myagkov, A., & Kneifel, S. (2022, 9). Ice micro-
 1199 physical processes in the dendritic growth layer: a statistical analysis combin-
 1200 ing multi-frequency and polarimetric doppler cloud radar observations. *Atmos.*
 1201 *Chem. Phys.*, *22*, 11795-11821. doi: 10.5194/ACP-22-11795-2022
- 1202 Wang, P. K. (2021). *Motions of ice hydrometeors in the atmosphere*. Springer Sin-
 1203 gapore. Retrieved from [https://link.springer.com/10.1007/978-981-33-](https://link.springer.com/10.1007/978-981-33-4431-0)
 1204 [-4431-0](https://link.springer.com/10.1007/978-981-33-4431-0) doi: 10.1007/978-981-33-4431-0
- 1205 Wang, P. K., & Ji, W. (2000, 04). Collision Efficiencies of Ice Crystals at
 1206 Low-Intermediate Reynolds Numbers Colliding with Supercooled Cloud
 1207 Droplets: A Numerical Study. *J. Atmos. Sci.*, *57*(8), 1001-1009. Re-
 1208 trieved from [https://doi.org/10.1175/1520-0469\(2000\)057<1001:](https://doi.org/10.1175/1520-0469(2000)057<1001:CEOICA>2.0.CO;2)
 1209 [CEOICA>2.0.CO;2](https://doi.org/10.1175/1520-0469(2000)057<1001:CEOICA>2.0.CO;2) doi: 10.1175/1520-0469(2000)057<1001:CEOICA>2.0.CO;2
- 1210 Westbrook, C. D., Hogan, R. J., Illingworth, A. J., Westbrook, C. D., Hogan,
 1211 R. J., & Illingworth, A. J. (2008, 1). The capacitance of pristine ice crys-
 1212 tals and aggregate snowflakes. *J. Atmos. Sci.*, *65*, 206-219. Retrieved from
 1213 <http://journals.ametsoc.org/doi/abs/10.1175/2007JAS2315.1> doi:
 1214 [10.1175/2007JAS2315.1](http://journals.ametsoc.org/doi/abs/10.1175/2007JAS2315.1)
- 1215 Westbrook, C. D., & Sephton, E. K. (2017). Using 3-d-printed analogues to inves-
 1216 tigate the fall speeds and orientations of complex ice particles. *Geophys. Res.*
 1217 *Lett.*, *44*(15), 7994-8001. Retrieved from [https://agupubs.onlinelibrary](https://agupubs.onlinelibrary.wiley.com/doi/abs/10.1002/2017GL074130)
 1218 [.wiley.com/doi/abs/10.1002/2017GL074130](https://agupubs.onlinelibrary.wiley.com/doi/abs/10.1002/2017GL074130) doi: 10.1002/2017GL074130
- 1219 Whitaker, S. (1972, 3). Forced convection heat transfer correlations for flow in pipes,
 1220 past flat plates, single cylinders, single spheres, and for flow in packed beds
 1221 and tube bundles. *AIChE Journal*, *18*, 361-371. Retrieved from [https://](https://onlinelibrary.wiley.com/doi/full/10.1002/aic.690180219)
 1222 onlinelibrary.wiley.com/doi/full/10.1002/aic.690180219[https://](https://onlinelibrary.wiley.com/doi/abs/10.1002/aic.690180219)
 1223 onlinelibrary.wiley.com/doi/abs/10.1002/aic.690180219[https://](https://aiche.onlinelibrary.wiley.com/doi/10.1002/aic.690180219)
 1224 aiche.onlinelibrary.wiley.com/doi/10.1002/aic.690180219 doi:
 1225 [10.1002/AIC.690180219](https://aiche.onlinelibrary.wiley.com/doi/10.1002/aic.690180219)
- 1226 Woo, S. E., & Hamielec, A. E. (1971). A numerical method of determining the
 1227 rate of evaporation of small water drops falling at terminal velocity in air. *J.*
 1228 *Atmos. Sci.*, *28*, 1448-1454. doi: 10.1175/1520-0469(1971)028<1448:ANMODT>
 1229 [2.0.CO;2](https://doi.org/10.1175/1520-0469(1971)028<1448:ANMODT>2.0.CO;2)
- 1230 Zängl, G., Reinert, D., Rípodas, P., & Baldauf, M. (2015). The icon (icosahed-
 1231 ral non-hydrostatic) modelling framework of dwd and mpi-m: Descrip-
 1232 tion of the non-hydrostatic dynamical core. *Q. J. Roy. Meteor. Soc.* doi:

1 **Explicit habit-prediction in the Lagrangian**
2 **super-particle ice microphysics model McSnow**

3 **Jan-Niklas Welss^{1,2}, C. Siewert¹, A. Seifert¹**

4 ¹Deutscher Wetterdienst, Frankfurt, Germany

5 ²Institute for Atmospheric Physics, Johannes Gutenberg University Mainz, Mainz, Germany

6 **Key Points:**

- 7 • McSnow is extended by an explicit habit prediction including the revision of cor-
8 responding parameterizations.
9 • A new inherent growth ratio overcoming existing deficiencies is proposed.
10 • The impact of the modifications on the depositional growth, aggregation, and rim-
11 ing is shown for two distinct case studies.

Corresponding author: Jan-Niklas Welss, jwelss@uni-mainz.de

Abstract

The Monte-Carlo ice microphysics model McSnow is extended by an explicit habit prediction scheme, combined with the hydrodynamic theory of Böhm. Böhm’s original cylindrical shape assumption for prolates is compared against recent lab results, showing that interpolation between cylinder and prolate yields the best agreement. For constant temperature and supersaturation, the predicted mass, size, and density agree well with the laboratory results, and a comparison with real clouds using the polarizability ratio shows regimes capable of improvement. An updated form of the inherent growth function to describe the primary habit growth tendencies is proposed and combined with a habit-dependent ventilation coefficient. The modifications contrast the results from general mass size relations and significantly impact the main ice microphysical processes. Depending on the thermodynamic regime, ice habits significantly alter depositional growth and affect aggregation and riming.

Plain Language Summary

The McSnow model was extended to predict the shape of ice crystals. A comparison of the falling behavior of modeled and 3D-printed ice crystals shows a discrepancy that can be improved by interpolation. At constant temperature and supersaturation, simulated crystal properties agree well with laboratory results, and by comparison to real clouds, we have updated the function to describe growth tendencies. Ice shape is shown to have a significant influence on the main microphysical processes.

1 Introduction

Inside clouds, atmospheric conditions are highly variable, often containing gaseous, liquid, and frozen water simultaneously in spatial and temporal heterogeneity (e.g. Morrison et al., 2012). The complex transitions involving all three phases are challenging when trying to describe and understand the microphysical processes within mixed-phase clouds (Morrison et al., 2020). Interactions involving ice crystals are tricky because of the variety of possible shapes. These habit characteristics are critical for the cold phase microphysical processes that influence sedimentation, deposition/sublimation, riming, aggregation, and especially radiative properties. Specialized observational methods to gather information on the rates of ice-microphysical processes are constantly being developed and improved, ranging from ground and in-situ (e.g. Field et al., 2004; Locatelli & Hobbs, 1974) to remote sensing observations (e.g. Dias Neto et al., 2019; Tridon et al., 2019). Classification and categorization of observed ice particles is an ongoing task (Bailey & Hallett, 2009; Kikuchi et al., 2013). This helps to link the occurrence of ice crystal types to specific atmospheric conditions. While these efforts provide data sets covering a variety of variables, they only partially allow attribution of effects to individual processes. Laboratory measurements such as Takahashi et al. (1991) or Connolly et al. (2012) allow process isolation, but lack representation of the full range of atmospheric conditions and especially the transition from isolation to a fully interactive system. As a result, the resulting physical descriptions can become highly specialized and are often only generalizable by assuming certain atmospheric conditions or categorizing ice habit, introducing artificial thresholds. The challenge posed by individual growth histories under changing conditions is to describe the variety of simple (columns, plates) and more complex (branched and polycrystalline) ice habits coexisting with aggregates composed of crystals of different shapes and numbers. Mass-size and mass-area relations may be able to describe the average geometry of certain ice habits (Mitchell, 1996; Auer & Veal, 1970; Um et al., 2015), but cannot represent the natural variety and transitions due to the use of thresholds. Overcoming the threshold between ice categories to allow a natural transition is a goal of modern microphysical schemes (Morrison & Grabowski, 2008; Milbrandt et al., 2021). Previous studies show that it is generally beneficial to explicitly resolve habit

62 development to improve the microphysical representation of ice in models: Jensen et al.
 63 (2017) show an effect of ice habit on the spatial precipitation pattern, Hashino and Tripoli
 64 (2007) find that dendrites extend dendritic growth regions further than atmospheric condi-
 65 tions suggest, and Sulia and Harrington (2011) conclude that the absence of ice habit
 66 underestimates ice growth and cloud glaciation time. Also, only models that resolve the
 67 evolving crystal shapes can make use of the wealth of data provided by radar polarime-
 68 try (Trömel et al., 2021) and combine the approaches to identify gaps in the interpre-
 69 tation of observations as well as in the microphysical descriptions when modeling clouds
 70 and precipitation (von Terzi et al., 2022).

71 To fully evaluate the effects of dynamically developing habits, detailed descriptions
 72 of processes at the particle level are needed. The approach of J.-P. Chen and Lamb (1994b)
 73 simplifies the ice habits of individual crystals as porous spheroids. The scheme predicts
 74 the shape and density of ice particles, helping to depict the natural evolution of ice habits
 75 and minimizing artificial type classification. While no natural crystal resembles a spheroid,
 76 Jayaweera and Cottis (1969) show that spheroids are suitable for representing colum-
 77 nar or plate-like ice crystals. However, even a simplified geometry requires changes in
 78 the process description: Vapor growth depends crucially on the particle shape, which af-
 79 fects the water vapor field around the particle. The theoretical framework of Böhm al-
 80 lows the consideration of ice habits for fall speed and collision effects based on spheroids
 81 (Böhm, 1989, 1992a, 1992b, 1992c, 1994, 1999). Based on investigations for oblates (Pitter
 82 et al., 1974), Hall and Pruppacher (1976) deduce that the ventilation is independent or
 83 only slightly dependent on the particle shape, but recent results suggest that this assump-
 84 tion underestimates the ventilation for prolate particles of larger sizes (Wang and Ji (2000),
 85 Ke et al. (2018) and others). For the collision of ice crystals with droplets, the results
 86 of Wang and Ji (2000) suggest the existence of preferred riming regions depending on
 87 the Reynolds number, which are difficult to represent in the spheroidal approach. Jensen
 88 and Harrington (2015) propose a way to distribute rime on the particle surface perpen-
 89 dicular to the flow in an effort to evaluate the effect of ice habits on the onset of rim-
 90 ing.

91 The likelihood of ice crystal aggregation is enhanced by non-spherical geometry mod-
 92 els because an increased cross-sectional area is a direct factor. However, it is difficult to
 93 describe the geometry of the resulting aggregates because of the many degrees of free-
 94 dom involved in the collision event. Several descriptions attempt to characterize the ge-
 95 ometry of aggregates after collisions (J.-P. Chen & Lamb, 1994a; Shima et al., 2020; Gavze
 96 & Khain, 2022) but a general and accurate parameterization is not yet available.

97 This paper presents the results of the extension of the Monte Carlo ice microphysics
 98 model *McSnow* Brdar and Seifert (2018) by an explicit habit prediction (HP) scheme
 99 using porous spheroids following J.-P. Chen and Lamb (1994b, CL94) and Jensen and
 100 Harrington (2015, JH15) to replace the classical m - D relations. The model uses the com-
 101 plete theoretical framework of Böhm, allowing the consideration of ice habits for fall ve-
 102 locity and collision effects (Sec. 2.2). We show that the original shape assumption for pro-
 103 lates underestimates the fall velocity derived from recent laboratory studies, and pro-
 104 vide an interpolation to overcome the observed mismatch (Sec. 3.1). The original formu-
 105 lation of the ventilation effect (Hall & Pruppacher, 1976) is extended to include a habit-
 106 specific ventilation effect suggested by several studies. We evaluate the performance of
 107 the habit prediction scheme against laboratory results and polarimetric observations, and
 108 propose several changes to overcome identified deficiencies. These include changes to the
 109 Inherent Growth Function (IGF) and the plate branching criterion. For the full model,
 110 we present the effects of explicit habit formation on deposition, riming, and aggregation
 111 in a 1-D snow shaft setup (Sec. 5).

112 2 Habit dependence of microphysical processes

113 This section describes the extensions of *McSnow* (Brdar & Seifert, 2018) regard-
 114 ing the habit prediction scheme, including necessary changes and clarifications encom-
 115 passed by an explicit ice morphology.

116 2.1 Habit prediction

In nature, the geometry and internal structure of ice particles can reach a high de-
 gree of complexity that defies any explicit description. A common approach is the use
 of z axis symmetric spheroids based on the two defining semi-axes a (equatorial) and c
 (polar radius). We can assume that the approximation of oblate and prolate spheroids
 for the two dominant primary habits of plates and columns is superior to fixed mass-size
 (m - D), mass-area (m - A), and size-density (D - ρ) relations because this removes the need
 for categorization of crystal and allows the transition between ice shapes to be consid-
 ered. The aspect ratio ϕ (ratio of polar to equatorial radius) describes the shape of the
 spheroid

$$\phi = \frac{c}{a}, \quad (1)$$

$$V_i = \frac{4}{3}\pi a^3 \phi = \frac{4}{3}\pi a^2 c, \quad (2)$$

$$\rho_{\text{app}} = \frac{m_i}{V_i}. \quad (3)$$

117 To account for possible secondary habit effects such as branching and hollowing, we use
 118 the ice volume V_i and the apparent density ρ_{app} . With the introduction of explicit par-
 119 ticle geometry, the shape changing processes must be adjusted, including vapor depo-
 120 sition, riming, and aggregation. Based on the results of J. Nelson (1998) and Harrington
 121 et al. (2019), we assume that the aspect ratio remains unchanged during sublimation.
 122 Mitra et al. (1990) and Kintea et al. (2015) find a similar behavior for melting, but the
 123 question remains whether water fills gaps revealed by branched or rimed structures, pos-
 124 sibly changing the density of the particles but not necessarily their shape.

125 2.1.1 Deposition/Sublimation

The equation for mass change through vapor deposition and sublimation,

$$\left(\frac{dm_i}{dt}\right)_v = 4\pi C D_v f_v \frac{p_{\text{vap}} - p_{\text{sat},i}}{R_v T} \left(1 + \frac{L_s^2 D_v p_{\text{sat},i}}{K_d R_v^2 T^3}\right)^{-1}, \quad (4)$$

126 considers the shape information mainly via the capacitance C . The other variables are
 127 the vapor diffusivity D_v , the ventilation coefficient f_v , the vapor pressure p_{vap} , the sat-
 128 uration pressure with respect to ice $p_{\text{sat},i}$, as well as the temperature T , the gas constant
 129 of water vapor R_v , the latent heat of sublimation L_s , and the thermal conductivity of
 130 dry air K_d . While J. T. Nelson and Baker (1996) show that the classical capacitance model
 131 cannot evolve faceted crystals because of inconsistent surface boundary conditions, it still
 132 produces relatively accurate estimates for mass and shape evolution. Still, Westbrook
 133 et al. (2008) show that the actual capacitance might depend on the internal structure
 134 of the hydrometeor, eventually causing an overestimation of capacitance for hydrome-
 135 teors of reduced density when using the original formulation of CL94.

Kobayashi (1961) shows that the evolution of primary habits (planar or columnar)
 depends mainly on ambient temperature, while that of secondary habits (branching and
 hollowing) depends on supersaturation. To quantify the temperature regimes favoring
 certain geometries, CL94 derive an inherent growth function Γ (IGF) by collecting labo-
 ratory and in-situ measurements for the temperature range between 0° and -30°C (re-
 spectively $243 - 273\text{K}$) by relating individual growth along the two major axes

$$\Gamma(T) = \frac{d \ln c}{d \ln a}. \quad (5)$$

The change in crystal mass causes an ice volume change

$$dV_i = \frac{1}{\rho_{\text{depo.}}} dm_i , \quad (6)$$

with the deposition density $\rho_{\text{depo.}}$. The spheroid shape does not explicitly allow for secondary habits. To capture branching and hollowing, the volume of the circumscribing spheroid is modified. Physically, the air inside the spheroid lowers the apparent density below ice density. J.-P. Chen and Lamb (1994b) use an empirical formulation for the deposition density based on experimental results of Fukuta (1969). We prefer the direct parameterization of the deposition density using the IGF proposed by Jensen and Harrington (2015, JH15)

$$\rho_{\text{depo}} = \begin{cases} \rho_i \Gamma(T) & , \quad \Gamma < 1 , \\ \rho_i \Gamma^{-1}(T) & , \quad \Gamma \geq 1 . \end{cases} \quad (7)$$

136 For oblates ($\phi < 1$), branching happens only if $v a > \pi D_v c$ (JH15), otherwise $\rho_{\text{depo}} =$
137 ρ_i . For prolates, hollowing happens immediately.

138 Using the same deposition density of branching/hollowing for sublimation may lead
139 to unphysical apparent densities because the IGF is only valid for temperature and su-
140 persaturation during the deposition process. Laboratory measurements suggest that ice
141 particles preserve their shape during sublimation, maintaining a constant aspect ratio
142 (Harrington et al., 2019; J. Nelson, 1998). We use the apparent density for particles un-
143 dergoing sublimation ($\rho_{\text{depo}} = \rho_{\text{app}}$).

Following CL94, we can predict the change in aspect ratio using the IGF

$$d \ln \phi = \frac{\Gamma - 1}{\Gamma + 2} d \ln V_i . \quad (8)$$

144 The evolution of V_i follows from Eqs. (4) and (6). As in previous work (Korolev & Isaac,
145 2003; Lawson et al., 2008; Baran, 2012), we restrict habit development for now to oc-
146 cur only for particles larger than $D \geq 10 \mu m$, since observations suggest that crystals
147 up to this size are approximately spherical.

The ice habit also affects the airflow around the particle and ventilation. The parts of the crystal surface that extend farthest into the flow experience the greatest effect due to increased water vapor advection (J.-P. Chen & Lamb, 1994b). Hall and Pruppacher (1976) suggest a description of the ventilation coefficient by

$$f_v = b_1 + b_2 X_{v,\text{equiv}}^\gamma , \quad (9)$$

the constants b_1 , b_2 , and γ have been generalized from observations for spheres and plates as

$$\begin{array}{llll} b_1 = 1.0, & b_2 = 0.14, & \gamma = 2 & \text{for } X_{v,\text{equiv}} \leq 1 , \\ b_1 = 0.86, & b_2 = 0.28, & \gamma = 1 & \text{for } X_{v,\text{equiv}} > 1 . \end{array}$$

The proposed ventilation is a function of Schmidt N_{Sc} and Reynolds number $N_{\text{Re,equiv}}$

$$X_{v,\text{equiv}} = N_{\text{Sc}}^{\frac{1}{3}} N_{\text{Re}}^{\frac{1}{2}} , \quad (10)$$

$$N_{\text{Sc}} = \frac{\mu_a}{\rho_a D_v} , \quad (11)$$

$$N_{\text{Re,equiv}} = \frac{d_{\text{equiv}} v_t \rho_a}{\mu_a} . \quad (12)$$

The dynamic viscosity μ_a can be described by Sutherland's Law (Sutherland, 1893)

$$\mu_a(T) = \mu_0 \frac{T_0 + T_S}{T + T_S} \left(\frac{T}{T_0} \right)^{3/2} , \quad (13)$$

148 with $\mu_0 = 1.716 \times 10^{-5}$, the melting/freezing point $T_0 = 273.15$ K, and the Suther-
 149 land temperature $T_S = 110.4$ K. The other variables are the air density ρ_a , the volume-
 150 equivalent diameter of a sphere d_{equiv} , and the terminal velocity v_t . Pruppacher and Klett
 151 (1997) collected habit-specific solutions for selected N_{Re} -regimes, but no continuous de-
 152 scription for all habits is known to the authors. We propose a habit-dependent formu-
 153 lation based on several numerical studies in Section 4.1.

Ventilation affects the geometric evolution by favoring the edges of the crystals. To account for this effect, we replace the IGF of Eq. 8 by the ventilation-influenced growth habit Γ^* as proposed by CL94

$$\Gamma^* = \Gamma f^* , \quad (14)$$

where the ratio of the local ventilation coefficients f^* of the respective axis (f_c, f_a)

$$f^* = \frac{f_c}{f_a} \approx \frac{b_1 + b_2 X^\gamma \left(\frac{c}{r_0}\right)^{1/2}}{b_1 + b_2 X^\gamma \left(\frac{a}{r_0}\right)^{1/2}} , \quad (15)$$

154 is used instead of the overall ventilation coefficient f_v . The local ventilation coefficient
 155 compares the local axis dimension to the radius of a sphere r_0 with the same volume.

The maximum dimension is defined as $D = 2 \max(a, c)$. We distinguish between the projected area A , which is relevant for riming and collision processes, and the hydrodynamic area \tilde{A} . The geometric area A of a spheroid is defined as the circumscribing ellipse

$$\begin{aligned} A_{\text{prolate}} &= \pi a c && \text{for prolates,} \\ A_{\text{oblate}} &= \pi a^2 && \text{for oblates,} \end{aligned} \quad (16)$$

while the cross-sectional area \tilde{A} is the effective area presented to the flow (cf. Böhm (1989)). JH15 suggest a linear dependency on ϕ and ρ_{app} to link the degree of branching to the thickness of a plate

$$\begin{aligned} \tilde{A} &= \xi A \\ \xi &= (1 - \phi) \left(\frac{\rho_{\text{app}}}{\rho_i} \right) + \phi && \text{for oblates,} \\ \xi &= 1 && \text{for prolates.} \end{aligned} \quad (17)$$

156 A decrease in cross-sectional area represents flow through the porous structures of the
 157 particle, which in turn reduces flow resistance. Prolates are assumed to be hollow inwards,
 158 so the cross-sectional area is effectively unaffected ($A = \tilde{A}$). In terms of collision prob-
 159 ability, we will see that the theory of Böhm uses boundary layer theory, explicitly con-
 160 sidering the difference between geometric and cross-sectional area via the area ratio q
 161 (cf. Eq. 23), which is similar to ξ above.

162 **2.1.2 Riming**

The distribution of rime along the two major axes is a critical factor in the prediction of ice crystal habit. We assume that particles fall with their largest cross-sectional area perpendicular to the flow, so that rime is always added to the minor axis while preserving the maximum dimension, transforming the habit of the particle towards a quasi-spherical shape. Jensen and Harrington (2015) refer to the work of A. J. Heymsfield (1978) for observations of the aspect ratio of graupel and propose that this quasi-spherical shape translates into an aspect ratio of $\phi = 0.8$ for plates or equivalently $\phi = 1/0.8 = 1.25$ for columns. For prolates with an aspect ratio between $1 < \phi \leq 1.25$, the updated equatorial radius a can be described as

$$a = \sqrt{\frac{V_{\text{tot}} + \frac{\Delta m_{\text{rime}}}{\rho_{\text{rime}}}}{\frac{4\pi}{3} c}} , \quad (18)$$

with V_{tot} the total volume before riming. Analogous, for oblate particles with $0.8 < \phi \leq 1$

$$c = \frac{V_{\text{tot}} + \frac{\Delta m_{\text{rime}}}{\rho_{\text{rime}}}}{\frac{4\pi}{3} a^2} . \quad (19)$$

The choice of a quasi-spherical aspect ratio threshold can lead to an oscillation around these values if simultaneous depositional growth supports the development of a more pronounced habit. These oscillations can be interpreted as a tumbling of the graupel particle, so that the newly added mass is randomly added to one of the axes.

We combine habit prediction with the stochastic riming approach of *McSnow*, introduced by Seifert et al. (2019), since it incorporates the shape properties of the particle into the collision probability using the theory of Böhm via the Stokes number (cf. Sec. 2.2.2). To better understand the feedback between habit information and collision probability, we will take a closer look at the implications of the shape dependence of the collision kernel.

2.1.3 Aggregation

For aggregates, we rely on the diagnostic geometry introduced by Brdar and Seifert (2018) following the empirical power laws for the mass-size-relation of aggregates (Mitchell, 1996, S3: Aggregates of Side Planes, Columns, and Bullets). The formulation and implementation of a more advanced aggregation framework that takes into account the habits and properties of the colliding particles in a self-consistent manner is left for future work (J.-P. Chen & Lamb, 1994a; Shima et al., 2020; Gavze & Khain, 2022). For small numbers of monomers ($N_m < 10$), we expect that this rather simple empirical approach may lead to errors in the estimation of particle properties (Karrer et al., 2021) compared to the explicit ideas above. The approach does not describe the transition from aggregates defined by the shape of a few individual monomer habits to those consisting of many particles.

To describe the aggregation of hydrometeors, we use the Monte-Carlo algorithm of Shima et al. (2009). When using an explicit habit prediction, aggregates and the assumption about the geometry term of the collision kernel K must be taken into account. In classical m - D - and m - A -relations, the maximum dimension D is used to estimate the geometry term (D -Kernel)

$$K_D = \pi \left(\frac{D_1}{2} + \frac{D_2}{2} \right)^2 S E_c |v_1 - v_2| = \pi (r_1 + r_2)^2 S E_c |v_1 - v_2| , \quad (20)$$

where S is the sticking efficiency, E_c is the collision efficiency (see Sec. 2.2.2), and v_n is the terminal fall velocity of the individual particles. The formulation is neutral for the treatment of oblates, but may overestimate the actual collision cross section of a prolate. An alternative is the A -Kernel (Böhm, 1994; Connolly et al., 2012; Karrer et al., 2021), which uses the equivalent radius $r_{n,\text{eq}} = \sqrt{A_n \pi^{-1}}$

$$K_A = \pi \left(\sqrt{A_1 \pi^{-1}} + \sqrt{A_2 \pi^{-1}} \right)^2 S E_c |v_1 - v_2| = \pi (r_{1,\text{eq}} + r_{2,\text{eq}})^2 S E_c |v_1 - v_2| . \quad (21)$$

The overestimation can be determined by the ratio of the maximum dimension of the prolates D_{max} to the equivalent diameter $D_{n,\text{eq}}$ and is proportional to

$$\frac{D_{\text{max}}}{D_{n,\text{eq}}} = \frac{2c}{2\sqrt{A_n \pi^{-1}}} = \frac{c}{\sqrt{a c}} = \sqrt{\frac{c}{a}} = \sqrt{\phi} . \quad (22)$$

We favor the use of the A -kernel when using the habit prediction scheme.

2.2 Review of Boehm's terminal velocity and collision efficiency parameterization

The work of Böhm comprises several publications, making it difficult to extract the parameterizations for terminal velocity and collision efficiency from his original work (Böhm,

190 1989, 1992a, 1992b, 1992c, 1994, 1999). Therefore, we review and summarize his work
 191 and its application to habit prediction. Since Böhm (2004) advised to use the original
 192 equations because they compare better with numerical simulations and field observations,
 193 we exclude the revision of Posselt et al. (2004).

194 **2.2.1 Terminal velocity**

195 The terminal velocity scheme is important for particles with different shapes and
 196 directly affects the depositional growth and the collision kernel. Böhm’s parameteriza-
 197 tion is a generalized and complete framework that makes the following necessary assump-
 198 tions

- 199 • The maximum dimension is oriented in the horizontal plane, as shown for exam-
 200 ple by Westbrook and Sephton (2017) for all simple geometries studied.
- The porosity p in the theory of Böhm is related to the ratio of the cross-sectional
 area \tilde{A} to the circumscribing ellipsis area A_{ce} . It represents the internal structure
 of ice crystals caused by secondary habits

$$p = 1 - q, \quad q = \frac{\tilde{A}}{A_{ce}}. \quad (23)$$

201 The ratio q is not to be confused with the area ratio $A_r = \tilde{A} A_{cc}^{-1}$ which A. J. Heyms-
 202 field and Westbrook (2010) and McCorquodale and Westbrook (2021) define as
 203 the ratio of the cross-sectional area to the circumscribing circle A_{cc} .

- Böhm (1992a) argues that the hydrodynamic behavior of prolate particles is sim-
 ilar to that of cylinders. He suggests

$$q = \frac{4}{\pi} \quad \text{for } \phi > 1.$$

204 This approximation is discussed in detail in Section 3.1.

- 205 • We add the assumption that all particles accelerate immediately to their termi-
 206 nal velocity. See, e.g., Naumann and Seifert (2015) for an alternative approach that
 207 attempts to account for deviations from the terminal fall velocity.

208 Böhm’s parameterization is valid for solid and liquid hydrometeors and is based on a func-
 209 tional dependence of the drag coefficient on the Reynolds number derived from Bound-
 210 ary Layer Theory (BLT). The terminal velocity follows the definition of the Reynolds
 211 number. Both the Reynolds number and the drag coefficient are modified by the aspect
 212 ratio via the Best number (see Eq. A1).

213 Böhm (1992a) showed that the formula is consistent with viscous theory, and by
 214 matching the results from BLT with Oseen’s theory (Oseen, 1927), there is good agree-
 215 ment of inertial drag at low Reynolds numbers. Böhm (1992a) claims that the errors are
 216 generally on the order of $\epsilon \leq 10\%$ for $0 < N_{Re} < 5 \times 10^5$ for the hydrometeor types
 217 studied (raindrops, columnar and planar ice crystals, rimed and unrimed aggregates, var-
 218 ious types of graupel, and hail). The complete parameterization of the fall velocity can
 219 be found in the appendix A1.

220 **2.2.2 Collision efficiency**

Generally, the collision efficiency E_c is defined as the ratio of the actual collision
 cross section to the geometric one (Pruppacher & Klett, 1997)

$$E_c = \frac{x_c^2}{(r_1 + r_2)^2} = \frac{y_s}{\delta}, \quad (24)$$

where x_c is the initial horizontal offset and r_n is the radius of the interacting particles.
 Böhm (1992b) states that the collision efficiency for axisymmetric particles can be de-
 scribed by the ratio of the stop distance of the collected particle y_s and the boundary

layer thickness of the collecting particle δ . For non-axisymmetric particles, the collision efficiency derivation is extended to a generalized form (Böhm, 1992c)

$$E_c = \left(\frac{y_s}{\delta} \right)^{2/j}, \quad (25)$$

with $j = 1$ for a two-dimensional flow (around the prolate) and $j = 2$ for the axisymmetric case. The boundary layer thickness δ can be calculated by

$$\delta = \delta_0 \frac{r}{\sqrt{N_{\text{Re}} \Gamma_\phi}}, \quad (26)$$

221 with $\delta_0 = 3.60$ for oblates and $\delta_0 = 4.54$ for prolates. The habit specific function Γ_ϕ
 222 can be found in the Appendix (Eq. A1c).

By replacing the individual boundary layer by the sum of the boundary layers of the colliding particles and integrating the differential equation from the initial velocity (detailed analysis in the dissertation (Böhm, 1990)), Böhm finds the collision efficiency for the resulting two-body system as

$$E_c = \begin{cases} [H \ln(\cosh \frac{F}{H} + \frac{1+G}{F} \sinh \frac{F}{H}) - G]^{2/j}, & (\frac{F}{H} < 10), \\ H \ln(\frac{F+G}{2F}) + F - G, & (\frac{F}{H} \geq 10). \end{cases} \quad (27)$$

223 The details of the variables used can be found in A2.

To account for the contribution of the surrounding non-frictional flow, Böhm added an approximate analytical solution based on potential flow theory (cf. Böhm (1994)). This extension aims at improving the asymptotic behavior for low Reynolds numbers $N_{\text{Re}} \lesssim 1$. With this modification, the total collision efficiency E is the product of the collision efficiency according to BLT E_c (from above) and the contribution from potential flow theory E_p

$$E = E_c E_p = \begin{cases} E_c \left[\left(\cosh \frac{\Delta_x t_\delta}{c_x} + \frac{1}{\Delta_x} \sinh \frac{\Delta_x t_\delta}{c_x} e^{-t_\delta/c_x} \right) \right]^{-j}, & (b c_y \geq 1), \\ E_c \left[\left(\frac{2 \Delta_x}{1+\Delta_x} e^{-(\Delta_x-1) t_\delta/c_x} \right) \right]^j, & (b c_y \leq 1). \end{cases} \quad (28)$$

224 The full formulations of the variables used in Eq. 28 can also be found in Appendix A2.
 225 For the remainder of the paper, we will refer to the total collision efficiency E as E_c .

226 3 Discussion of Boehm's Theory for habit prediction

227 3.1 Shape assumptions for columns

For particles that change habit, the hydrodynamic assumption in Böhm's theory changes from a symmetric flow around an oblate to an asymmetric flow around a cylinder (cf. dashed lines in Fig. 3). This change in morphology between primary habits may not be fully transferable to natural ice geometries, where complex crystalline features such as capped columns may evolve instead of complete habit changes. It is unclear if and how the spheroidal approach could capture these effects. Recent laboratory results from McCorquodale and Westbrook (2021) provide data for over 80 particle geometries at different aspect ratios. McCorquodale and Westbrook (2021) also evaluate the performance of Böhm's original work (Böhm, 1989, B89) and criticize a general overestimation of the drag coefficient. We expect the modifications from (Böhm, 1992a) to (Böhm, 1999) including the dependency on the shape of the spheroidal to significantly improve the agreement with the lab data. The C_d - N_{Re} relationship of the latest formulation from Böhm is compared with the TRAIL results in Figure 1 and the data points for the *CO1* particle ($\phi = 1.0476$) from Westbrook and Sephton (2017). We re-scale the drag coefficient by the area ratio $A_r^{1/2}$ compensates for the effect of A_r and allow comparison between the data and the derived C_d - N_{Re} -relation of A. J. Heymsfield and Westbrook

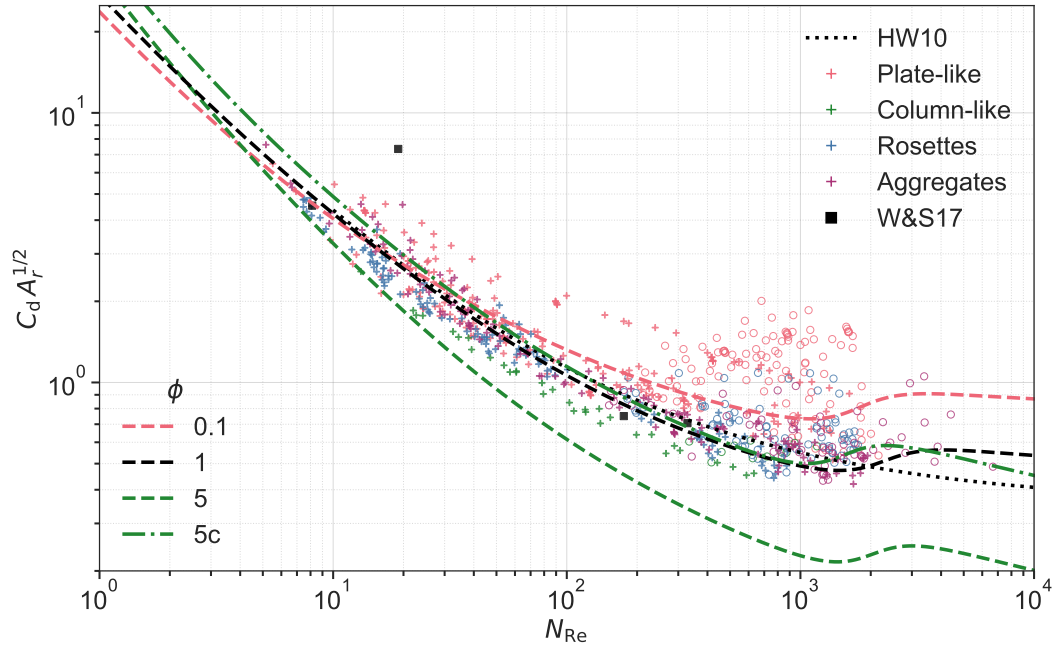


Figure 1. Comparison of measurements of N_{Re} and drag coefficient C_d for ice particle analogues (colored '+'/'o' for steady/unsteady regimes) against the parameterization of Böhm. Black squares mark the data from Westbrook and Sephton (2017, W&S17) for a cylinder with $\phi = 1.0476$. The black dotted line marks the results from A. J. Heymsfield and Westbrook (2010), while the dashed colored lines show the results using the parameterization from Böhm for the corresponding ϕ .

(2010). The dashed and dash-dotted lines show three different ARs (color-coded) representing spherical ($\phi = 1$, black), plate-like ($\phi = 0.1$, red), and columnar/prolate particles ($\phi = 5$, green). Additionally, we include colored markers for the TRAIL results. The area ratio needs special attention when the scheme of Böhm is used for prolate particles, because the definition varies from that of q (Eq. 23). McCorquodale and Westbrook (2021) define the area ratio A_r as

$$A_r = \tilde{A} A_{cc} = q \phi^{-1}, \quad (29)$$

with $q = 1$ for prolate spheroids and $q = 4\pi^{-1}$ for cylinders. For all other hydrometeor types we assume $A_r = 1$. The laboratory data and the parameterization agree well and the explicit dependence on the aspect ratio of the hydrometeors can capture the geometric effect of the different particle types. The drag coefficient of columnar particles differs significantly between the cylindrical and the prolate approach. At low Re , the prolate curve seems to reproduce the drag coefficient better. However, as Re increases, it greatly underestimates the drag and the cylindrical approach provides a better representation.

To better understand the difference in drag between cylindrical and spheroidal shapes, we compare the ϕ dependence of the parameterization with the laboratory results for prolate particles only. The combined data set consists of particles with $\phi = [1.0476, 2, 3, 5]$, allowing us to estimate the behavior near sphericity and the asymptotic behavior. Starting from low Reynolds numbers $N_{Re} \approx 10^0$, the two geometries slowly diverge as can be seen in Figure 2. For $N_{Re} > 10^2$, the prolate geometry agrees well with the two black squares marking the data of $\phi = 1.0476$, but has lower drag coefficients than the measurements for $\phi \geq 2$. The curves using the cylindrical assumption behave in the oppo-

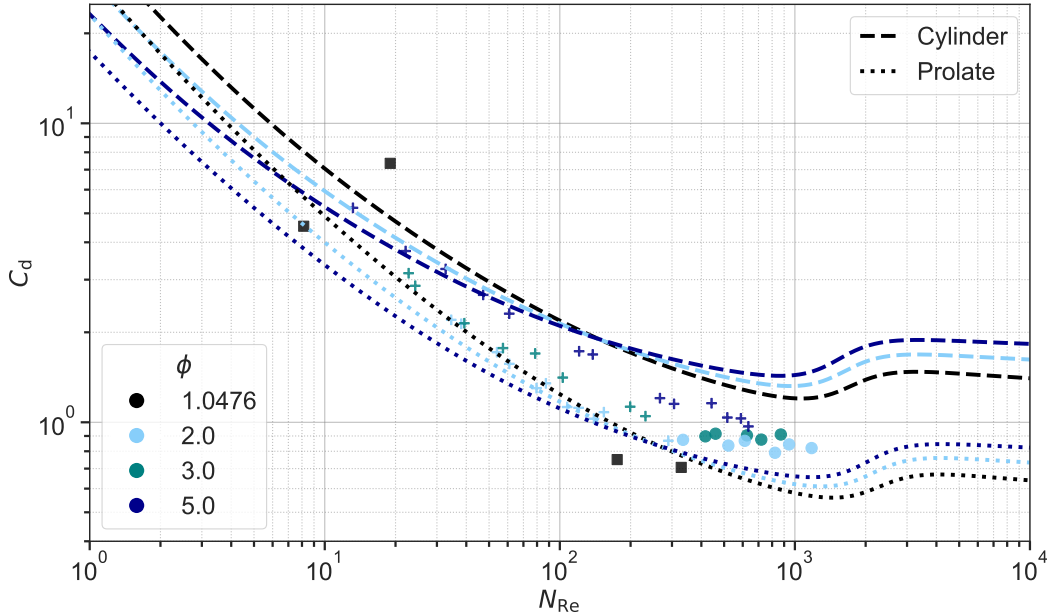


Figure 2. Comparison of N_{Re} and C_d for measured prolate ice particle analogues from McCorquodale and Westbrook (2021) ('+'/'o' for steady/unsteady regimes) and Westbrook and Sephton (2017) (squares) against the parameterization of Böhm for different ϕ (color-coded) and assumed hydrodynamic assumption (short-dashed: prolate, long-dashed: cylinder).

244 site way and predict to high drag coefficients for $\phi \geq 2$ and especially overestimate the
 245 behavior for $\phi = 1.0476$. The majority of the measurements lie between the two assump-
 246 tions. The disagreement for particles near sphericity explains the sudden deceleration
 247 of particles evolving from oblate or spherical particles into prolates when a cylinder is
 248 assumed and suggests a revision of this approach.

Using the original data from McCorquodale and Westbrook (2021), we derive a N_{Re} - C_d relation only for hexagonal columns (HCs) based on the area ratio A_r to describe the shape

$$C_d = A_r^n C_0 (1 + d_0 N_{Re}^{-1/2})^2 . \quad (30)$$

The empirical values found are $n = -1/2$, $C_0 = 0.30$, and $d_0 = 7.1$, improving the agreement for HCs over the models of A. J. Heymsfield and Westbrook (2010) and McCorquodale and Westbrook (2021), which are generalized for all particle types (cf. Fig. A1). We use the empirical values obtained for Eq. (30) to extrapolate the behavior to other aspect ratios and corresponding terminal velocities. Particle characteristics are derived by similarity theory for specific data points of hexagonal columns. Figure 3 shows the fall speed as a function of aspect ratio $v_t(\phi)$ for four particles of increasing mass. The black and dark blue line are representative for $Re < 100$ and the light blue and grey line for particles with $100 < Re < 1000$. Comparing the results from Böhm's scheme for the spheroidal (solid) and the cylindrical prolate assumption (dashed), shows the aforementioned deceleration near $\phi = 1$. The fall velocity behavior derived from the data of McCorquodale and Westbrook (2021) suggests a more subtle transition from a prolate to a cylindrical geometry and fits the results of Figure 2. The cylindrical geometry prescribes an edge at the basal surface, but physically the representation of this edge in the hydrodynamic properties is at least questionable in the spheroidal framework of habits. We therefore

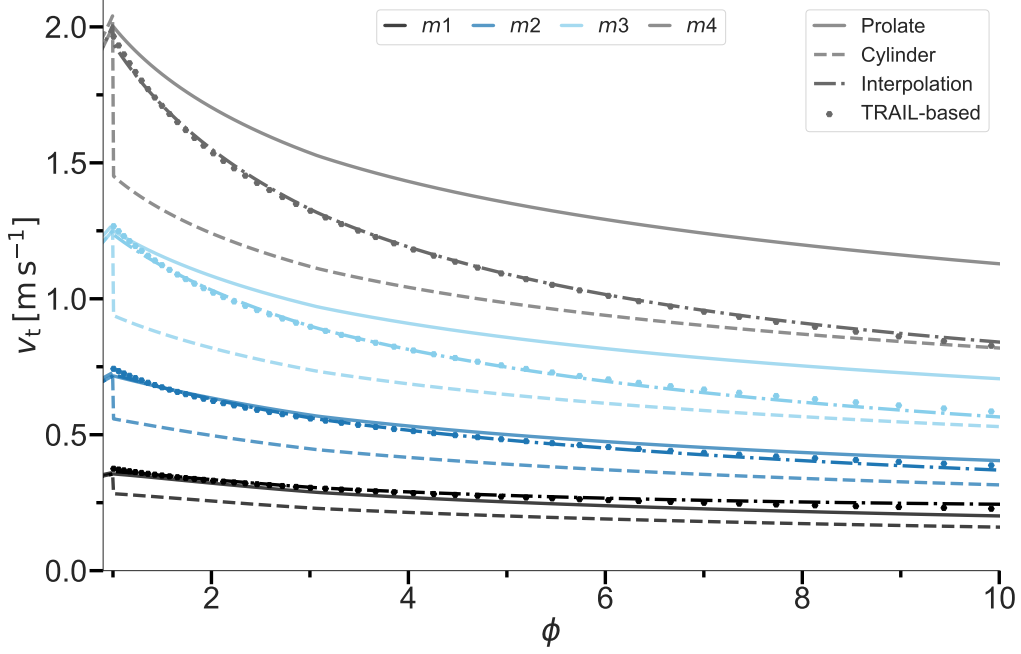


Figure 3. Terminal fall speed v_t dependency on the aspect ratio ϕ for particles with different mass (color-coded), treated as a prolate (solid) or a cylindrical spheroid (dashed), for TRAIL-based data (points), and for an interpolated approach (dash-dotted line, Eq. 31).

advocate an interpolation between the two fall velocities v_{pro} and v_{cyl} using the form

$$v(\phi) = f(\phi) v_{\text{pro}} + (1 - f(\phi)) v_{\text{cyl}}, \quad (31)$$

$$f(\phi) = \beta(m) e^{-\alpha(m)\phi} \quad (32)$$

This function helps to account for the relatively steep decrease in v_t with increasing ϕ , while matching the asymptotic behavior for the cylindrical approach. We propose a simple fit for the mass dependence of $\alpha(m)$ and $\beta(m)$

$$\begin{aligned} g(m) &= a \ln(m) + b, \\ a_\alpha &= 8.60 \times 10^{-2}, & b_\alpha &= 1.722, \\ a_\beta &= 3.08 \times 10^{-2}, & b_\beta &= 1.691. \end{aligned} \quad (33)$$

249 Figure 3 already includes the interpolated fall speed as dash-dotted lines that match the
 250 TRAIL results. The interpolation overcomes the need to choose between cylinder and
 251 prolate geometry, providing a smooth transition from prolate to cylinder-like behavior
 252 of ice columns.

253 3.2 Response to atmospheric conditions

The terminal fall velocity and the collision efficiency of Böhm are derived from using the Reynolds and Best numbers. This introduces a dependency on atmospheric conditions since both numbers depend on the air density ρ_a and the temperature via the dynamic viscosity $\mu(T)$ (Eqs. A1a & 13). Therefore, v_t and E_c must also change with height if a realistic atmospheric profile is assumed. Pinsky et al. (2001) find an increase in collision efficiency of more than a factor of two for a collision of small droplets ($D_1 \approx 30 - 50 \mu\text{m}$ and $D_2 \approx 10 - 20 \mu\text{m}$) between the 1000 and 500 hPa levels. The effect of the

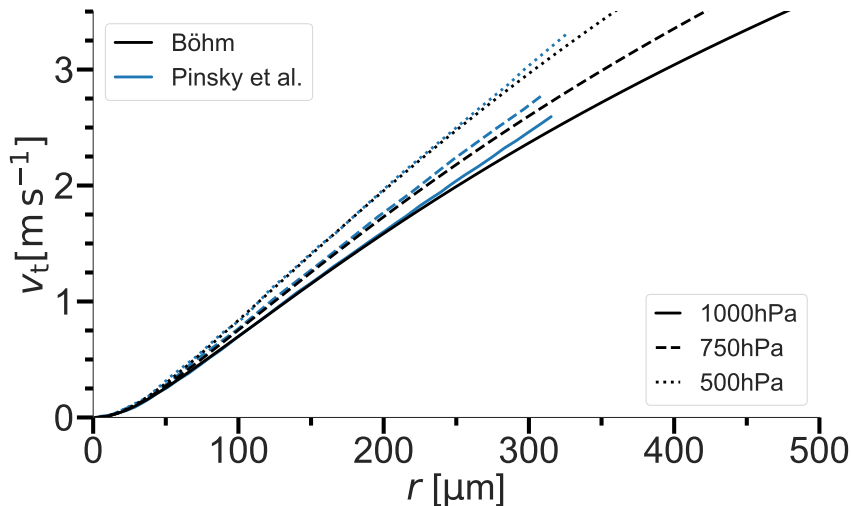


Figure 4. Dependency of v_t on the drop radius for the pressure levels 1000 hPa (solid), 750 hPa (long dashed), 500 hPa (short dashed) for Böhm’s scheme (black) and from Pinsky et al. (2001) (blue lines).

atmospheric conditions decreases with increasing droplet size. They argue that 90 % of the enhancement is due to the sensitivity of E_c to the relative velocity difference and only 10 % to an increase in swept volume. Böhm (1992b) finds an increase in E_c with temperature and pressure on the order of only 10 % for small drops ($r_1 \lesssim 30 \mu\text{m}$) and almost no effect for larger ones. Although we expect the work of Böhm to be generalizable, the contradiction of the two results requires an analysis of the dependence of Böhm’s fall velocity and collision efficiency parameterizations on different atmospheric states for droplets and ice particles. Compared to Pinsky et al. (2001), we change the surface temperature to freezing point to have a physically justified setup for ice particles at $p = 1000 \text{ hPa}$. While this change could affect the results, we argue that the exponential decrease in pressure with height dominates the effect over the linear dependence of temperature. Fig. 4 shows the comparison of terminal velocity by droplet size between the results of Pinsky et al. (2001) and with the scheme of Böhm. Böhm’s scheme predicts comparable results for all pressure levels. Both results show that the terminal velocity for a drop with $r = 300 \mu\text{m}$ is about 25 % greater at 500 hPa than at 1000 hPa. Using the adjustment factor of Beard (1980) allows us to compare the pressure dependence as a function of atmospheric conditions

$$f_{v_t} = \frac{v_t(T, p)}{v_{t,0}(T_0, p_0)}, \quad (34)$$

254 with the reference value of $v_{t,0}$ at $p_0 = 1000 \text{ hPa}$ and $T_0 = 273.15 \text{ K}$. We look at four
 255 different particle types (drop, oblate w. $\phi = 0.25$, prolate w. $\phi = 4$, and graupel w.
 256 $\phi = 1$ and $\rho_r = 800 \text{ kg m}^{-3}$) and five different masses equal to the mass of a sphere
 257 with an equivalent diameter of $D_{\text{eq}} = [20, 50, 100, 200, 500] \mu\text{m}$. In Figure 5 we see that
 258 the adjustment factor is proportional to D and can reach a maximum of about 1.3 at
 259 500 hPa for $D = 500 \mu\text{m}$. The difference between particle types is small, but becomes
 260 more relevant for larger particles.

261 In Figure 6 we analyze the effect of the changing thermodynamic state on the col-
 262 lision efficiency for four different collision pairs: drop-drop (D-D, solid lines), graupel-
 263 drop (G-D, dash-dotted lines), oblate-oblate (O-O, dashed lines), and prolate-prolate (P-
 264 P, dotted lines) collisions. The equivalent diameters of the particles involved are color-

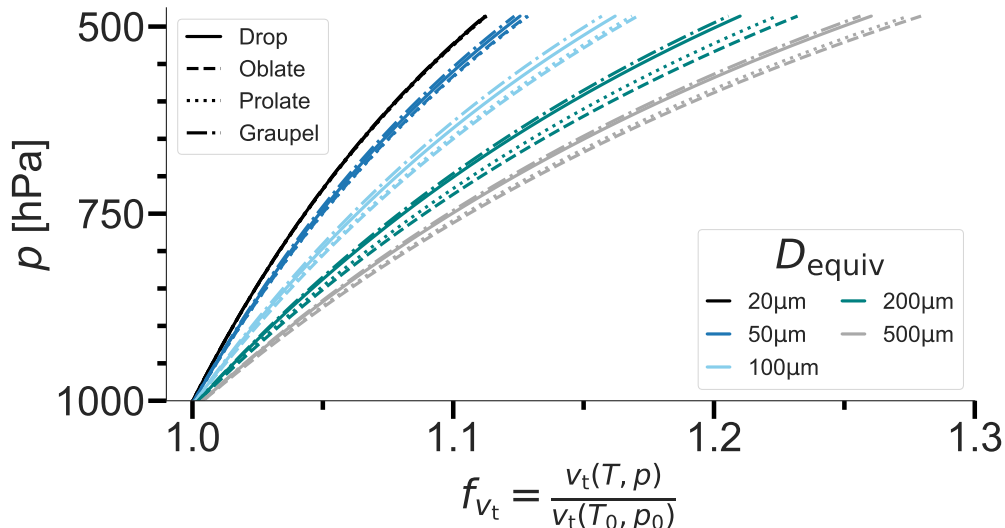


Figure 5. p -profiles of f_{v_t} for drops (solid), oblates (dashed), prolates (dotted), and graupel particles (dash-dotted lines). Color-coded is the equivalent diameter.

265 coded and include the size range used for the terminal velocity. The impact is inversely
 266 proportional to the mass/size and much smaller than for v_t , not exceeding 1.12. We can
 267 therefore specify the statement of Pinsky et al. (2001): for small particles, the change
 268 in collision efficiency itself dominates the collision behavior. The impact is higher for large
 269 particles ($\leq 30\%$), where the change in terminal velocity dominates the atmospheric depen-
 270 dence of the collision kernel. Looking at pairs with similar fall velocities, where the
 271 collision efficiency rapidly approaches zero, we observe adjustment factors greater than
 272 two, as observed by Pinsky et al. (2001) (not shown). The combined effect of atmospheric
 273 conditions on terminal velocity and collision efficiency is shown in Figure 7 via the ad-
 274 justment factor of the collision kernel K . The impact is strongest for the collision of small
 275 particles where the onset of effective collision causes strong difference in collision efficiency.
 276 For all collisions of larger particles, the total amplification does not exceed 2.5% and can
 277 be considered negligible.

278 3.3 Habit impact on riming efficiency

279 While Böhm compares and calibrates his theory for the collision efficiency with re-
 280 sults of Schlamp et al. (1975), Martin et al. (1981) and Reinking (1979), more recent re-
 281 sults of e.g. Wang and Ji (2000) are available. These are improved with respect to the
 282 shape of the particles investigated and the accuracy of the flow field, including unsteady
 283 features. Therefore, their results are suitable to evaluate the validity of Böhm (1992a)'s
 284 theory for collision events of spheroids with spherical droplets up to radii of $r = 100 \mu\text{m}$.
 285 In Figure 8, the analytical collision efficiencies of Böhm are plotted against the simula-
 286 tion of Wang and Ji (2000) for given geometries of oblates, cylinders, and broadly branched
 287 crystals. The cylindrical shape is the most difficult to compare due to the mismatch be-
 288 tween the actual and spheroidal shape, combined with the asymmetry of the flow.

289 The results for the oblates are in good agreement with respect to the onset, max-
 290 ima and cut-offs of all eight particles (Fig. 8a). The direct comparison for the cylinder
 291 (Fig. 8b) shows a slightly delayed onset and higher maxima for curves following the theo-
 292 ry of Böhm. The cut-offs are shifted to higher collected droplet radii compared to Wang
 293 and Ji (2000). Note that terminal velocity interpolation is applied. For branched crys-

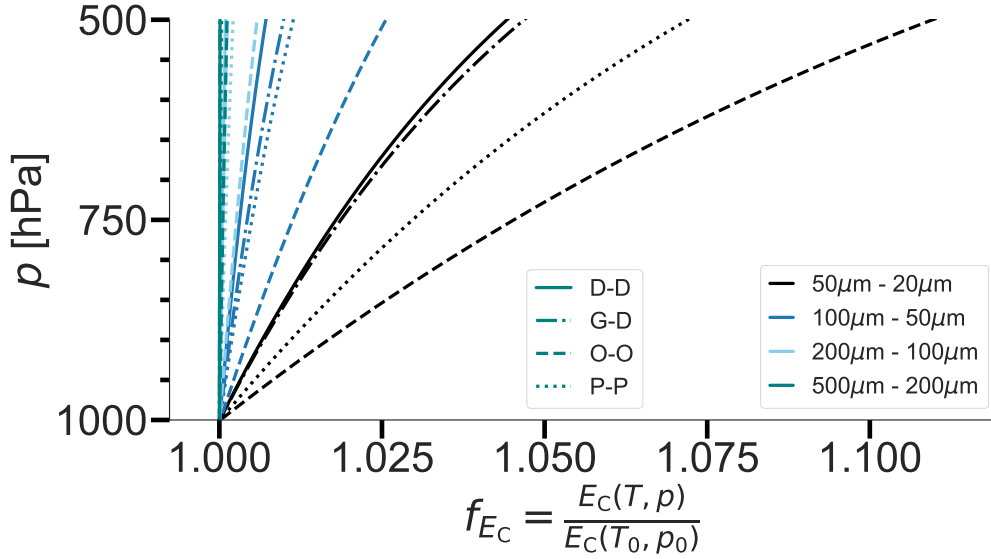


Figure 6. p -profiles of f_{Ec} for a drop-drop (D-D, solid), graupel-droplet (G-D, dash-dotted lines), an oblate-oblate (O-O, dashed), and a prolate-prolate collision (P-P, dotted). Color-coded is the equivalent diameter of the colliding particles.

294 tals (Fig. 8c) the onset and maximum are quite close. Only the cut-off radii differ, es-
 295 pecially for larger crystals. Nevertheless, the overall similarity of the results is satisfac-
 296 tory considering the theoretical assumptions. We conclude that the theory of Böhm pro-
 297 vides a suitable framework for parameterizing the collision efficiency of primary habits
 298 compared to numerical simulations.

299 4 Revision of Theory

300 4.1 Shape-dependent ventilation

301 Several studies present formulations for habit-specific ventilation coefficients based
 302 on the underlying geometry, which may differ substantially from Hall and Pruppacher
 303 (1976, HP76) (Prolate: Wang and Ji (2000, WJ00), Ke et al. (2018, Ke18), Kiwitt et al.
 304 (2022, K22), Y. Chen et al. (2021), Oblates: Pitter et al. (1974, P74), Ji and Wang (1999,
 305 J99), Wang (2021, W21), Nettesheim and Wang (2018, NW17), spheres: Woo and Hami-
 306 elec (1971, WH71), Whitaker (1972)).

The left side of Figure 9 shows a collection of these data sets as well as three pro-
 posed fits of the dependence of ventilation on X_v for spheres (Hall & Pruppacher, 1976,
 solid), dendrites (Nettesheim & Wang, 2018, NW17, long dashed), and columns (Ji &
 Wang, 1999, JW99, short dashed). The formulation of Hall and Pruppacher (1976) shows
 reasonable behavior for (nearly) spherical particles, but especially for prolate particles,
 large underestimations of the ventilation coefficient are given (up to 3 for a given X_v).
 Using the collected data set, we modify the formulation of Hall and Pruppacher (1976,
 cf. Eq. 30) by adding a ϕ -dependent term to the ventilation coefficient

$$\begin{aligned}
 f_{v,\text{prolate}} &= f_v + c_1 X_{v,\text{equiv}} \phi, & \text{for } \phi > 1, & \quad c_1 = 2.8 \times 10^{-2}, \\
 f_{v,\text{oblate}} &= f_v + c_2 X_{v,\text{equiv}}^{3/2} \phi^{-1}, & \text{for } \phi < 1, & \quad c_2 = 2.8 \times 10^{-3}.
 \end{aligned}
 \tag{35}$$

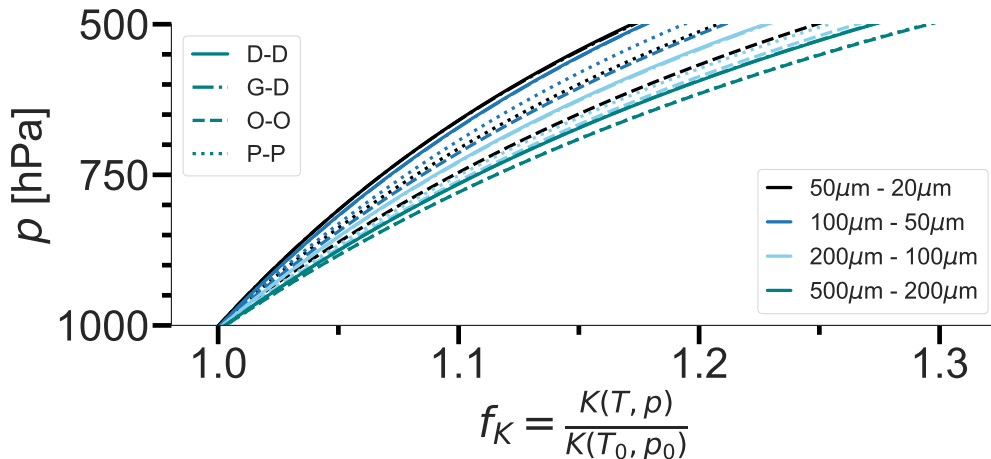


Figure 7. p -profiles of f_K for a drop-drop (D-D, solid), graupel-droplet (G-D, dash-dotted lines), an oblate-oblate (O-O, dashed), and a prolate-prolate collision (P-P, dotted). Color-coded is the equivalent diameter of the colliding particles.

307 Good agreement with the data can be found for all geometries (right side of Figure 9).
 308 It is important to note that we have not introduced any feedback between this shape-
 309 dependent (overall) ventilation coefficient (Eq. 9) and the effect of ventilation on the in-
 310 herent growth function (Eq. 15). The latter only uses the generalized form of Hall and
 311 Pruppacher (1976) and considers the habit effect individually.

312 4.2 Inherent Growth Function

313 The IGF, as introduced by CL94, can describe primary and secondary habit devel-
 314 opment in the spheroidal framework (e.g. Jensen & Harrington, 2015; Sulia & Har-
 315 rington, 2011; Shima et al., 2020)). While providing a fundamental physical description
 316 of the growth ratio of the a - to c -axis, the original fit of observational and laboratory re-
 317 sults has some inconsistencies when compared with more recent laboratory (Connolly
 318 et al., 2012) or modeling studies (Sheridan et al., 2009; Hashino & Tripoli, 2007) for cer-
 319 tain temperature regimes.

320 In this section, we will evaluate the results using the original IGF, point out its de-
 321 ficiencies, and propose another version of the IGF based on observational evidence that
 322 corrects some of the shortcomings.

323 4.2.1 Original version of Chen & Lamb

324 Takahashi et al. (1991, TH91) provide a set of laboratory measurements that quan-
 325 tify the depositional growth of ice crystals at constant temperature ($T \in [250 \text{ K} - 270 \text{ K}]$)
 326 and water saturation. Because of the high quality measurements of the mass, density,
 327 and geometry of individual ice crystals, J.-P. Chen and Lamb (1994b) use the TH91 ex-
 328 periments as a benchmark to validate their habit prediction scheme. Figure 10 repro-
 329 duces Figures 7-9 of J.-P. Chen and Lamb (1994b) using results from the HP scheme
 330 without (black) and with the new habit-dependent ventilation coefficient (green lines).
 331 It also includes the result with a diagnostic geometry for monomers using the empiri-
 332 cal m - D relationship of Mitchell (1996) for aggregates of side planes, columns, and bul-
 333 lets (S3, long dashed lines) and a strictly spherical geometry (short dashed lines). In the
 334 lab experiment, the particles freeze from a droplet distribution and the size/weight shows

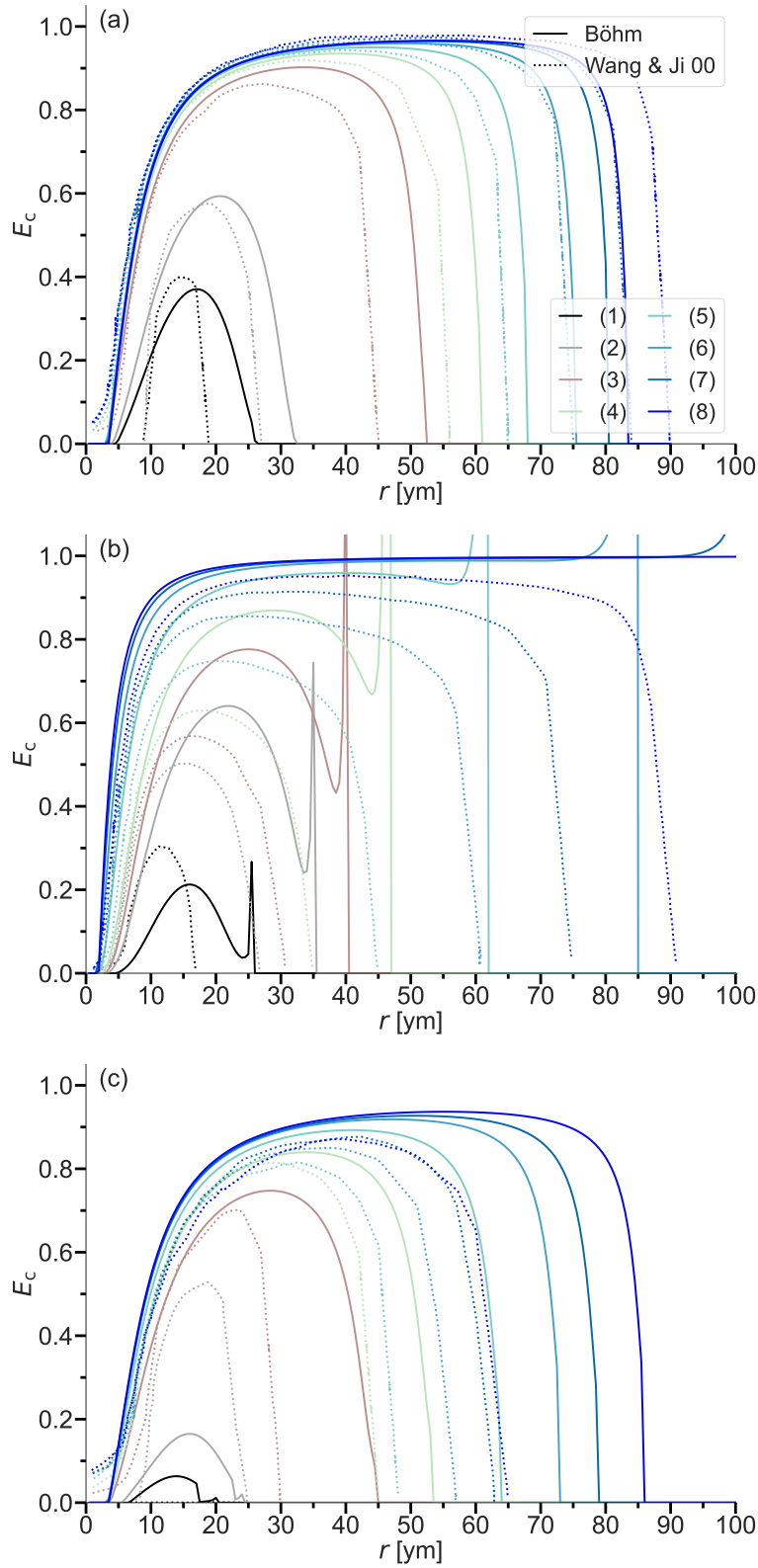


Figure 8. Collision efficiencies of a) thin oblates, b) cylinders, and c) broadly branched crystals with spheres. Particle dimensions and reference numerical simulations of Wang and Ji (2000).

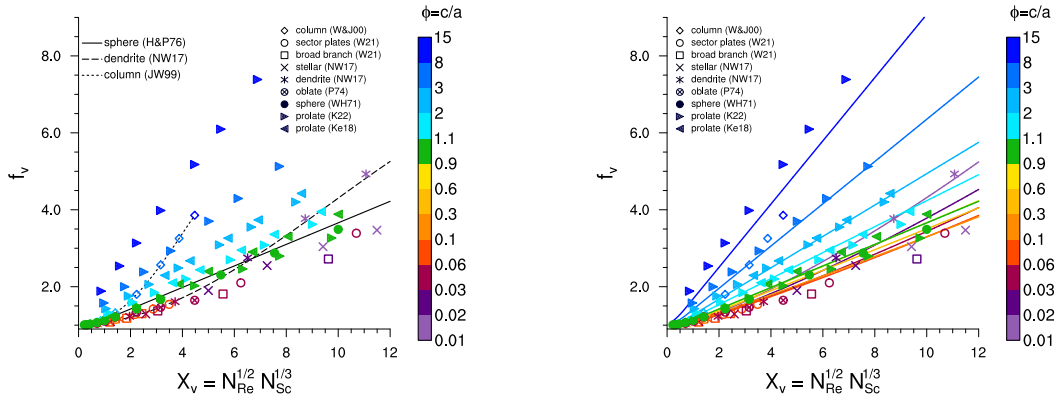


Figure 9. Left: Data points and functional dependencies of $f_v(X_v)$ for several studies. Right: Proposed functional habit-dependent description $f_v(\phi)$. The aspect ratio of the assumed particles is color-coded.

slight variations. In the simulations, an initial radius similar to the maximum of the droplet distribution of $r_{\text{start}} = 2 \mu\text{m}$ (Takahashi & Fukuta, 1988) shows overall good agreement with the laboratory data and compares significantly better than the m - D -relationship of Mitchell. The difference in the initial radius is considered small compared to the uncertainties of the measurements and the model assumptions.

For the limiting case of spherical development at $\Gamma = 1$ for temperatures $T \in [253 \text{ K}, 263 \text{ K}]$, the habit prediction is in agreement with the results for spherical particles, and the laboratory results show slightly lighter crystals. In the columnar regime, $T \in [248 \text{ K} - 252 \text{ K}]$ (cold) and $T \in [263 \text{ K} - 268 \text{ K}]$ (warm), the prolates are heavier. For the oblate maximum around $T = 258 \text{ K}$ they are lighter than laboratory data suggest. Since $X_{v,\text{equiv}}$ does not exceed 1.5 for all particles studied, we see only a slight enhancement of the deposited mass for all non-spherical growth regimes when the habit-dependent ventilation coefficient is included. As expected, prolates are more influenced than oblates, but not enough to change the geometry or density significantly (Fig. 10b&c). From here on, all results will include the habit-dependent ventilation coefficient.

The differences between our model and the laboratory data for particle mass are due to the predicted geometry, too high/low apparent density, or a combination of both. Therefore, Figure 10 (b) and (c) show that within the warm columnar regime, prolates tend to grow to larger aspect ratios than suggested by the laboratory data. Nevertheless, the eventual hollowing captured by the deposition density parameterization is representative. The axis length of oblate growing particles follows the results for the a axis, while showing an inability to represent strongly branched, thin dendritic crystals. This feature is due to the spheroidal assumption and the initial spherical growth up to $D \geq 10 \mu\text{m}$, leading to an overestimation of the c axis size.

If all particles were allowed to grow habit-specifically immediately after nucleation it would reduce the differences observed for the oblate geometry, but leads to unnatural aspect ratios in the columnar regime. The coupling of IGF and deposition density leads to branching for the entire oblate regime and does not reproduce the sharp density minimum for branching particles observed by TH91.

Particles within the cold columnar regime ($T < 253 \text{ K}$) evolve prolate features with a secondary maximum, while TH91 observe nearly spherical or only slightly prolate particles. The habit description becomes ambiguous for the temperature range due to the increased occurrence of polycrystals (based on field observations e.g. Um et al. (2015)). The complex shape of polycrystals and their density cannot be adequately captured by the spheroidal approach. However, model agreement with laboratory data on ice mass deposition is improved by the explicit habit prediction and habit-dependent ventilation.

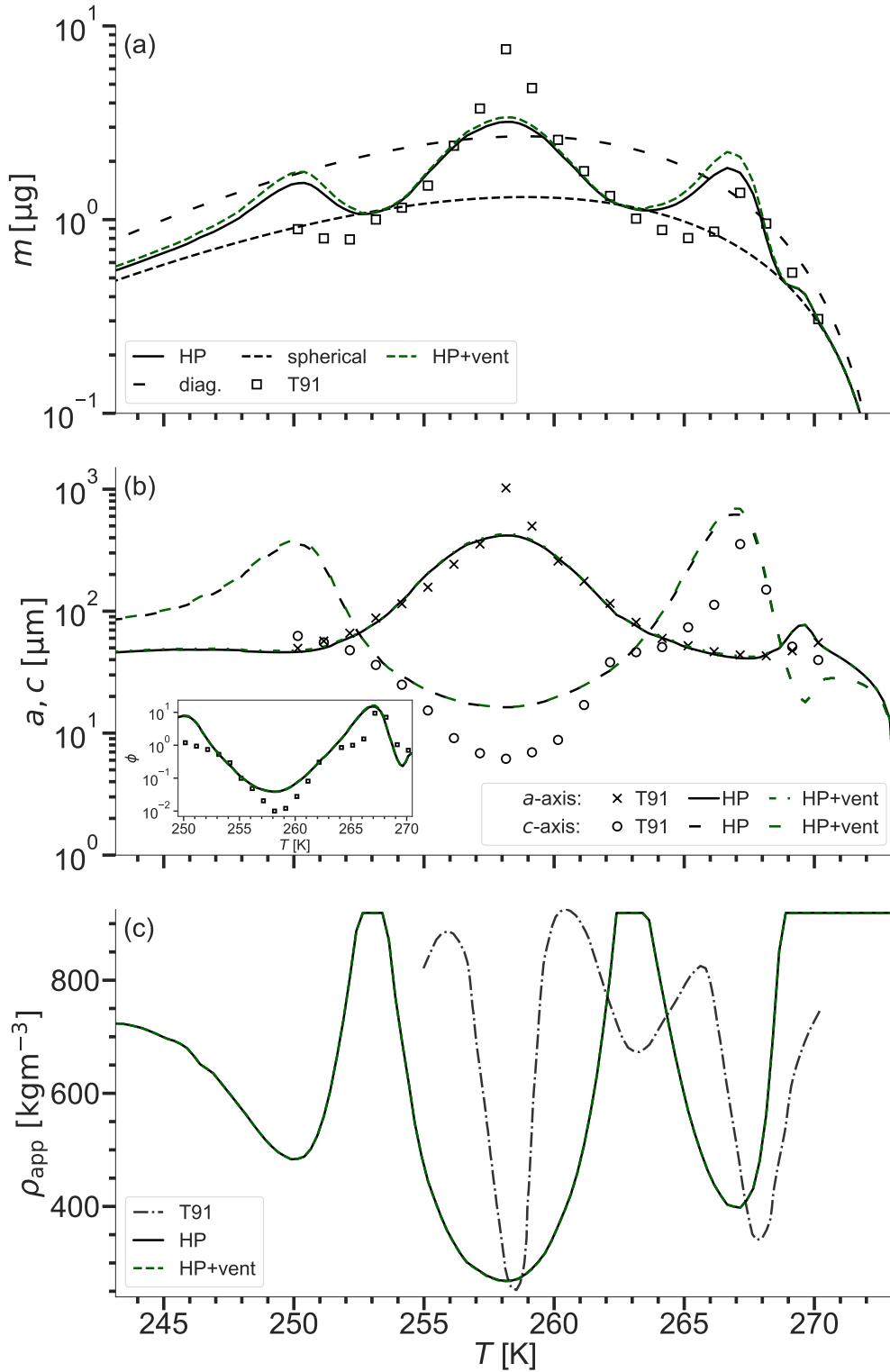


Figure 10. T -dependence of (a) m , (b) geometry (a -, c -axis, ϕ), and (c) ρ_{app} after 10 min of vapor deposition. The black line shows results for the baseline HP, green lines include the habit-dependent ventilation coefficient, and the markers show results of Takahashi et al. (1991, TH91). (a) includes a line for a particle with a diagnostic geometry (diag., long dashed) and that for a spherical crystal (short dashed).

371

4.2.2 Polarimetric signal of model results

372

373

374

375

376

377

378

379

380

381

382

383

384

385

386

387

388

389

390

391

392

393

394

395

396

397

398

399

400

401

402

403

404

405

406

407

408

To further analyze the modeled results, we use the methods proposed by Myagkov, Seifert, Wandinger, et al. (2016) to calculate the polarizability ratio for the different temperature regimes. Myagkov, Seifert, Bauer-Pfundstein, and Wandinger (2016) combines the methods of Melnikov and Straka (2013) and Matrosov et al. (2012) to obtain the polarizability ratio ρ_e (PR) from a 35 GHz cloud radar with a hybrid polarimetric configuration. The PR is based on the particle shape and its dielectric properties and can be used to retrieve information about the environmental conditions under which particles develop certain habits and apparent densities. For their analysis, only particles near cloud top are considered since these observed characteristics developed in local conditions and particle mixtures are unlikely. Myagkov, Seifert, Wandinger, et al. (2016) show that observed PRs are similar to those obtained from the free fall chamber of Takahashi et al. (1991) within the uncertainties of the (temperature) measurements. The PR analysis provides insight into the functional coupling between geometry and density via the IGF (Eq. 7). It is important to note that the sensitivity of the PR to a change in geometry is higher for high particle densities (see Fig. 2 of Myagkov, Seifert, Wandinger, et al. (2016)).

Figure 11 compares the PRs of TH91 (open grey triangles, all growth times), observations near cloud tops (Myagkov, Seifert, Wandinger, et al., 2016, black squares), and the results after three and ten minutes of simulated growth with HP (pluses/circles, color indicates app. density). We show two different time steps of *McSnow* to distinguish between primary and secondary habit effects of oblates: after three minutes, only primary habits develop, so that particles reach a maximum PR before branching. The qualitative results of the HP compare well with TH91 and observations. Particles with the most extreme PRs do not develop in *McSnow*, and their transition between regimes appears to be shifted.

For the maximum in the warm prolate regime, the particles appear to have the correct aspect ratio (Fig. 10(b)) with a slightly lower PR than the observations. This finding suggests that the warm prolate maximum of the IGF may cause excessive hollowing. In addition, the maximum may be too broad, causing an offset in the transition regime.

Oblates that turn out not to be thin enough (cf. Fig. 10b)) result in a PR that (after three minutes) is not as low as suggested by the observations, but is qualitatively consistent. The strong branching of the particles throughout the oblate-favoring regime leads to an overestimated reduction of the PR for the simulated particles. According to this analysis, it seems necessary to postpone branching to later stages of particle evolution.

Warm oblates ($269 < T < 273$ K) and the cold prolate maximum ($T < 252$ K) cannot be fully evaluated due to a lack of observational data points. However, existing laboratory measurements suggest that these maxima may be overestimated. The above deficiencies for the specific regimes are:

409

410

411

412

1. oblate minimum around $T = 269$ K is too low,
2. prolate maximum around $T = 267$ K too high m with too low ρ_{app} ,
3. crystals around $T = 258$ K not thin enough ,
4. cold prolate/polycrystal regime exhibits has too high m and ϕ .

413

4.2.3 Updated Inherent Growth Function

414

415

416

417

418

419

420

421

To overcome the above deficiencies, we propose a modification of the IGF and related assumptions to improve the habit-dependent particle growth. Starting from point one, there is no clear evidence for a strong oblate minimum at $T = 269$ K, either from the observations shown above or from other sources such as Bailey and Hallett (2009). We therefore use the values suggested by Sei and Gonda (1989). Future retrievals may be useful to evaluate this change.

Point two can be addressed by reducing the IGF maximum around $T = 267$ K by 25% and fitting the curve to $\Gamma = 1$ at the appropriate temperatures. This change should

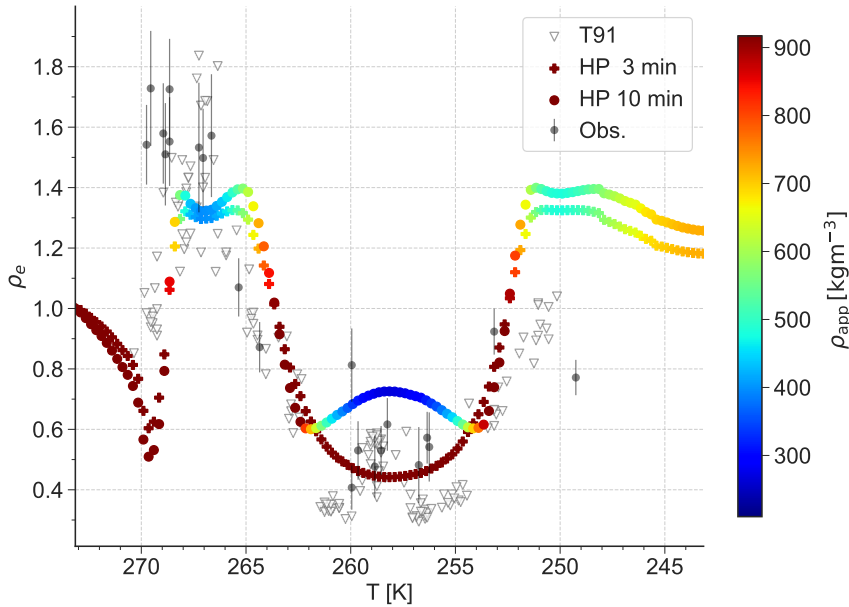


Figure 11. T -dependence of polarizability ratios ρ_e for ice crystals grown in the free-fall chamber (open grey triangles), with HP ([+] for $t = 3$ min, [•] for $t = 10$ min), and observed near cloud tops (black squares, error bars represent ± 1 standard deviation). Color-coded is the particle's apparent density ρ_{app} .

422 result in slightly shorter, lighter, but denser columns that better match the TH91 data.
 423 For PR, the geometric change is (partially) offset by an increase in density.

424 In the oblate growth regime, the IGF initially produces the correct geometries (cf.
 425 3 min results), but branching seems to occur too early and for a relatively wide range
 426 of planar particles. Comparing the simulated density with the wind tunnel results (Fig. 10c),
 427 we see that particles branch only for a narrow temperature range. So instead of chang-
 428 ing the IGF, we change the branching criterion to better resemble the onset of branch-
 429 ing. In the formulation of JH15, branching does not occur before $a \geq 100 \mu\text{m}$. Here,
 430 we assume that particles branch when $a \geq 200 \mu\text{m}$, effectively delaying the onset of branch-
 431 ing.

432 For the final point, we merge the time-dependent growth rates of TH91 (Tab. 2 of
 433 Takahashi et al., 1991) with the results of Sheridan (2008) and Sheridan et al. (2009).
 434 Connolly et al. (2012) also report a discrepancy between observed and modeled crystals
 435 for the regime around $T = 253 \text{ K}$ using CL94's IGF, but they assume oblate growth
 436 for colder temperatures. Due to the dominance of polycrystals, it becomes difficult to
 437 generalize these habits to either prolate or oblate spheroids. The advantage of assumed
 438 columnar growth is the immediate hollowing, which effectively reduces the apparent den-
 439 sity, whereas if oblate growth is assumed, the branching criterion of JH15 is not met be-
 440 cause the particles remain nearly spherical.

441 Figure 12 shows the original IGF (black) and our proposed version (blue line) combin-
 442 ing the above modifications, together with the diagnosed Inherent Growth Ratios of
 443 Takahashi et al. (1991) (red and black dots). In Figure 13, results of the depositional growth
 444 experiment using the new IGF (blue lines) are compared with the original results (black
 445 lines) for mass, axis measure, and apparent density. Using the new IGF, the accumu-

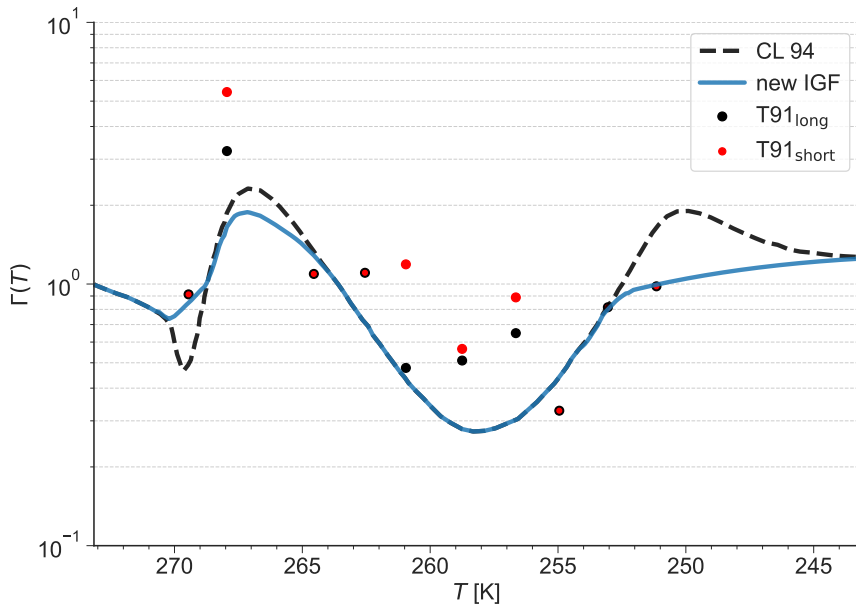


Figure 12. Inherent Growth Function of CL94 and our new formulation as a function of temperature. Explicit values of Takahashi et al. (1991) are marked as red and black dots.

446 lated mass is decreased for the warm prolate peak as well as in the polycrystalline regime,
 447 removing the secondary peak (colder $T = 253$ K) (Fig. 13a). In terms of geometry, the
 448 changes induced by the modified IGF are suitable for both prolate regimes. There is no
 449 modification of the IGF in the oblate regime around $T = 258$ K. The reduction of the
 450 warm oblate ϕ minimum is in good agreement with the laboratory results. The result-
 451 ing changes in particle density are negligible.

452 A second experiment includes the modified IGF, combined with the modified branch-
 453 ing criterion of $a \geq 200 \mu\text{m}$ introduced above (IGF2+, red lines). The lower limit of
 454 $D > 10 \mu\text{m}$ for habit development can be physically justified by the studies mentioned
 455 above, but at the same time it prevents the development of very thin oblates observed
 456 by Takahashi et al. (1991). In this setup we therefore remove the limiter and allow free
 457 evolution after nucleation, which gives the best agreement with TH91. The modifications
 458 result in more mass being deposited around $T = 258$ K, bringing the results closer to
 459 the TH91 measurements. In terms of geometry, the transition from the oblate to the poly-
 460 crystalline regime as well as the shape of the oblates are very similar to the measurements.
 461 The coupling of the IGF and the deposition density leads to subsequent changes in the
 462 apparent density. It seems difficult to assess the change in apparent density, but the nar-
 463 rowed oblate minimum seems justified, while the warm prolate minimum might overes-
 464 timate the particle density. To evaluate the combined effect of shape and density, we an-
 465 alyze the PR with the updated IGF including the additional modifications. Figure 14
 466 confirms that this setup can remove the major deficiencies between the laboratory mea-
 467 surements and the simulation. The warm oblate regime shows higher PRs, while the warm
 468 prolate maximum is slightly closer to the majority of observational data due to the in-
 469 terplay of geometry and density (less hollowing). Nevertheless, the highest PRs cannot
 470 be matched. This discrepancy can be attributed to the parameterization of the hollow-
 471 ing, since the AR is well matched. In the cold oblate regime, delayed branching signif-

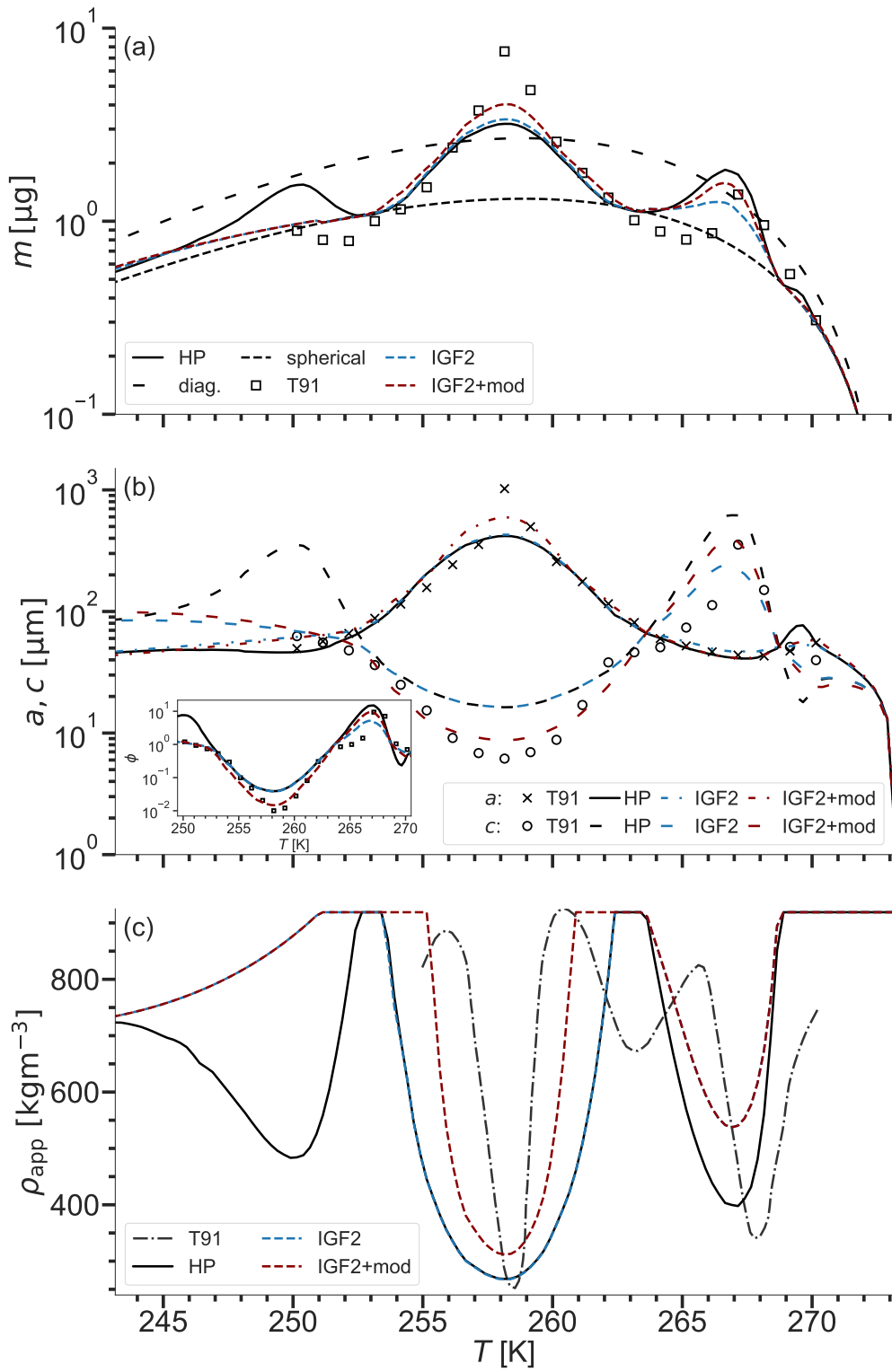


Figure 13. As Fig. 10 but also compared with the results of the updated IGF (blue) and of the updated IGF including branching modification (IGF2+, red).

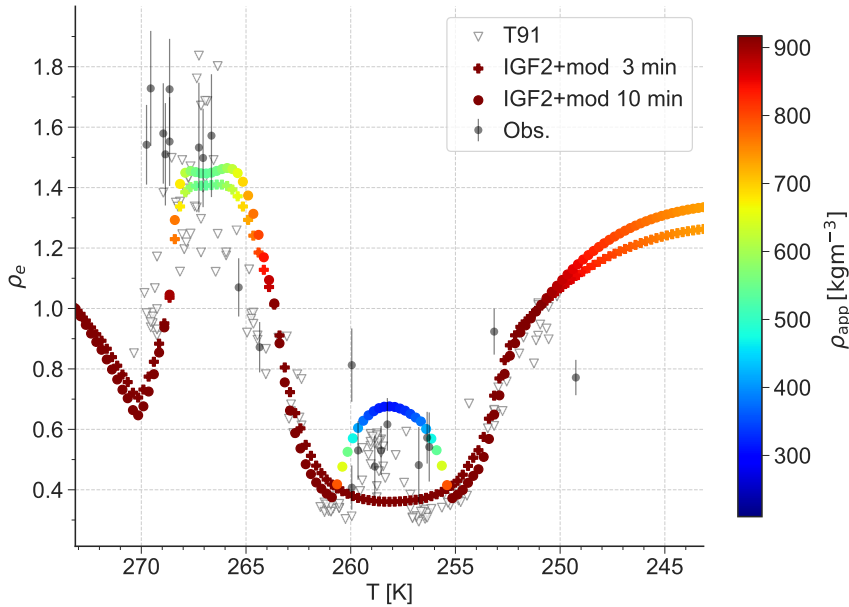


Figure 14. As Fig. 11 but with the new IGF and altered branching criterion.

472 icantly improves the agreement of the PR with the observational and T91 results. The
 473 evolution of particles with very low PRs ($\rho_e < 0.4$) can be observed after three min-
 474 utes, as suggested by the measurements. The same is true for the increase in PR due to
 475 strong branching around $T = 258$ K. Finally, the transition from oblate to polycrys-
 476 tals seems to agree better with the results of T91 and Myagkov, Seifert, Wandinger, et
 477 al. (2016). For possible further modifications of this version of the IGF, more retrieved
 478 observational or laboratory data are needed. In particular, the regimes that are sparsely
 479 populated by measurements (such as the polycrystalline region) could be of great benef-
 480 it to such a detrimental function as the IGF.

481 5 Case study exhibiting sensitivities

482 Habit prediction has a pronounced impact on many microphysical processes and
 483 can introduce variability among particles by abandoning static m - D and v_t -relations. *Mc-*
 484 *Snow* is unique in the sense that it combines the habit prediction scheme of J.-P. Chen
 485 and Lamb (1994b) and Jensen and Harrington (2015) with the full set of parameteriza-
 486 tions of Böhm. Using Böhm's framework for the parameterization of particle properties
 487 allows a physically consistent and mathematically continuous description of the habit
 488 dependency of most microphysical processes. The effect of habit prediction on particles
 489 at constant temperature has been shown in Figure 10, but this setup can only serve as
 490 a limiting case. In real clouds, hydrometeors experience different thermodynamic con-
 491 ditions and change the conditions themselves by absorbing/releasing water and latent
 492 heat. We soften the constraints implied by the laboratory setting by focusing on a setup
 493 where particles fall through a one-dimensional column (rain/snow shaft) with a prescribed
 494 atmospheric profile. The model setup (Fig. 15) is defined to mimic different sections in-
 495 side a cloud where certain relevant ice-microphysical processes dominate. In the upper
 496 part, depositional growth of small particles should govern the evolution. The ice mass

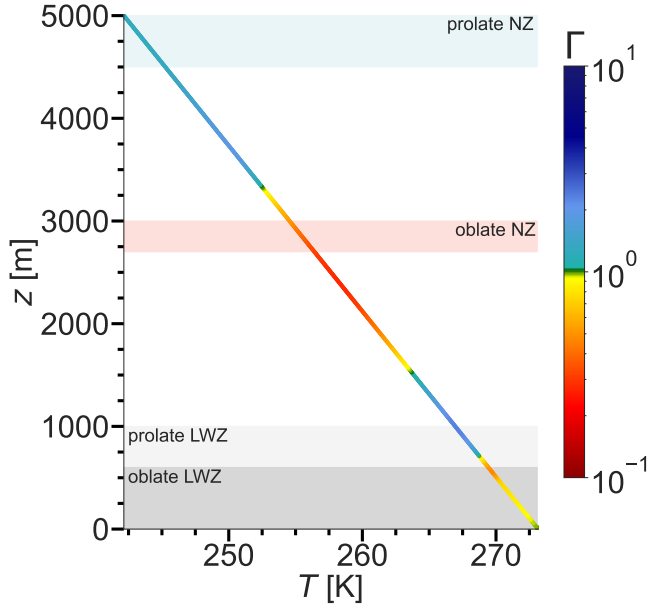


Figure 15. Background atmosphere for the 1-D model simulations incl. the vertical profiles of temperature and corresponding IGF. The nucleation (NZ) and liquid water zones (LWZ) are situated in the shaded regions for the respective cases.

497 accumulated by deposition changes the shape and fall velocity. Both terminal velocity
 498 and geometry are linked to the likelihood of collision events and change the onset of ag-
 499 gregation and how effective it is. In the lower part of the profile, both monomers and
 500 aggregates encounter a liquid water zone (LWZ) where the impact of the ice habit on
 501 the effectiveness of riming is examined.

502 5.1 Setup

503 Similar as in Brdar and Seifert (2018), the temperature profile is constructed using
 504 the surface temperature of $T_{\text{surf}} = 273 \text{ K}$ and a constant lapse rate of $\gamma = 0.0062 \text{ Km}^{-1}$.
 505 The domain height is case specific with $z_{\text{top}} = 5000 \text{ m}$ ($T_{\text{top}} = 242 \text{ K}$) for a prolate
 506 and $z_{\text{top}} = 3000 \text{ m}$ ($T_{\text{top}} = 254.4 \text{ K}$) for an oblate favoring regime. Water vapor, liq-
 507 uid water, and temperature are assumed to be constant and not increased or decreased
 508 by any microphysical process.

509 In the upper 80% of the (case-specific) domain, particles grow solely by vapor de-
 510 positional growth and aggregation at a supersaturation of 5%. In the lower 20%, the
 511 regime is dominated by riming due to a liquid water zone ($LWC = 0.2 \text{ gm}^{-3}$), which
 512 enhances particle growth and in turn increases the probability of aggregation. We do not
 513 impose a subsaturated regime because the habit-specific effect is small and possible ag-
 514 gregation events become unlikely due to decreasing particle size. The initial properties
 515 (mass and size) of the ice crystals are drawn from a gamma distribution with a mean
 516 mass equal to the mass of a spherical ice particle with a diameter of $D = 10 \mu\text{m}$, the
 517 initial aspect ratio is set to $\text{phi} = 1$. Particles are generated at a constant nucleation
 518 rate within a nucleation zone that spans 10% of the total domain height. A random ini-
 519 tialization height has a positive effect on the variance of the developed particle habits
 520 due to the different atmospheric conditions compared to constant nucleation at the do-
 521 main top. Particles larger than $D > 10 \mu\text{m}$ are initialized with a density derived from

empirical mass-area relations to avoid underestimating the actual particle geometry and overestimating the fall velocity.

We integrate the model over 10 h to reach a steady state, and all statistical quantities are averaged over the last 5 h. Riming is treated by the stochastic riming scheme (cf. Brdar & Seifert, 2018; Brangi et al., 2020) which makes use of the theory of Böhm for terminal velocity and collision efficiency.

Sheridan et al. (2009) shows that habit development is strongly controlled by conditions shortly after nucleation, when relative changes in mass and shape are most pronounced. Numerical models of the atmosphere typically assume uniform thermodynamic conditions within a grid cell. Especially in regions where the IGF shows strong gradients, the uniform treatment leads to different habits as if the actual thermodynamic conditions at the position of the particles were assumed. In Large Eddy Simulation (LES) and Numerical Weather Prediction (NWP) models the vertical spacing inside clouds can easily exceed $\Delta z = 50$ m (Dziekan et al., 2019; Shima et al., 2020), which already results in a temperature difference between the lower and upper edge of the cell of $\Delta T \geq 0.3$ K (assuming the above temperature gradient). Hence, we strongly recommend an interpolation of the atmospheric state to the particle position, making the habit evolution independent of the resolution of the atmospheric grid.

5.2 Deposition

The results in Figure 10 imply a change in deposition rate due to the habit prediction and the preceding dependencies on capacitance, ventilation, and fall velocity. To study the effect of particle habits without the complex feedback between ice microphysical processes, we suppress aggregation and remove the liquid water layer for the time being. We focus on a prolate and an oblate favoring initial growth scenario as archetypes for typically observed monomer cases and show why it is important to consider ice habits.

5.2.1 Prognostic geometry vs. m - D -relationship

Figure 16 illustrates the diversity of particle properties induced by the temperature dependence (original IGF of CL94) of the habit evolution of the mass, velocity, and density of individual crystals relative to their maximum dimension. Since there is no complete set of empirical formulations, we use individual relations for the variables: mass-size of Mitchell (1996), velocity of A. Heymsfield (1972, Tab. 3), and apparent density from Pruppacher and Klett (1997) for comparison.

Unless otherwise stated, we compare the results of the explicit habit prediction with those of simulations using the diagnostic geometry for monomers and aggregates as introduced by Brdar and Seifert (2018) using the power law of Mitchell (1996) for aggregates of side planes, columns, and bullets.

Like Shima et al. (2020), we use the normalized mass of the ice particles

$$\bar{m} = \frac{m}{\rho_i \frac{\pi}{6} D^3}, \quad D = 2 \max(a, c) . \quad (36)$$

The terminal velocity has been normalized to surface conditions $v_{t,0}$ to remove the direct atmospheric effect (see Sec. 3.2) and ease comparison with the empirical equations of A. Heymsfield (1972) that assume a reference pressure of $p = 1000$ hPa.

The empirical mass-size-relations for aggregates, plates, columns, or broadly branched crystals of M96 may be able to estimate an average behavior of the mass-size spectrum for certain diameter ranges, but the variations caused by local temperature and supersaturation effects seem impossible to describe with prescribed thresholds or a mixture of static relations. Depending on the nucleation conditions prescribed by the initialization height and mass, the particles develop different characteristics for the same maximum dimension. For larger maximum dimensions, we see that the diagnostic geometry of aggregates tends to underestimate the prolate and overestimate the oblate particle mass, demonstrating the weakness of using the diagnostic approach for the differ-

ent regimes. Habit-specific relationships do not significantly improve the agreement, and to use them additional thresholds based on particle properties would have to be defined. This strongly emphasizes the importance of the HP for predicting ice growth in clouds.

Specifically for the mass of prolate particles, a sharp increase around $D = 0.4$ mm can be observed, accompanied by an increase in velocity and apparent density. This behavior cannot be matched by the slope of any empirical relation and exhibits a caveat of the deposition density description for secondary habits as formulated by JH15: the deposition density is generally dependent on the surrounding conditions and is assumed to approach ice density for the transition from prolate-favoring to oblate-favoring conditions (and vice versa) ($\Gamma \rightarrow 1 \Rightarrow \rho_{\text{app}} \rightarrow \rho_i$, cf. Eq. 7). Because the columns cannot satisfy the branching criterion of JH15, they grow with ice density not only when in regions that mandate spherical growth, but also when falling in oblate-favoring conditions where the addition of high-density mass causes acceleration (Fig. 16(b)). Coupled with the comparatively short residence times in habit-forming regimes due to high fall velocities, columns do not substantially change the habit they initially formed under conditions close to their nucleation height. The deposition density for habits growing in unfavorable conditions is unknown. Comparison with the empirical relation for apparent density suggests that the assumption of secondary habits (immediate onset and subsequent degree of hollowing) may be overstated.

Particles nucleated under oblate-favoring conditions can form relatively small ARs once they begin to branch. The development of a large area presented to the flow increases the drag, leading to an almost constant terminal velocity at large diameters. This feedback positively supports habit development in the prevailing atmospheric conditions. Compared with the empirical relation of the apparent density of dendrites, the onset of branching seems premature and further motivates our changes to the branching criterion. Oblates that fall into conditions of higher deposition density experience an increase in apparent density. It is unclear if this behavior can be physically motivated or is a feature of the coupling between IGF and deposition density. Hashino and Tripoli (2007) hypothesize that dendritic arms grow under prolate-favoring conditions due to an increased ventilation effect along the tips, while there is no current theory for columns. Future laboratory experiments may help to better understand this behavior and motivate a modified treatment of the modeled particles, but for now, we stick with the secondary habit treatment proposed by JH15.

To get a quantitative impression of the average effect of the habit prediction, Figure 17 shows the vertical profiles of mass flux, deposition rate, and mass-weighted terminal velocity \bar{v}_t . A comparison of particles following the m - D -relation of aggregates from Mitchell (1996, solid lines) with the original formulation of cylindrical hydrodynamic behavior of Böhm (1992a) (long-dashed, HP) shows that the habit prediction significantly reduces mass flux (precipitation rate, Fig. 17a). The diagnostic geometry predicts larger areas for particles of a certain maximum dimension than those of prolate spheroids of the habit prediction. This drastically increases the deposition rate (Fig. 17b) via the increased capacitance, while leading to lower fall velocities for the same mass (Fig. 17c). Slower particles prolong the residence time, leading to even more depositional growth that cannot be compensated for by the increased ventilation effect for the fast columnar particles. In turn, particles that follow the m - D -relationship can develop up to twice the mass flux of particles that develop a habit.

Using the interpolation for the velocity of prolates increases the observed difference and further reduces the mass flux due to the effective acceleration of the particles (see section 3.1). Upcoming results will only use the interpolated fall velocity for prolates due to consistency with laboratory results.

The behavior of particles nucleated under oblate-favoring conditions qualifies the results of the simplified experimental setup of Takahashi et al.: Plates generate more mass than particles with a diagnostic geometry, but the effect is less pronounced than for prolates. Even at higher masses, oblates have a slightly longer residence time than particles without a habit. The development of thin plates or dendritic structures increases

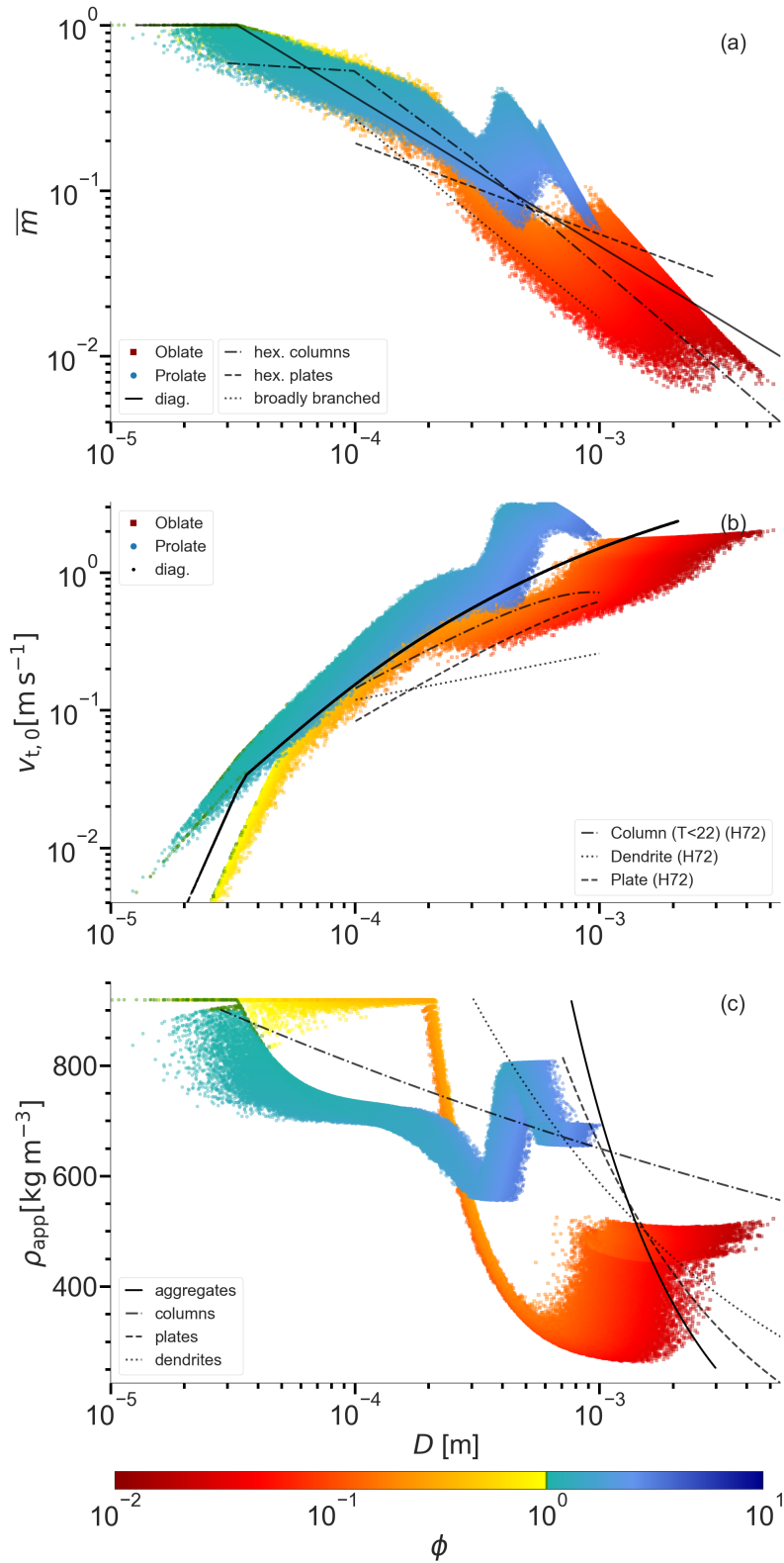


Figure 16. \bar{m} - D (a), $v_{t,0}$ - D (b), and ρ_{app} - D -relations (c) for the steady state of the simulation. Markers represent the simulations using a diagnostic geometry and an explicit habit prediction. The particles AR ϕ is color-coded. Lines in (a) are empirical relations of Mitchell (1996), in (b) of A. Heymsfield (1972), and in (c) from Pruppacher and Klett (1997).

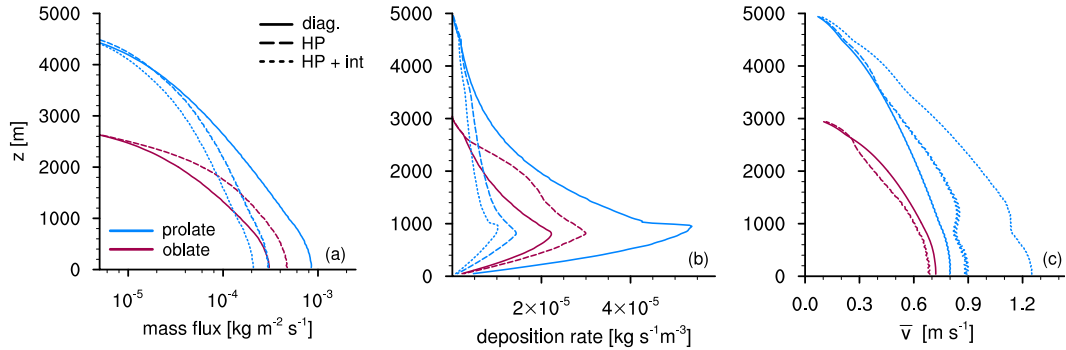


Figure 17. Comparison of vertical profiles of (a) mass flux, (b) deposition rate, and (c) mass-weighted velocity \bar{v} for particles nucleated in a prolate (blue, $\Delta z_{\text{nuc}} = 4500 - 5000$ m) and an oblate (red, $\Delta z_{\text{nuc}} = 2700 - 3000$ m) regime using a diagnostic geometry (solid), habit prediction with cylinder (dashed), and habit prediction with interpolated velocity for prolates (short-dashed).

625 the surface area, causing a positive feedback on capacitance and ventilation, amplified
 626 by habit-dependent ventilation, increasing the deposition rate.

627 An opposite effect on the first-order variables of the two categories of habits can
 628 be observed: the HP effectively causes an increase in precipitation mass for oblate par-
 629 ticles and a decrease for prolate particles (such as the mass flux/precipitation).

630 5.2.2 Updated IGF

631 While we do not expect the effect of the updated habit scheme to be nearly as pro-
 632 nounced as in the isolated laboratory setup of Takahashi et al., the changes may initial-
 633 ize altered habit developments. In particular, particles nucleated in the cold prolate regime
 634 remain more spherical and are therefore more prone to primary habit change. Figure 18
 635 shows the changes in both growth regimes caused by the modifications of the IGF, in-
 636 cluding the branching criterion. The flattening of the prolate maximum in the cold regime
 637 ($T < 253$ K) leads to the evolution of fast falling crystals because their AR remains close
 638 to sphericity and their apparent density is comparatively high, improving the agreement
 639 with the empirical relation of the apparent density of columns. These crystals short resi-
 640 dence times result in reduced total depositional growth and maximum dimension, and
 641 ultimately shorter lifetimes as they fall out as precipitation.

642 The change in branching criterion delays the development of porous structures for
 643 plates, and the more compact shape results in an initially increased terminal fall veloc-
 644 ity. As soon as strong branching sets in, v_t reaches lower velocities as for the original branch-
 645 ing criterion closer to the empirical relation for dendrites of A. Heymsfield (1972). The
 646 delayed onset of branching agrees well with the empirical relation for the apparent den-
 647 sity of dendrites.

648 Generally, the modifications to the IGF and branching criterion show the desired
 649 impact on mass and apparent density while terminal velocities are fairly high.

650 The average vertical profiles in Figure 19 allow to summarize the quantitative behav-
 651 ior: The mass flux for plates following the original IGF is significantly increased compar-
 652 ed to the diagnostic counterpart. For the updated formulation, the mass flux is similar
 653 to that of particles without explicit habits. This highlights the importance of the ini-
 654 tial growth phase, where the exact onset of branching significantly affects the particle
 655 characteristics. The new IGF causes a decrease in mass flux for both the columnar and
 656 prolate cases compared to the original IGF configuration for similar reasons: While pro-
 657 lates remain more spherical and less hollow, oblates branch later and the more compact

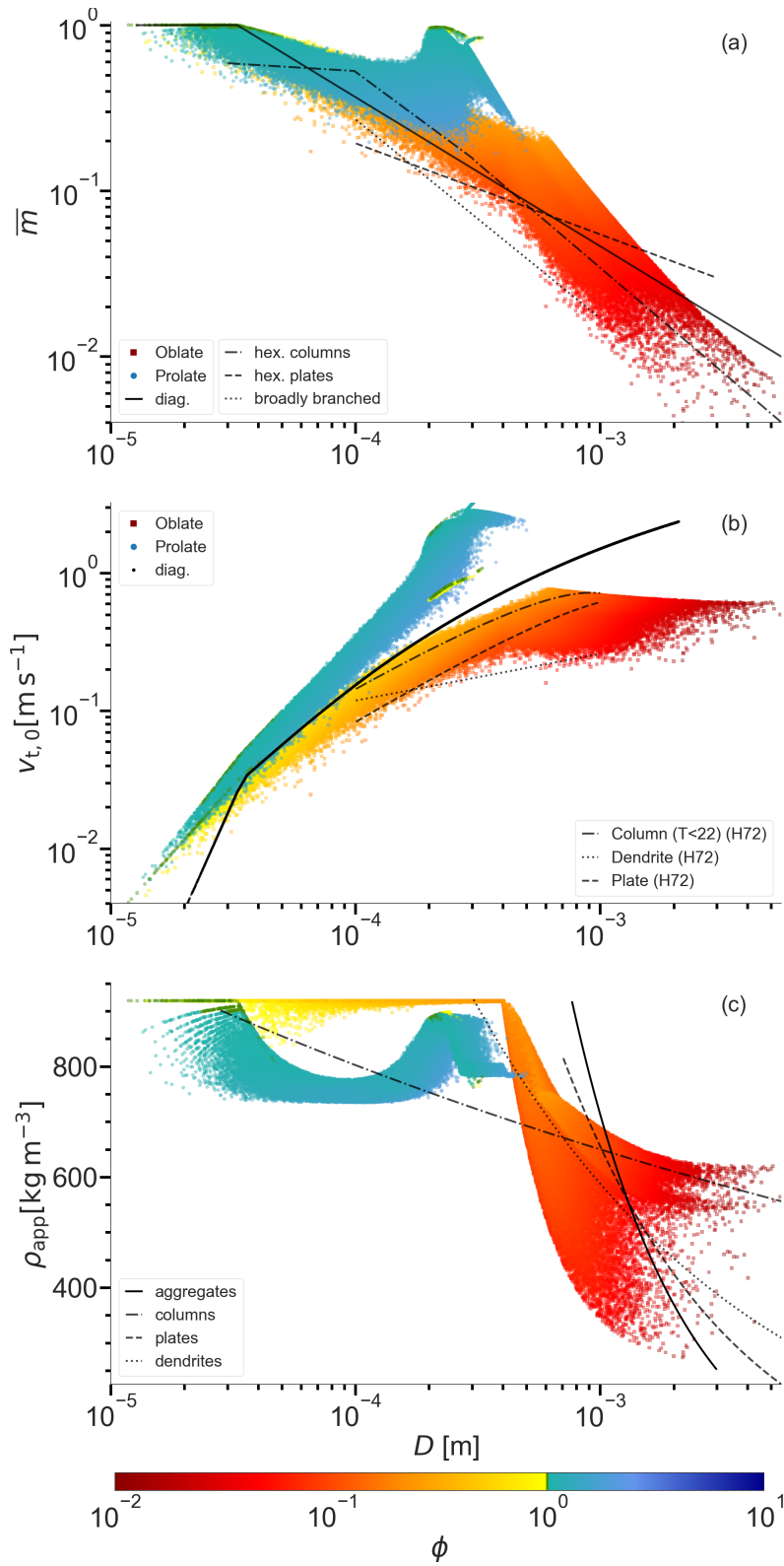


Figure 18. Same as Fig. 16 but using the updated IGF configuration. Lines in (a) are empirical relations of Mitchell (1996), in (b) of A. Heymsfield (1972), and in (c) from Pruppacher and Klett (1997).

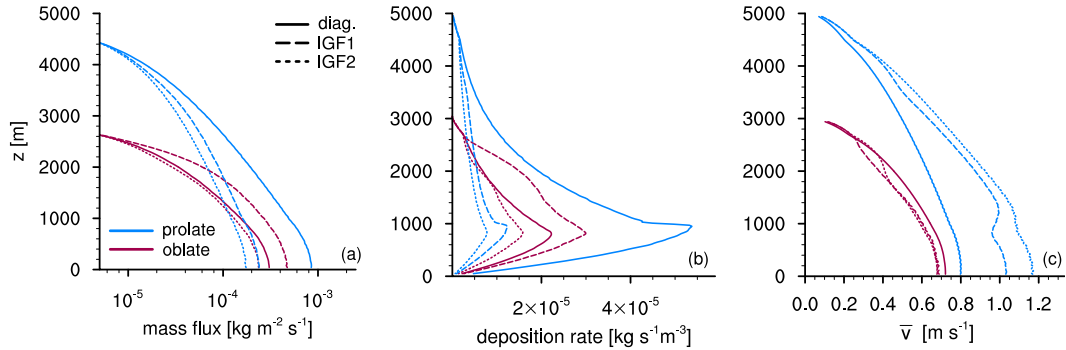


Figure 19. Comparison of vertical profiles of (a) mass flux, (b) deposition rate, and (c) mass-weighted velocity \bar{v} for particles nucleated in a prolate regime (blue, $\Delta z_{\text{nuc}} = 4500 - 5000$ m) and an oblate regime (red, $\Delta z_{\text{nuc}} = 2700 - 3000$ m) using a diagnostic geometry (solid), HP with original IGF (dashed), and HP with updated IGF (short-dashed).

658 geometry shortens the residence time. This can only be seen by comparing Fig. 16 and
 659 18 because the mass-weighted velocity (Fig 19c) does not show the effect of the lighter
 660 particles. The effect of the two IGF versions on habit development is visualized in Fig-
 661 ure 20. For reference, lines are plotted for ϕ - D -relations from Auer and Veal (1970), as-
 662 suming the corresponding nucleation temperature (columnar (dash-dotted) $T < 253$ K,
 663 Plc (dashed): $256 \text{ K} < T < 260 \text{ K}$). The ARs of the prolates developed for the origi-
 664 nal IGF (blue) are similar to those expected from the empirical relations in the corre-
 665 sponding temperature range. Using the new IGF instead, columnar particles develop sim-
 666 ilar ARs for lower D due to the removal of the size constraint on habit development, but
 667 for larger D their ARs are less pronounced and some particles even change their habit
 668 (highlighted in light blue). The classification of these particles is difficult, but they could
 669 be interpreted as complex polycrystals like capped columns. If they are polycrystals, this
 670 raises the question of the apparent density treatment. It seems unlikely that Eq. 7 can
 671 describe the development of secondary habits for polycrystalline structures, since for spheri-
 672 city the deposition densities are at or around ice density.

673 By removing the size constraint on habit development, planar particles (red) are
 674 able to develop strong aspect ratios close to $\phi = 10^{-2}$ (lower right corner) for the up-
 675 dated IGF including modifications. For very large D , the aspect ratios are similar to those
 676 expected from the empirical relation for dendrites.

677 We can conclude that the changes to the IGF and the branching criterion reduce
 678 the mass flux for both scenarios while allowing the development of very thin plates. It
 679 remains an open question how to deal with particles that change their habit, since the
 680 spheroidal approach is limited to simple geometries.

681 5.3 Aggregation

682 The three main factors influencing the aggregation process are the geometric area
 683 A , the fall velocity difference $\Delta v = |v_1 - v_2|$, and the collision efficiency E_c , which de-
 684 pends on the difference in v_t . The habit prediction scheme affects all of the above fac-
 685 tors by introducing variability in particle shape and density, broadening the velocity spec-
 686 trum, and potentially changing the cross sectional area. Here, we use the formulation
 687 from Mitchell (1988) for sticking efficiency, which prescribes piecewise linear values for
 688 temperature ranges. Intuitively, the habit prediction is expected to lead to altered, habit-
 689 specific aggregation rates that feedback on depositional growth. Figure 21 shows the ver-
 690 tical profiles of number density (left column) and mass flux (right column) for the oblate
 691 (top row) and prolate (bottom row) cases, separated into monomers and aggregates. The

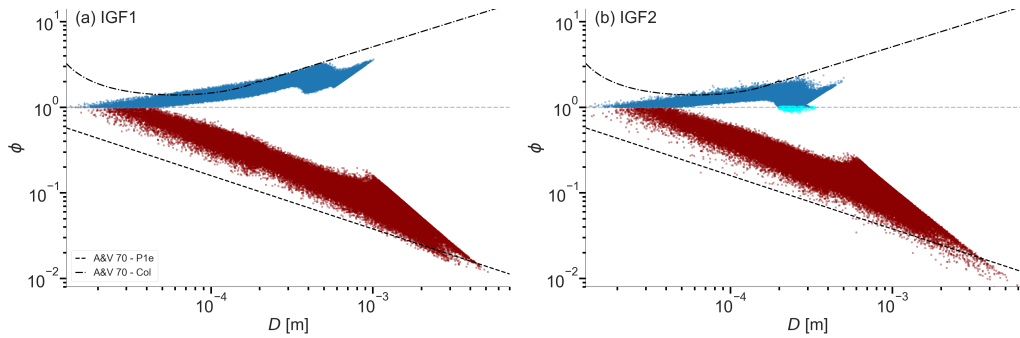


Figure 20. ϕ - D -relations of the two cases for the original IGF (a) and the updated version with modifications (b). The black lines are empirical relations from Auer and Veal (1970).

vertical number density profiles show that the different descriptions of depositional growth and geometry have critical effects on aggregation. The development of dendritic crystals causes an earlier and stronger initial aggregation rate compared to particles without HP and is strongest for the original IGF (crystals branch earlier). Both IGF configurations show a reduction in monomer number density, but the earlier branching critically influences the onset of aggregation and the additional collection of both monomers and aggregates further down. This causes the mass flux for the original IGF to be dominated by aggregates. The number of aggregates for the modified IGF is almost independent of height, indicating that aggregates mainly collect other monomers rather than self-collection of monomers or aggregates. Analysis of the number of monomers per aggregate confirms that mostly large monomers are collected, while smaller crystals rarely aggregate (not shown). Oblate particles grow efficiently by vapor growth and their collection by aggregation does not transfer its positive effects to the aggregates because we assume that their geometry is reduced to the m - D power law. This leads to a reduction in the total mass flux when the HP is compared to the classical m - D -relationship, indicating the effect of the simplified aggregation geometry that immediately forgets the monomer information. A difference between the two IGF configurations for the composition of the total mass flux at the surface is present: for the original IGF, the mass flux is dominated by aggregates and close to equality for the new configuration. The higher total number density leads to more depositional growth because the supersaturation is fixed. If there would be an interactive feedback between hydrometeors and the atmosphere, higher number densities would lead to a faster depletion of the supersaturation.

The prolate case shows the opposite behavior: the reduced depositional growth compared to particles without explicit habit, caused by shorter residence times, leads to smaller cross sectional areas, which in turn decreases the aggregation rates. Particles with a diagnostic geometry, on the other hand, start to aggregate efficiently in the lower half of the domain, where the sticking efficiency is high, so that the number densities of monomers and aggregates constantly decrease and large aggregates form. Aggregates dominate the mass flux when no habits can develop, while for the HP the mass flux is defined by that of the monomers.

The habit prediction has a significant impact on the aggregation of the cases studied. The impact depends on the dominant primary habit, but could be overestimated because in the specific cases no different primary habits coexist that would lead to potentially high aggregation rates.

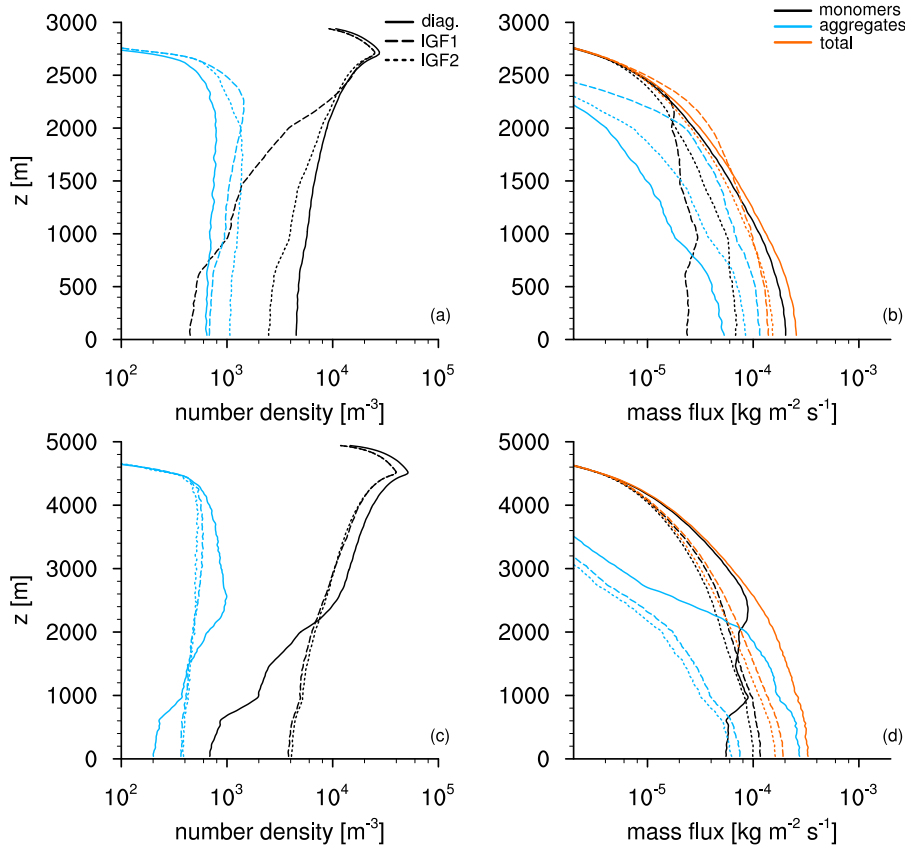


Figure 21. Vertical profiles of number density (a & c) and mass flux (b & d) for monomers (black) and aggregates (blue) for the oblate (top row) and prolate (bottom row) nucleation regimes using a diagnostic geometry (solid), HP with original IGF (dashed), and HP with updated IGF (short-dashed) with deposition and aggregation enabled.

726

5.4 Riming

727

Finally, we enable riming by specifying a liquid water zone in the bottom 20% of the domain (Fig. 22). Particles are classified as rimed as soon as they contain rime mass. For low LWCs, the transition from prolate/oblate monomers may be slow, and habit effects caused by deposition may persist, but high LWCs lead to effective rounding of particles, which can then be described by m - D -relations for rimed particles or graupel (as shown by Jensen and Harrington (2015)).

733

734

735

736

737

738

739

740

741

742

743

744

For the chosen conditions, all particles are large enough to rime immediately upon reaching the LWZ, regardless of configuration. Riming increases the mass and area of the particles while accelerating them, increasing the rate of aggregation and leading to a further decrease in number density. The immediate effect of the added rime mass is to fill the porous structures before effectively increasing the maximum dimension. For particles that do not develop a habit, this leads to a dominance of the acceleration effect over the geometric change. Regardless of the primary habit, particles that are allowed to evolve habits are effectively dragged toward sphericity by the assumption that riming only increases the minor dimension (see Eq. 18 & 19). Therefore, riming accelerates the most pronounced evolved habit through mass growth and rounding. IGF configuration has a weak effect on riming compared to deposition and aggregation. Only for prolates following the original IGF can a more pronounced decrease in number density

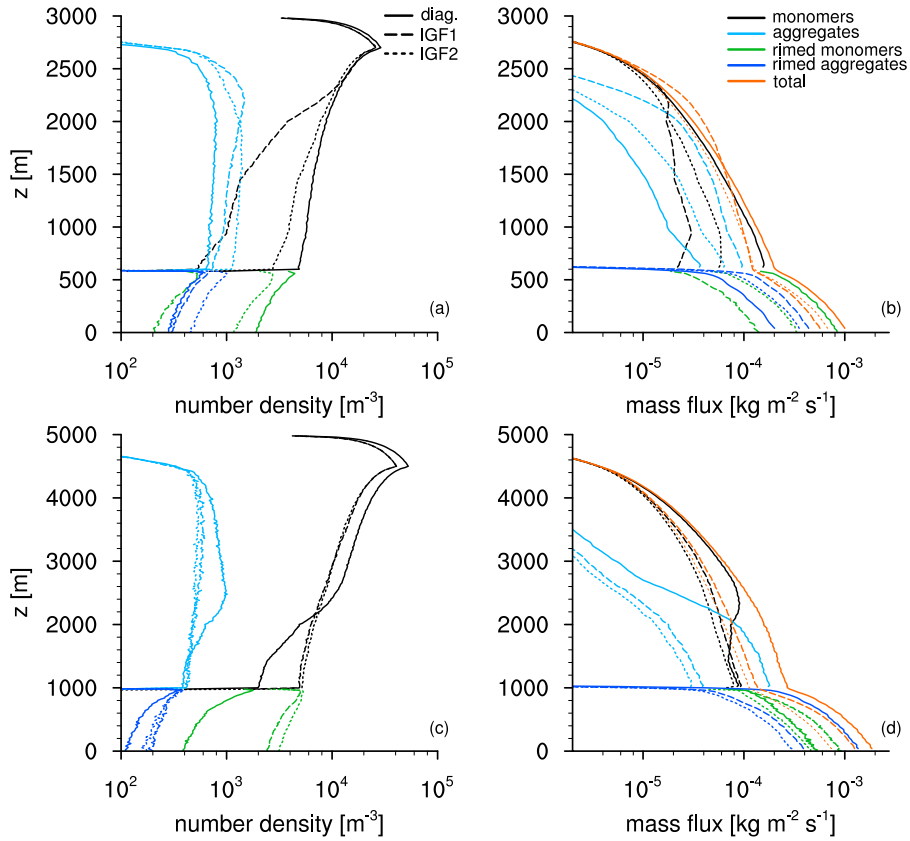


Figure 22. Vertical profiles of number density (a & c) and mass flux (b & d) for monomers (black), aggregates (black), rimed monomers (green), and rimed aggregates (dark blue) for the oblate (top row) and prolate nucleation regimes (bottom row) using a diagnostic geometry (solid), HP with original IGF (dashed), and HP with updated IGF (short-dashed) with all processes enabled.

745 in the LWZ be observed, because the cross-sectional area is more effectively changed by
 746 rounding when more pronounced ARs have developed.

747 6 Conclusion

748 The LPM *McSnow* has been expanded by an extended version of the habit prediction
 749 scheme of Jensen and Harrington (2015), based on the work of J.-P. Chen and Lamb
 750 (1994b). The comprehensive hydrodynamic description of porous spheroids by Böhm adds
 751 parameterizations regarding terminal velocity and collision efficiency. We propose a mass-
 752 dependent interpolation of the terminal velocity between prolate and cylindrical parti-
 753 cles based on the laboratory results of McCorquodale and Westbrook (2021), which over-
 754 comes the massive deceleration resulting from the cylindrical assumption of Böhm when
 755 transitioning from spherical to prolate or vice versa. A shape-dependent ventilation co-
 756 efficient has been introduced that combines the results of a collection of recent studies
 757 on ventilation of different geometries. While the effect on depositional growth is found
 758 to be in the range of a few percent for small particles, for larger particles the ventilation
 759 coefficients can increase by a factor of two compared to spheres. The habit prediction
 760 scheme in its original version was shown to be in good agreement with individual parti-
 761 cle measurements from Takahashi et al. (1991), but also has deficiencies, including the
 762 polycrystalline regime, the warm prolate maximum, and the branching criterion used for

763 oblate particles. A comparison with an independent method using the polarizability ra-
 764 tio of Myagkov, Seifert, Bauer-Pfundstein, and Wandinger (2016) confirmed these find-
 765 ings. Hence, we propose a modified version of the IGF combined with a modified branch-
 766 ing criterion. These modifications were found to improve the results under constant con-
 767 ditions in an appropriate way. The importance of explicit habit prediction for deposi-
 768 tion, aggregation and, in part, riming was demonstrated in a simplified 1-D snow shaft
 769 simulation. Columnar particles fall faster than their counterparts without explicit habits,
 770 and the shortened residence time leads to less ice mass, independent of the IGF config-
 771 uration. The reduced mass translates into rather weak aspect ratios and the resulting
 772 smaller cross-sectional areas significantly reduce the aggregation rate. However, riming
 773 is highly effective and partially enhances aggregation due to the assumed effective round-
 774 ing increasing the cross-sectional area. For the original IGF configuration, this effect is
 775 most pronounced because of the more pronounced ARs that develop due to the prolate
 776 maximum around the nucleation temperature.

777 The deposition rate of the plates is significantly increased compared to the m - D -
 778 particles for the original IGF at lower fall velocities, especially for large particles, result-
 779 ing in a higher mass flux. The planar geometry has a positive effect on the aggregation
 780 rate, with the opposite effect observed for prolates. The habit effect is partially mitigated
 781 when using the modified branching criterion: particles branch later, stay denser, accel-
 782 erate more, and grow slower than for the original IGF. In turn, the aggregation rates de-
 783 crease, but are still higher than when no habits are formed. It remains an open ques-
 784 tion when oblate particles branch, but the proposed approach showed reasonable results.
 785 Future laboratory studies could be aimed at understanding the deposition behavior un-
 786 der unfavorable habit conditions e.g. oblate particles growing in an environment that
 787 favors prolate growth.

788 Finally, large LWCs rapidly transform planar crystals into rimed particles once they
 789 reach the onset of riming. If the threshold is already exceeded when entering the LWZ,
 790 we do not find a significant effect of habit prediction on riming rates.

791 Given the importance of ice-microphysical processes in mixed-phase clouds, ice habits
 792 are highly influential and affect cloud lifetime. The variability of atmospheric conditions
 793 shapes individual particles whose characteristics cannot be generalized by broad clas-
 794 sifications. The chosen 1-D scenarios can only describe parts of the impact of an explicit
 795 habit prediction on process rates, but they already emphasize that it is of first order. By
 796 design, the setup does not allow the atmosphere to change dynamically, but these effects
 797 should play a role in the competition for water vapor and ultimately alter precipitation
 798 rates. More sophisticated atmospheric simulations could be set up to try to reproduce
 799 the interactions between different habits that are present simultaneously. Coupling *Mc-*
 800 *Snow* with the ICON model (Zängl et al., 2015) is a next step in achieving such realis-
 801 tic atmospheric simulations.

802 In addition, the detailed information on particle properties shall be compared with
 803 polarimetric measurements to show the validity of the model and to be used as a numer-
 804 ical laboratory to study microphysical processes in clouds.

805 Appendix A Böhm's theory

806 In the following, the reader can find the sets of equations of Böhm's theory to cal-
 807 culate the terminal velocity and collision efficiency using BLT.

808 A1 Terminal fall velocity

809 For both oblate and prolate particles, Böhm defines the characteristic length scale
 810 as the equatorial diameter $d_{\text{char}} = 2a$ instead of the maximum dimension (also men-

811 tioned by (Shima et al., 2020)).

$$X(m, \phi, q) = \frac{8 m_i g \rho_a}{\pi \mu^2 \max(\phi; 1) \max(q^{1/4}; q)}, \quad (\text{A1a})$$

$$k(\phi) = \min \left(\max(0.82 + 0.18 \phi; 0.85); \left(0.37 + \frac{0.63}{\phi} \right); \frac{1.33}{\max(\log \phi; 0) + 1.19} \right), \quad (\text{A1b})$$

$$\Gamma_\phi = \max \left(1; \min(1.98; 3.76 - 8.41 \phi + 9.18 \phi^2 - 3.53 \phi^3) \right), \quad (\text{A1c})$$

$$C_{\text{DP,S}} = \max \left(0.292 k \Gamma_\phi; 0.492 - \frac{0.2}{\sqrt{\phi}} \right), \quad (\text{A1d})$$

$$C_{\text{DP}} = \max \left(1; q(1.46q - 0.46) \right) C_{\text{DP,S}}, \quad (\text{A1e})$$

$$C'_{\text{DP}} = C_{\text{DP}} \frac{1 + (X/X_0)^2}{1 + 1.6(X/X_0)^2}, \quad \text{with } X_0 = \begin{cases} 2.8 \times 10^6, & \text{ice particles,} \\ 6.7 \times 10^6, & \text{water particles,} \end{cases} \quad (\text{A1f})$$

$$C_{\text{D0}} = 4.5 k^2 \max(\phi; 1), \quad (\text{A1g})$$

$$\beta = \left[1 + \frac{C_{\text{D0}} - C_{\text{DP}}}{6k} \left(\frac{X'}{C'_{\text{DP}}} \right)^{1/2} \right]^{1/2} - 1, \quad (\text{A1h})$$

$$\gamma = \frac{C_{\text{D0}} - C_{\text{DP}}}{4 C_{\text{DP}}}, \quad (\text{A1i})$$

$$N_{\text{Re}} = \frac{6k}{C'_{\text{DP}}} \beta^2 \left[1 + \frac{2\beta e^{-\beta\gamma}}{(2+\beta)(1+\beta)} \right], \quad (\text{A1j})$$

$$C_{\text{DI}} = \frac{X}{N_{\text{Re}}^2} - \frac{24k}{N_{\text{Re}}}, \quad (\text{A1k})$$

$$v_t = \frac{\mu N_{\text{Re}}}{\rho_a d_{\text{char}}}. \quad (\text{A1l})$$

812 The used variables are the Best number X , the turbulence modified Best number X' ,
 813 the dynamic viscosity μ , the air density ρ_a , the viscous shape parameter k , a function
 814 regarding the aspect ratio Γ_ϕ , the drag coefficient $C_{\text{DP,S}}$, the drag coefficient fitted for
 815 prolates C_{DP} , the Oseen drag coefficient C_{D0} , the inertial drag coefficient C_{DI} , the char-
 816 acteristic length scale d_{char} , and some helper variables β, γ . The minimum and maximum
 817 functions are used to constrain transitions from very oblate over quasi-spherical to very
 818 prolate particles. For more details on the derivation, the reader is referred to Böhm (1989)
 819 and Böhm (1992a). The middle term of formula A1c is found with and without the square
 820 root of the aspect ratio in the denominator (see Eq. 13 in (Böhm, 1992a) and Eq. 9 in
 821 (Böhm, 1999)). Analysis indicates that for a consistent transition the version from Böhm
 822 (1992a) should be correct while differences are marginal.

823 A2 Collision efficiency

$$F = \sqrt{G^2 + \frac{C_{\text{I},1} v_{\text{I1}}^2}{C_{\text{DI}}^* |v_1 - v_2|^2}}, \quad (\text{A2a})$$

$$G = \frac{6 \mu_a}{\rho_a r^* |v_1 - v_2| C_{\text{DI}}^*}, \quad (\text{A2b})$$

$$H = \frac{2m^*}{\rho_a \pi r^{*2} C_{\text{DI}}^* \delta}, \quad (\text{A2c})$$

$$v_{\text{I1}} = \frac{2+j}{4} v_1. \quad (\text{A2d})$$

$$(\text{A2e})$$

C_{DI}^* is the inertial drag coefficient with respect to r^* and the initial velocity while $C_{\text{I},1}$ refers to the bigger particle properties. While the latter is determined by Eq. A1l, C_{DI}^* is found by Eq. A1f-g and

$$C_{\text{DI}}^* = C'_{\text{DP}} \left(1 + \frac{4}{\beta} (1 - e^{-\gamma\beta}) \right), \quad (\text{A3})$$

824 to match the value of C_{DI} with the value from Oseen theory at low Reynolds numbers.

825 The two-body system is characterized by the radius r^* , mass m^* , area of intersec-
826 tion A^* , initial velocity v^* , and boundary layer thickness δ_s^*

$$r^* = \frac{r_1 r_2}{r_1 + r_2} = \sqrt{A^*/\pi}, \quad (\text{A4a})$$

$$m^* = \frac{m_1 m_2}{m_1 + m_2}, \quad (\text{A4b})$$

$$A^* = \pi r^{*2} = \frac{A_1 A_2}{\pi (r_{e1} + r_{e2})}, \quad (\text{A4c})$$

$$v^* = \max(|v_1 - v_2|; v_{\min}), \quad (\text{A4d})$$

$$\delta_s^* = \delta_{s1} \sqrt{v_1/v^*} + \delta_{s2} \sqrt{v_2/v^*}. \quad (\text{A4e})$$

827 For v^* , a minimum value is assumed ($v_{\min} = 10^{-10} \text{ m s}^{-1}$) because for equally fast par-
828 ticles the difference would approach zero, leading to a division by zero in Eq. A2a and
829 A2b.

In the case of an oblate particle, the equivalent circular radius r_e is the equatorial radius r but for prolate particles the definition changes to

$$r_e = \left(\frac{4\phi}{\pi} \right)^{1/2} r_1, \quad (\text{A5})$$

830 following the special assumptions of columns to be better approximated by a cylindri-
831 cal shape. In Böhm (1999), he also especially mentions that in case of columns or irreg-
832 ularly shaped aggregates the equivalent circular definition shall be used. In a general-
833 ized form for all particle shapes they can be written as

$$r_e = \sqrt{A/\pi}, \quad (\text{A6a})$$

$$\phi_e = \min(\phi; 1) \frac{r}{r_e}, \quad (\text{A6b})$$

$$q_e = \begin{cases} \pi q/4, & q > 1, \\ q, & q \leq 1, \end{cases} = q \left[1 - \frac{\max(q-1; 0)}{q-1} \left(1 - \frac{\pi}{4} \right) \right]. \quad (\text{A6c})$$

To fully define the shape characteristics of the two-body system, we additionally need to give definitions of the equivalent aspect ratio and porosity. Simple averaging of these quantities might lead to strong over- or underestimation. Hence, we use the radius weighted mean of those characteristics (Böhm, 1999)

$$\xi^* = r^* \left(\frac{\xi_1}{r_{e1}} + \frac{\xi_2}{r_{e2}} \right) \quad (\xi = q, \phi), \quad (\text{A7})$$

834 where the indices refer to the corresponding particle.

For anisotropic particles, the velocity v_1 has to be replaced by a characteristic velocity

$$v'_1 = \begin{cases} \phi_1 v_1 & , \text{for plates,} \\ \frac{3}{4} v_1 & , \text{for columns.} \end{cases} \quad (\text{A8})$$

835 Variables used in the flow correction for potential flow are defined as

$$t_\delta = \begin{cases} \frac{c_y}{\Delta_y} \arctan \frac{\Delta_y}{b c_y - 1}, & (b c_y \geq 1), \\ \frac{c_y}{\Delta_y} (\pi - \arctan \frac{\Delta_y}{1 - b c_y}), & (\frac{1}{2} < b c_y < 1), \end{cases} \quad (\text{A9a})$$

$$c_i = \frac{m_2}{3 k_{2,i} \pi r_2 \eta_a} \quad (i = x, y), \quad (\text{A9b})$$

$$b = \frac{3v}{r_{e,1} \delta_1}, \quad (\text{A9c})$$

$$\Delta_x = \sqrt{2b c_x / j + 1}, \quad (\text{A9d})$$

$$\Delta_y = \sqrt{2b c_y - 1}. \quad (\text{A9e})$$

The shape factor $k_{2,x}$ does not describe the same quantity as in Eq. A1c because this is defined perpendicular to the axis of symmetry in case of a plate or as the arithmetic mean

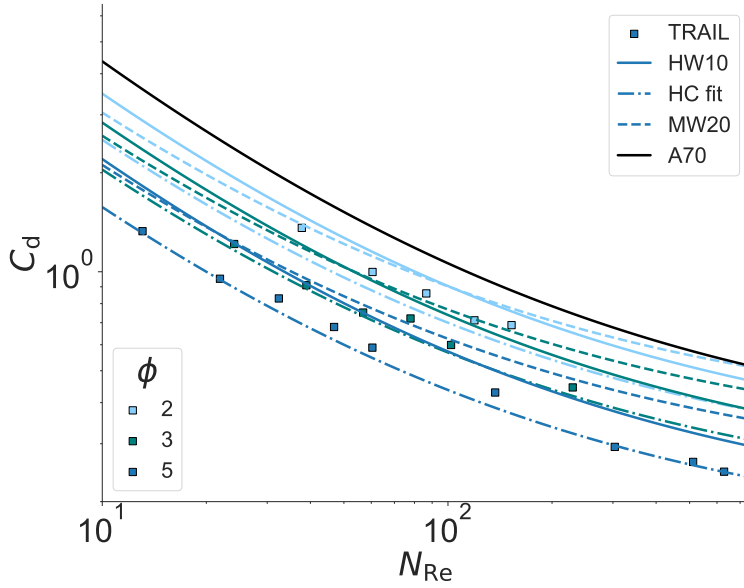


Figure A1. Fits for the N_{Re} - C_d -relations compared with data of hexagonal columns from TRAIL (colored squares). Black line corresponds to the solution of spheres by Abraham (1970, A70), solid lines are the generalized relation of A. J. Heymsfield and Westbrook (2010, HW10), dashed lines mark results of McCorquodale and Westbrook (2021, MW20), and dash-dotted lines show our fit for hexagonal columns (HC) only. The assumed aspect ratio is color coded

of the two shape factors parallel and perpendicular to the axis for a column. It can be approximated by

$$k_{2,x} \approx \begin{cases} 0.57 + 0.43\phi, & (\phi < 1), \\ k^{1.15}, & (\phi > 1). \end{cases} \quad (\text{A10})$$

836

A3 Shape assumption for columns

837

Figure A1 shows fits of Eq. 30 of Abraham (1970, A70), A. J. Heymsfield and Westbrook (2010, HW10), McCorquodale and Westbrook (2021, MW20), and our fit (HC fit) compared against the TRAIL data for hexagonal columns.

839

840

Appendix B Open Research

841

McSnow is part of the ICON modeling framework and the code is available under two different licenses: A personal non-commercial scientific license, and an institutional license that requires a cooperation agreement with DWD. More details on the licenses and an instruction how to obtain the ICON code can be found at <https://code.mpimet.mpg.de/projects/iconpublic>. Access to the McSnow repository can be granted on request as soon as an ICON license agreement has been signed. Data and post-processing script are available from Zenodo at <https://doi.org/10.5281/zenodo.7900348>. The repository includes a modified copy of the data from McCorquodale and Westbrook (2021) found in the "Supporting Information" section]TRAIL2021b.

849

Acknowledgments

The in-depth analysis of the Böhm parameterization would not have been so fruitful without the data set of the TRAIL campaign. We, therefore, like to thank Christopher D. Westbrook for sharing the data and providing insight. Furthermore, we would like to thank Alexander Myagkov for sharing the routines used to calculate the polarizability ratio from shape and density. This work has been funded by the German Science Foundation (DFG) under grant SE 1784/3-1, project ID 408011764 as part of the DFG priority program SPP 2115 on radar polarimetry.

References

- Abraham, F. F. (1970). Functional dependence of drag coefficient of a sphere on reynolds number. *The Physics of Fluids*, *13*(8), 2194-2195. Retrieved from <https://aip.scitation.org/doi/abs/10.1063/1.1693218> doi: 10.1063/1.1693218
- Auer, A. H., & Veal, D. L. (1970). The dimension of ice crystals in natural clouds. *J. Atmos. Sci.*, *27*(6), 919 - 926. Retrieved from https://journals.ametsoc.org/view/journals/atsc/27/6/1520-0469_1970_027_0919_tdoici_2_0_co_2.xml doi: 10.1175/1520-0469(1970)027<0919:TDOICI>2.0.CO;2
- Bailey, M. P., & Hallett, J. (2009, 9). A comprehensive habit diagram for atmospheric ice crystals: Confirmation from the laboratory, airs ii, and other field studies. *J. Atmos. Sci.*, *66*, 2888-2899. Retrieved from <http://journals.ametsoc.org/doi/abs/10.1175/2009JAS2883.1> doi: 10.1175/2009JAS2883.1
- Baran, A. J. (2012). From the single-scattering properties of ice crystals to climate prediction: A way forward. *Atmos. Res.*, *112*, 45 - 69. Retrieved from <http://www.sciencedirect.com/science/article/pii/S0169809512001160> doi: 10.1016/j.atmosres.2012.04.010
- Beard, K. V. (1980). The effects of altitude and electrical force on the terminal velocity of hydrometeors. *J. Atmos. Sci.*, *37*(6), 1363 - 1374. Retrieved from https://journals.ametsoc.org/view/journals/atsc/37/6/1520-0469_1980_037_1363_teoaae_2_0_co_2.xml doi: 10.1175/1520-0469(1980)037<1363:TEOAAE>2.0.CO;2
- Brdar, S., & Seifert, A. (2018). Mcsnow: A monte-carlo particle model for riming and aggregation of ice particles in a multidimensional microphysical phase space. *J. Adv. Model Earth Sy.*, *10*(1), 187-206. Retrieved from <https://agupubs.onlinelibrary.wiley.com/doi/abs/10.1002/2017MS001167> doi: 10.1002/2017MS001167
- Bringi, V., Seifert, A., Wu, W., Thurai, M., Huang, G. J., & Siewert, C. (2020, 8). Hurricane dorian outer rain band observations and 1d particle model simulations: A case study. *Atmosphere*, *11*, 879. Retrieved from <https://www.mdpi.com/2073-4433/11/8/879/htm> doi: 10.3390/ATMOS11080879
- Böhm, J. P. (1989). A general equation for the terminal fall speed of solid hydrometeors. *J. Atmos. Sci.*, *46*(15), 2419-2427. Retrieved from [https://doi.org/10.1175/1520-0469\(1989\)046<2419:AGEFTT>2.0.CO;2](https://doi.org/10.1175/1520-0469(1989)046<2419:AGEFTT>2.0.CO;2) doi: 10.1175/1520-0469(1989)046<2419:AGEFTT>2.0.CO;2
- Böhm, J. P. (1990). *On the hydrodynamics of cloud and precipitation particles* (Doctoral dissertation, ETH Zurich). doi: 10.3929/ethz-a-000578177
- Böhm, J. P. (1992a). A general hydrodynamic theory for mixed-phase microphysics. part i: drag and fall speed of hydrometeors. *Atmos. Res.*, *27*(4), 253 - 274. Retrieved from <http://www.sciencedirect.com/science/article/pii/S0169809592900359> doi: 10.1016/0169-8095(92)90035-9
- Böhm, J. P. (1992b). A general hydrodynamic theory for mixed-phase microphysics. part ii: collision kernels for coalescence. *Atmos. Res.*, *27*(4), 275 - 290. Retrieved from <http://www.sciencedirect.com/science/article/pii/S0169809592900359>

- 016980959290036A doi: 10.1016/0169-8095(92)90036-A
- 903 Böhm, J. P. (1992c). A general hydrodynamic theory for mixed-phase micro-
 904 physics. part iii: Riming and aggregation. *Atmos. Res.*, 28(2), 103 - 123.
 905 Retrieved from [http://www.sciencedirect.com/science/article/pii/](http://www.sciencedirect.com/science/article/pii/0169809592900234)
 906 0169809592900234 doi: 10.1016/0169-8095(92)90023-4
- 907 Böhm, J. P. (1994). Theoretical collision efficiencies for riming and aerosol
 908 impaction. *Atmos. Res.*, 32(1), 171 - 187. Retrieved from [http://](http://www.sciencedirect.com/science/article/pii/0169809594900582)
 909 www.sciencedirect.com/science/article/pii/0169809594900582 doi:
 910 10.1016/0169-8095(94)90058-2
- 911 Böhm, J. P. (1999). Revision and clarification of “a general hydrodynamic theory
 912 for mixed-phase microphysics”. *Atmos. Res.*, 52(3), 167 - 176. Retrieved from
 913 <http://www.sciencedirect.com/science/article/pii/S0169809599000332>
 914 doi: 10.1016/S0169-8095(99)00033-2
- 915 Böhm, J. P. (2004). Reply to comment on “revision and clarification of ‘a gen-
 916 eral hydrodynamic theory for mixed-phase microphysics’ [böhm j.p., 1999,
 917 *atmos. res.* 52, 167–176]”. *Atmos. Res.*, 69(3), 289 - 293. Retrieved from
 918 <http://www.sciencedirect.com/science/article/pii/S016980950300125X>
 919 doi: 10.1016/j.atmosres.2003.10.001
- 920 Chen, J.-P., & Lamb, D. (1994a, 09). Simulation of Cloud Microphysical and Chem-
 921 ical Processes Using a Multicomponent Framework. Part I: Description of the
 922 Microphysical Model. *J. Atmos. Sci.*, 51(18), 2613-2630. Retrieved from
 923 [https://doi.org/10.1175/1520-0469\(1994\)051<2613:SOCMAC>2.0.CO;2](https://doi.org/10.1175/1520-0469(1994)051<2613:SOCMAC>2.0.CO;2)
 924 doi: 10.1175/1520-0469(1994)051(2613:SOCMAC)2.0.CO;2
- 925 Chen, J.-P., & Lamb, D. (1994b). The theoretical basis for the parameterization
 926 of ice crystal habits: Growth by vapor deposition. *J. Atmos. Sci.*, 51(9), 1206-
 927 1222. Retrieved from [https://doi.org/10.1175/1520-0469\(1994\)051<1206:](https://doi.org/10.1175/1520-0469(1994)051<1206:TTBFTP>2.0.CO;2)
 928 [TTBFTP>2.0.CO;2](https://doi.org/10.1175/1520-0469(1994)051<1206:TTBFTP>2.0.CO;2) doi: 10.1175/1520-0469(1994)051(1206:TTBFTP)2.0.CO;2
- 929 Chen, Y., Jiang, P., Xiong, T., Wei, W., Fang, Z., & Wang, B. (2021, 11). Drag and
 930 heat transfer coefficients for axisymmetric nonspherical particles: A lbm study.
 931 *Chem. Eng. J.*, 424, 130391. doi: 10.1016/J.CEJ.2021.130391
- 932 Connolly, P. J., Emersic, C., & Field, P. R. (2012). A laboratory investigation into
 933 the aggregation efficiency of small ice crystals. *Atmos. Chem. Phys.*, 12, 2055-
 934 2076. doi: 10.5194/acp-12-2055-2012
- 935 Dias Neto, J., Kneifel, S., Ori, D., Trömel, S., Handwerker, J., Bohn, B., ... Sim-
 936 mer, C. (2019). The triple-frequency and polarimetric radar experiment for
 937 improving process observations of winter precipitation. *Earth Syst. Sci. Data*,
 938 11(2), 845–863. Retrieved from [https://essd.copernicus.org/articles/](https://essd.copernicus.org/articles/11/845/2019/)
 939 [11/845/2019/](https://essd.copernicus.org/articles/11/845/2019/) doi: 10.5194/essd-11-845-2019
- 940 Dziekan, P., Waruszewski, M., & Pawlowska, H. (2019, 7). University of warsaw
 941 lagrangian cloud model (uwlcm) 1.0: a modern large-eddy simulation tool for
 942 warm cloud modeling with lagrangian microphysics. *Geosci. Model Dev.*, 12,
 943 2587-2606. Retrieved from [https://www.geosci-model-dev.net/12/2587/](https://www.geosci-model-dev.net/12/2587/2019/)
 944 [2019/](https://www.geosci-model-dev.net/12/2587/2019/) doi: 10.5194/gmd-12-2587-2019
- 945 Field, P. R., Hogan, R. J., Brown, P. R. A., Illingworth, A. J., Choulaton, T. W.,
 946 Kaye, P. H., ... Greenaway, R. (2004). Simultaneous radar and aircraft ob-
 947 servations of mixed-phase cloud at the 100 m scale. *Q. J. Roy. Meteor. Soc.*,
 948 130(600), 1877-1904. Retrieved from [https://rmets.onlinelibrary.wiley](https://rmets.onlinelibrary.wiley.com/doi/abs/10.1256/qj.03.102)
 949 [.com/doi/abs/10.1256/qj.03.102](https://rmets.onlinelibrary.wiley.com/doi/abs/10.1256/qj.03.102) doi: 10.1256/qj.03.102
- 950 Fukuta, N. (1969). Experimental studies on the growth of small ice crys-
 951 tals. *J. Atmos. Sci.*, 26(3), 522-531. Retrieved from [https://doi.org/](https://doi.org/10.1175/1520-0469(1969)026<0522:ESOTGO>2.0.CO;2)
 952 [10.1175/1520-0469\(1969\)026<0522:ESOTGO>2.0.CO;2](https://doi.org/10.1175/1520-0469(1969)026<0522:ESOTGO>2.0.CO;2) doi: 10.1175/
 953 1520-0469(1969)026(0522:ESOTGO)2.0.CO;2
- 954 Gavze, E., & Khain, A. (2022). Gravitational collision of small nonspheri-
 955 cal particles: Swept volumes of prolate and oblate spheroids in calm air.
 956 *J. Atmos. Sci.*, 79(6), 1493 - 1514. Retrieved from <https://journals>
- 957

- 958 .ametsoc.org/view/journals/atsc/79/6/JAS-D-20-0336.1.xml doi:
959 10.1175/JAS-D-20-0336.1
- 960 Hall, W. D., & Pruppacher, H. R. (1976). The survival of ice particles falling
961 from cirrus clouds in subsaturated air. *J. Atmos. Sci.*, *33*(10), 1995-2006.
962 Retrieved from [https://doi.org/10.1175/1520-0469\(1976\)033<1995:
963 TSOIPF>2.0.CO;2](https://doi.org/10.1175/1520-0469(1976)033<1995:TSOIPF>2.0.CO;2) doi: 10.1175/1520-0469(1976)033<1995:TSOIPF>2.0.CO;2
- 964 Harrington, J. Y., Moyle, A., Hanson, L. E., & Morrison, H. (2019). On
965 calculating deposition coefficients and aspect-ratio evolution in approx-
966 imate models of ice crystal vapor growth. *J. Atmos. Sci.*, *76*(6), 1609-
967 1625. Retrieved from <https://doi.org/10.1175/JAS-D-18-0319.1> doi:
968 10.1175/JAS-D-18-0319.1
- 969 Hashino, T., & Tripoli, G. J. (2007). The spectral ice habit prediction sys-
970 tem (ships). part i: Model description and simulation of the vapor de-
971 position process. *J. Atmos. Sci.*, *64*(7), 2210 - 2237. Retrieved from
972 <https://journals.ametsoc.org/view/journals/atsc/64/7/jas3963.1.xml>
973 doi: 10.1175/JAS3963.1
- 974 Heymsfield, A. (1972). Ice crystal terminal velocities. *J. Atmos. Sci.*, *29*,
975 1348-1357. Retrieved from [https://journals.ametsoc.org/view/
976 journals/atsc/29/7/1520-0469_1972_029_1348_ictv_2_0_co_2.xml](https://journals.ametsoc.org/view/journals/atsc/29/7/1520-0469_1972_029_1348_ictv_2_0_co_2.xml) doi:
977 10.1175/1520-0469(1972)029<1348:ICTV>2.0.CO;2
- 978 Heymsfield, A. J. (1978). The characteristics of graupel particles in north-
979 eastern colorado cumulus congestus clouds. *J. Atmos. Sci.*, *35*(2), 284-
980 295. Retrieved from [https://journals.ametsoc.org/doi/abs/10.1175/
981 1520-0469%281978%29035%3C0284%3ATCOGPI%3E2.0.CO%3B2](https://journals.ametsoc.org/doi/abs/10.1175/1520-0469%281978%29035%3C0284%3ATCOGPI%3E2.0.CO%3B2) doi: 10.1175/
982 1520-0469(1978)035<0284:TCOGPI>2.0.CO;2
- 983 Heymsfield, A. J., & Westbrook, C. D. (2010, 08). Advances in the Estimation of
984 Ice Particle Fall Speeds Using Laboratory and Field Measurements. *J. At-
985 mos. Sci.*, *67*(8), 2469-2482. Retrieved from [https://doi.org/10.1175/
986 2010JAS3379.1](https://doi.org/10.1175/2010JAS3379.1) doi: 10.1175/2010JAS3379.1
- 987 Jayaweera, K. O. L. F., & Cottis, R. E. (1969). Fall velocities of plate-like and
988 columnar ice crystals. *Q. J. Roy. Meteor. Soc.*, *95*(406), 703-709. Re-
989 trieved from [https://rmets.onlinelibrary.wiley.com/doi/abs/10.1002/
990 qj.49709540604](https://rmets.onlinelibrary.wiley.com/doi/abs/10.1002/qj.49709540604) doi: 10.1002/qj.49709540604
- 991 Jensen, A. A., & Harrington, J. Y. (2015). Modeling ice crystal aspect ratio evo-
992 lution during riming: A single-particle growth model. *J. Atmos. Sci.*, *72*(7),
993 2569-2590. Retrieved from <https://doi.org/10.1175/JAS-D-14-0297.1> doi:
994 10.1175/JAS-D-14-0297.1
- 995 Jensen, A. A., Harrington, J. Y., Morrison, H., & Milbrandt, J. A. (2017, 6). Pre-
996 dicting ice shape evolution in a bulk microphysics model. *J. Atmos. Sci.*, *74*,
997 2081-2104. Retrieved from [https://journals.ametsoc.org/view/journals/
998 atsc/74/6/jas-d-16-0350.1.xml](https://journals.ametsoc.org/view/journals/atsc/74/6/jas-d-16-0350.1.xml) doi: 10.1175/JAS-D-16-0350.1
- 999 Ji, W., & Wang, P. K. (1999). Ventilation coefficients for falling ice crystals in the
1000 atmosphere at low-intermediate reynolds numbers. *J. Atmos. Sci.*, *56*, 829-836.
1001 doi: 10.1175/1520-0469(1999)056<0829:VCFVIC>2.0.CO;2
- 1002 Karrer, M., Seifert, A., Ori, D., & Kneifel, S. (2021). Improving the representa-
1003 tion of aggregation in a two-moment microphysical scheme with statistics of
1004 multi-frequency doppler radar observations. *Atmos. Chem. Phys.*, *21*(22),
1005 17133-17166. Retrieved from [https://acp.copernicus.org/articles/21/
1006 17133/2021/](https://acp.copernicus.org/articles/21/17133/2021/) doi: 10.5194/acp-21-17133-2021
- 1007 Ke, C., Shu, S., Zhang, H., Yuan, H., & Yang, D. (2018, 2). On the drag coefficient
1008 and averaged nusselt number of an ellipsoidal particle in a fluid. *Powder Tech-
1009 nol.*, *325*, 134-144. doi: 10.1016/J.POWTEC.2017.10.049
- 1010 Kikuchi, K., Kameda, T., Higuchi, K., & Yamashita, A. (2013). A global classifica-
1011 tion of snow crystals, ice crystals, and solid precipitation based on observations
1012 from middle latitudes to polar regions. *Atmos. Res.*, *132-133*, 460-472. Re-

- 1013 trieved from [https://www.sciencedirect.com/science/article/pii/](https://www.sciencedirect.com/science/article/pii/S0169809513001841)
1014 S0169809513001841 doi: 10.1016/j.atmosres.2013.06.006
- 1015 Kintea, D. M., Roisman, I. V., Hauk, T., & Tropea, C. (2015, 9). Shape evolution of
1016 a melting nonspherical particle. *Physical Review E - Statistical, Nonlinear, and*
1017 *Soft Matter Physics*, 92. doi: 10.1103/PhysRevE.92.033012
- 1018 Kiwitt, T., Fröhlich, K., Meinke, M., & Schröder, W. (2022, 4). Nusselt correlation
1019 for ellipsoidal particles. *Int. J. Multiphas. Flow*, 149, 103941. doi: 10.1016/J
1020 .IJMULTIPHASEFLOW.2021.103941
- 1021 Kobayashi, T. (1961). The growth of snow crystals at low supersaturations. *Phi-*
1022 *los. Mag.*, 6(71), 1363-1370. Retrieved from [https://doi.org/10.1080/](https://doi.org/10.1080/14786436108241231)
1023 14786436108241231 doi: 10.1080/14786436108241231
- 1024 Korolev, A., & Isaac, G. (2003). Roundness and aspect ratio of particles in
1025 ice clouds. *J. Atmos. Sci.*, 60(15), 1795-1808. Retrieved from [https://](https://doi.org/10.1175/1520-0469(2003)060<1795:RAAROP>2.0.CO;2)
1026 doi.org/10.1175/1520-0469(2003)060<1795:RAAROP>2.0.CO;2 doi:
1027 10.1175/1520-0469(2003)060<1795:RAAROP>2.0.CO;2
- 1028 Lawson, R. P., Pilon, B., Baker, B., Mo, Q., Jensen, E., Pfister, L., & Bui, P.
1029 (2008). Aircraft measurements of microphysical properties of subvisible cir-
1030 rus in the tropical tropopause layer. *Atmos. Chem. Phys.*, 8(6), 1609–1620.
1031 Retrieved from <https://www.atmos-chem-phys.net/8/1609/2008/> doi:
1032 10.5194/acp-8-1609-2008
- 1033 Locatelli, J. D., & Hobbs, P. V. (1974). Fall speeds and masses of solid precipita-
1034 tion particles. *J. Geophys. Res.*, 79(15), 2185-2197. Retrieved from [https://](https://agupubs.onlinelibrary.wiley.com/doi/abs/10.1029/JC079i015p02185)
1035 agupubs.onlinelibrary.wiley.com/doi/abs/10.1029/JC079i015p02185
1036 doi: 10.1029/JC079i015p02185
- 1037 Martin, J. J., Wang, P. K., Pruppacher, H. R., & Pitter, R. L. (1981). Numerical
1038 study of the effect of electric charges on the efficiency with which planar ice
1039 crystals collect supercooled cloud drops. *J. Atmos. Sci.*, 38(11), 2462-2469.
1040 doi: 10.1175/1520-0469(1981)038<2462:ANSOTE>2.0.CO;2
- 1041 Matrosov, S. Y., Mace, G. G., Marchand, R., Shupe, M. D., Hallar, A. G., & Mc-
1042 cubbin, I. B. (2012, 8). Observations of ice crystal habits with a scan-
1043 ning polarimetric w-band radar at slant linear depolarization ratio mode.
1044 *J. Atmos. Ocean Tech.*, 29, 989-1008. Retrieved from [https://journals](https://journals.ametsoc.org/view/journals/atot/29/8/jtech-d-11-00131_1.xml)
1045 .ametsoc.org/view/journals/atot/29/8/jtech-d-11-00131_1.xml doi:
1046 10.1175/JTECH-D-11-00131.1
- 1047 McCorquodale, M. W., & Westbrook, C. D. (2021). Trail part 2: A comprehensive
1048 assessment of ice particle fall speed parametrisations. *Q. J. Roy. Meteor. Soc.*,
1049 147(734), 605-626. Retrieved from [https://rmets.onlinelibrary.wiley](https://rmets.onlinelibrary.wiley.com/doi/abs/10.1002/qj.3936)
1050 .com/doi/abs/10.1002/qj.3936 doi: 10.1002/qj.3936
- 1051 Melnikov, V., & Straka, J. M. (2013, 8). Axis ratios and flutter angles of cloud ice
1052 particles: Retrievals from radar data. *J. Atmos. Ocean Tech.*, 30, 1691-1703.
1053 Retrieved from [https://journals.ametsoc.org/view/journals/atot/30/8/](https://journals.ametsoc.org/view/journals/atot/30/8/jtech-d-12-00212_1.xml)
1054 jtech-d-12-00212_1.xml doi: 10.1175/JTECH-D-12-00212.1
- 1055 Milbrandt, J. A., Morrison, H., II, D. T. D., & Paukert, M. (2021). A triple-
1056 moment representation of ice in the predicted particle properties (p3) micro-
1057 physics scheme. *J. Atmos. Sci.*, 78(2), 439 - 458. Retrieved from [https://](https://journals.ametsoc.org/view/journals/atsc/78/2/jas-d-20-0084_1.xml)
1058 journals.ametsoc.org/view/journals/atsc/78/2/jas-d-20-0084_1.xml
1059 doi: 10.1175/JAS-D-20-0084.1
- 1060 Mitchell, D. L. (1988). Evolution of snow-size spectra in cyclonic storms. part i:
1061 Snow growth by vapor deposition and aggregation. *J. Atmos. Sci.*, 45, 3431-
1062 3451. doi: 10.1175/1520-0469(1988)045<3431:EOSSSI>2.0.CO;2
- 1063 Mitchell, D. L. (1996). Use of mass- and area-dimensional power laws for deter-
1064 mining precipitation particle terminal velocities. *J. Atmos. Sci.*, 53(12), 1710-
1065 1723. Retrieved from [https://doi.org/10.1175/1520-0469\(1996\)053<1710:](https://doi.org/10.1175/1520-0469(1996)053<1710:UOMAAD>2.0.CO;2)
1066 UOMAAD>2.0.CO;2 doi: 10.1175/1520-0469(1996)053<1710:UOMAAD>2.0.CO;
1067 2

- 1068 Mitra, S. K., Vohl, O., Ahr, M., & Pruppacher, H. R. (1990). A wind tun-
 1069 nel and theoretical study of the melting behavior of atmospheric ice par-
 1070 ticles. iv: Experiment and theory for snow flakes. *J. Atmos. Sci.*, *47*(5),
 1071 584 - 591. Retrieved from [https://journals.ametsoc.org/view/](https://journals.ametsoc.org/view/journals/atsc/47/5/1520-0469_1990_047_0584_awtats_2_0_co_2.xml)
 1072 journals/atsc/47/5/1520-0469_1990_047_0584_awtats_2_0_co_2.xml doi:
 1073 10.1175/1520-0469(1990)047<0584:AWTATS>2.0.CO;2
- 1074 Morrison, H., de Boer, G., Feingold, G., Harrington, J., Shupe, M. D., & Sulia, K.
 1075 (2012, 12). Resilience of persistent arctic mixed-phase clouds. *Nat. Geosci.*, *5*,
 1076 11-17. Retrieved from <https://www.nature.com/articles/ngeo1332> doi:
 1077 10.1038/ngeo1332
- 1078 Morrison, H., & Grabowski, W. W. (2008). A novel approach for represent-
 1079 ing ice microphysics in models: Description and tests using a kinematic
 1080 framework. *J. Atmos. Sci.*, *65*(5), 1528 - 1548. Retrieved from [https://](https://journals.ametsoc.org/view/journals/atsc/65/5/2007jas2491.1.xml)
 1081 journals.ametsoc.org/view/journals/atsc/65/5/2007jas2491.1.xml
 1082 doi: 10.1175/2007JAS2491.1
- 1083 Morrison, H., van Lier-Walqui, M., Fridlind, A. M., Grabowski, W. W., Harrington,
 1084 J. Y., Hoose, C., ... Xue, L. (2020). Confronting the challenge of model-
 1085 ing cloud and precipitation microphysics. *J. Adv. Model Earth Sy.*, *12*(8),
 1086 e2019MS001689. Retrieved from [https://agupubs.onlinelibrary.wiley](https://agupubs.onlinelibrary.wiley.com/doi/abs/10.1029/2019MS001689)
 1087 [.com/doi/abs/10.1029/2019MS001689](https://agupubs.onlinelibrary.wiley.com/doi/abs/10.1029/2019MS001689) doi: 10.1029/2019MS001689
- 1088 Myagkov, A., Seifert, P., Bauer-Pfundstein, M., & Wandinger, U. (2016, 2). Cloud
 1089 radar with hybrid mode towards estimation of shape and orientation of ice
 1090 crystals. *Atmos. Meas. Tech.*, *9*, 469-489. doi: 10.5194/AMT-9-469-2016
- 1091 Myagkov, A., Seifert, P., Wandinger, U., Bühl, J., & Engelmann, R. (2016, 8). Re-
 1092 lationship between temperature and apparent shape of pristine ice crystals
 1093 derived from polarimetric cloud radar observations during the accept cam-
 1094 paign. *Atmos. Meas. Tech.*, *9*, 3739-3754. doi: 10.5194/AMT-9-3739-2016
- 1095 Naumann, A. K., & Seifert, A. (2015). A lagrangian drop model to study warm rain
 1096 microphysical processes in shallow cumulus. *J. Adv. Model Earth Sy.*, *7*(3),
 1097 1136-1154. Retrieved from [https://agupubs.onlinelibrary.wiley.com/](https://agupubs.onlinelibrary.wiley.com/doi/abs/10.1002/2015MS000456)
 1098 [doi/abs/10.1002/2015MS000456](https://agupubs.onlinelibrary.wiley.com/doi/abs/10.1002/2015MS000456) doi: 10.1002/2015MS000456
- 1099 Nelson, J. (1998). Sublimation of ice crystals. *J. Atmos. Sci.*, *55*(5), 910-919.
 1100 Retrieved from [https://doi.org/10.1175/1520-0469\(1998\)055<0910:](https://doi.org/10.1175/1520-0469(1998)055<0910:SOIC>2.0.CO;2)
 1101 [SOIC>2.0.CO;2](https://doi.org/10.1175/1520-0469(1998)055<0910:SOIC>2.0.CO;2) doi: 10.1175/1520-0469(1998)055<0910:SOIC>2.0.CO;2
- 1102 Nelson, J. T., & Baker, M. B. (1996). New theoretical framework for studies
 1103 of vapor growth and sublimation of small ice crystals in the atmosphere.
 1104 *J. Geophys. Res.: Atmospheres*, *101*(D3), 7033-7047. Retrieved from
 1105 <https://agupubs.onlinelibrary.wiley.com/doi/abs/10.1029/95JD03162>
 1106 doi: 10.1029/95JD03162
- 1107 Nettesheim, J. J., & Wang, P. K. (2018, 9). A numerical study on the aerody-
 1108 namics of freely falling planar ice crystals. *J. Atmos. Sci.*, *75*, 2849-2865.
 1109 Retrieved from [https://journals.ametsoc.org/view/journals/atsc/75/9/](https://journals.ametsoc.org/view/journals/atsc/75/9/jas-d-18-0041.1.xml)
 1110 [jas-d-18-0041.1.xml](https://journals/ametsoc.org/view/journals/atsc/75/9/jas-d-18-0041.1.xml) doi: 10.1175/JAS-D-18-0041.1
- 1111 Oseen, C. W. (1927). *Neuere methoden und ergebnisse in der hydrodynamik*. Akad.
 1112 Verlagsgesellschaft Leipzig. Retrieved from [https://archive.org/details/in](https://archive.org/details/in.ernet.dli.2015.80409)
 1113 [.ernet.dli.2015.80409](https://archive.org/details/in.ernet.dli.2015.80409)
- 1114 Pinsky, M., Khain, A., & Shapiro, M. (2001). Collision efficiency of drops in a wide
 1115 range of reynolds numbers: Effects of pressure on spectrum evolution. *J. At-*
 1116 *mos. Sci.*, *58*(7), 742 - 764. Retrieved from [https://journals.ametsoc.org/](https://journals.ametsoc.org/view/journals/atsc/58/7/1520-0469_2001_058_0742_ceodia_2_0_co_2.xml)
 1117 [view/journals/atsc/58/7/1520-0469_2001_058_0742_ceodia_2_0_co_2.xml](https://journals/atsc/58/7/1520-0469_2001_058_0742_ceodia_2_0_co_2.xml)
 1118 doi: 10.1175/1520-0469(2001)058<0742:CEODIA>2.0.CO;2
- 1119 Pitter, R. L., Pruppacher, H. R., & Hamielec, A. E. (1974). A numerical
 1120 study of the effect of forced convection on mass transport from a thin
 1121 oblate spheroid of ice in air. *J. Atmos. Sci.*, *31*, 1058-1066. doi: 10.1175/
 1122 1520-0469(1974)031<1058:ANSOTE>2.0.CO;2

- 1123 Posselt, R., Simmel, M., & Wurzler, S. (2004). Comment on revision and clar-
 1124 ification of “a general hydrodynamic theory for mixed-phase microphysics”
 1125 [böhm, j.p., 1999, *atmos. res.* 52, 167–176]. *Atmos. Res.*, 69(3), 281 - 287.
 1126 Retrieved from [http://www.sciencedirect.com/science/article/pii/](http://www.sciencedirect.com/science/article/pii/S0169809503001248)
 1127 [S0169809503001248](http://www.sciencedirect.com/science/article/pii/S0169809503001248) doi: 10.1016/j.atmosres.2003.03.001
- 1128 Pruppacher, H., & Klett, J. (1997). *Microphysics of clouds and precipitation*.
 1129 Springer Netherlands. doi: 10.1007/978-0-306-48100-0
- 1130 Reinking, R. F. (1979). The onset and early growth of snow crystals by accretion
 1131 of droplets. *J. Atmos. Sci.*, 36, 870 - 881. Retrieved from [https://journals](https://journals.ametsoc.org/view/journals/atms/36/5/1520-0469.1979.036_0870_toaego_2_0_co_2.xml)
 1132 [.ametsoc.org/view/journals/atms/36/5/1520-0469.1979.036_0870_toaego](https://journals.ametsoc.org/view/journals/atms/36/5/1520-0469.1979.036_0870_toaego_2_0_co_2.xml)
 1133 [_2_0_co_2.xml](https://journals.ametsoc.org/view/journals/atms/36/5/1520-0469.1979.036_0870_toaego_2_0_co_2.xml) doi: 10.1175/1520-0469(1979)036<0870:TOAEGO>2.0.CO;2
- 1134 Schlamp, R., Pruppacher, H., & Hamielec, A. (1975). A numerical investi-
 1135 gation of the efficiency with which simple columnar ice crystals collide
 1136 with supercooled water drops. *J. Atmos. Sci.*, 32(12), 2330-2337. doi:
 1137 10.1175/1520-0469(1975)032<2330:ANIOTE>2.0.CO;2
- 1138 Sei, T., & Gonda, T. (1989). The growth mechanism and the habit change of ice
 1139 crystals growing from the vapor phase. *J. Cryst. Growth*, 94(3), 697-707.
 1140 Retrieved from [https://www.sciencedirect.com/science/article/pii/](https://www.sciencedirect.com/science/article/pii/0022024889900948)
 1141 [0022024889900948](https://www.sciencedirect.com/science/article/pii/0022024889900948) doi: 10.1016/0022-0248(89)90094-8
- 1142 Seifert, A., Leinonen, J., Siewert, C., & Kneifel, S. (2019). The geometry of rimed
 1143 aggregate snowflakes: A modeling study. *J. Adv. Model Earth Sy.*, 11(3), 712-
 1144 731. Retrieved from [https://agupubs.onlinelibrary.wiley.com/doi/abs/](https://agupubs.onlinelibrary.wiley.com/doi/abs/10.1029/2018MS001519)
 1145 [10.1029/2018MS001519](https://agupubs.onlinelibrary.wiley.com/doi/abs/10.1029/2018MS001519) doi: 10.1029/2018MS001519
- 1146 Sheridan, L. M. (2008). *Deposition coefficient, habit, and ventilation influences on*
 1147 *cirriform cloud properties* (Master’s thesis, Dept.of Meteorology, The Pennsyl-
 1148 vanian State University). Retrieved from [https://etda.libraries.psu.edu/](https://etda.libraries.psu.edu/catalog/8556)
 1149 [catalog/8556](https://etda.libraries.psu.edu/catalog/8556)
- 1150 Sheridan, L. M., Harrington, J. Y., Lamb, D., & Sulia, K. (2009). Influence of
 1151 ice crystal aspect ratio on the evolution of ice size spectra during vapor
 1152 depositional growth. *J. Atmos. Sci.*, 66(12), 3732-3743. Retrieved from
 1153 <https://doi.org/10.1175/2009JAS3113.1> doi: 10.1175/2009JAS3113.1
- 1154 Shima, S., Kusano, K., Kawano, A., Sugiyama, T., & Kawahara, S. (2009, 7). The
 1155 super-droplet method for the numerical simulation of clouds and precipitation:
 1156 a particle-based and probabilistic microphysics model coupled with a non-
 1157 hydrostatic model. *Q. J. Roy. Meteor. Soc.*, 135, 1307-1320. Retrieved from
 1158 <http://doi.wiley.com/10.1002/qj.441> doi: 10.1002/qj.441
- 1159 Shima, S., Sato, Y., Hashimoto, A., & Misumi, R. (2020). Predicting the mor-
 1160 phology of ice particles in deep convection using the super-droplet method:
 1161 development and evaluation of scale-sdm 0.2.5-2.2.0, -2.2.1, and -2.2.2. *Geosci.*
 1162 *Model Dev.*, 13(9), 4107–4157. Retrieved from [https://gmd.copernicus.org/](https://gmd.copernicus.org/articles/13/4107/2020/)
 1163 [articles/13/4107/2020/](https://gmd.copernicus.org/articles/13/4107/2020/) doi: 10.5194/gmd-13-4107-2020
- 1164 Sulia, K. J., & Harrington, J. Y. (2011, 11). Ice aspect ratio influences on
 1165 mixed-phase clouds: Impacts on phase partitioning in parcel models. *J.*
 1166 *Geophys. Res.: Atmospheres*, 116, 21309. Retrieved from [https://](https://onlinelibrary.wiley.com/doi/full/10.1029/2011JD016298)
 1167 onlinelibrary.wiley.com/doi/full/10.1029/2011JD016298[https://](https://onlinelibrary.wiley.com/doi/abs/10.1029/2011JD016298)
 1168 onlinelibrary.wiley.com/doi/abs/10.1029/2011JD016298[https://](https://agupubs.onlinelibrary.wiley.com/doi/10.1029/2011JD016298)
 1169 agupubs.onlinelibrary.wiley.com/doi/10.1029/2011JD016298 doi:
 1170 10.1029/2011JD016298
- 1171 Sutherland, W. (1893). Lii. the viscosity of gases and molecular force. *The*
 1172 *London, Edinburgh, and Dublin Philosophical Magazine and Journal of*
 1173 *Science*, 36(223), 507-531. Retrieved from [https://doi.org/10.1080/](https://doi.org/10.1080/14786449308620508)
 1174 [14786449308620508](https://doi.org/10.1080/14786449308620508) doi: 10.1080/14786449308620508
- 1175 Takahashi, T., Endoh, T., Wakahama, G., & Fukuta, N. (1991). Vapor diffusional
 1176 growth of free-falling snow crystals between -3 and -23°C. *J. Meteorol. Soc.*
 1177 *Jpn. Ser. II*, 69(1), 15-30. doi: 10.2151/jmsj1965.69.1_15

- 1178 Takahashi, T., & Fukuta, N. (1988). Supercooled cloud tunnel studies on the growth
1179 of snow crystals between -4 and -20°C. *J. Meteorol. Soc. Jpn. Ser. II*, *66*, 841-
1180 855. Retrieved from [https://www.jstage.jst.go.jp/article/jmsj1965/66/](https://www.jstage.jst.go.jp/article/jmsj1965/66/6/66_6.841/_article)
1181 [6/66_6.841/_article](https://www.jstage.jst.go.jp/article/jmsj1965/66/6/66_6.841/_article) doi: 10.2151/jmsj1965.66.6.841
- 1182 Tridon, F., Battaglia, A., Chase, R. J., Turk, F. J., Leinonen, J., Kneifel, S., ...
1183 Nesbitt, S. W. (2019). The microphysics of stratiform precipitation dur-
1184 ing olympex: Compatibility between triple-frequency radar and airborne
1185 in situ observations. *J. Geophys. Res.: Atmospheres*, *124*(15), 8764-8792.
1186 Retrieved from [https://agupubs.onlinelibrary.wiley.com/doi/abs/](https://agupubs.onlinelibrary.wiley.com/doi/abs/10.1029/2018JD029858)
1187 [10.1029/2018JD029858](https://agupubs.onlinelibrary.wiley.com/doi/abs/10.1029/2018JD029858) doi: 10.1029/2018JD029858
- 1188 Trömel, S., Simmer, C., Blahak, U., Blanke, A., Doktorowski, S., Ewald, F., ...
1189 Quaas, J. (2021). Overview: Fusion of radar polarimetry and numerical
1190 atmospheric modelling towards an improved understanding of cloud and
1191 precipitation processes. *Atmos. Chem. Phys.*, *21*(23), 17291-17314. Re-
1192 trieved from <https://acp.copernicus.org/articles/21/17291/2021/> doi:
1193 [10.5194/acp-21-17291-2021](https://acp.copernicus.org/articles/21/17291/2021/)
- 1194 Um, J., McFarquhar, G. M., Hong, Y. P., Lee, S.-S., Jung, C. H., Lawson, R. P., &
1195 Mo, Q. (2015). Dimensions and aspect ratios of natural ice crystals. *Atmos.*
1196 *Chem. Phys.*, *15*(7), 3933-3956. Retrieved from [https://acp.copernicus](https://acp.copernicus.org/articles/15/3933/2015/)
1197 [.org/articles/15/3933/2015/](https://acp.copernicus.org/articles/15/3933/2015/) doi: 10.5194/acp-15-3933-2015
- 1198 von Terzi, L., Neto, J. D., Ori, D., Myagkov, A., & Kneifel, S. (2022, 9). Ice micro-
1199 physical processes in the dendritic growth layer: a statistical analysis combin-
1200 ing multi-frequency and polarimetric doppler cloud radar observations. *Atmos.*
1201 *Chem. Phys.*, *22*, 11795-11821. doi: 10.5194/ACP-22-11795-2022
- 1202 Wang, P. K. (2021). *Motions of ice hydrometeors in the atmosphere*. Springer Sin-
1203 gapore. Retrieved from [https://link.springer.com/10.1007/978-981-33-](https://link.springer.com/10.1007/978-981-33-4431-0)
1204 [-4431-0](https://link.springer.com/10.1007/978-981-33-4431-0) doi: 10.1007/978-981-33-4431-0
- 1205 Wang, P. K., & Ji, W. (2000, 04). Collision Efficiencies of Ice Crystals at
1206 Low-Intermediate Reynolds Numbers Colliding with Supercooled Cloud
1207 Droplets: A Numerical Study. *J. Atmos. Sci.*, *57*(8), 1001-1009. Re-
1208 trieved from [https://doi.org/10.1175/1520-0469\(2000\)057<1001:](https://doi.org/10.1175/1520-0469(2000)057<1001:CEOICA>2.0.CO;2)
1209 [CEOICA>2.0.CO;2](https://doi.org/10.1175/1520-0469(2000)057<1001:CEOICA>2.0.CO;2) doi: 10.1175/1520-0469(2000)057<1001:CEOICA>2.0.CO;2
- 1210 Westbrook, C. D., Hogan, R. J., Illingworth, A. J., Westbrook, C. D., Hogan,
1211 R. J., & Illingworth, A. J. (2008, 1). The capacitance of pristine ice crys-
1212 tals and aggregate snowflakes. *J. Atmos. Sci.*, *65*, 206-219. Retrieved from
1213 <http://journals.ametsoc.org/doi/abs/10.1175/2007JAS2315.1> doi:
1214 [10.1175/2007JAS2315.1](http://journals.ametsoc.org/doi/abs/10.1175/2007JAS2315.1)
- 1215 Westbrook, C. D., & Sephton, E. K. (2017). Using 3-d-printed analogues to inves-
1216 tigate the fall speeds and orientations of complex ice particles. *Geophys. Res.*
1217 *Lett.*, *44*(15), 7994-8001. Retrieved from [https://agupubs.onlinelibrary](https://agupubs.onlinelibrary.wiley.com/doi/abs/10.1002/2017GL074130)
1218 [.wiley.com/doi/abs/10.1002/2017GL074130](https://agupubs.onlinelibrary.wiley.com/doi/abs/10.1002/2017GL074130) doi: 10.1002/2017GL074130
- 1219 Whitaker, S. (1972, 3). Forced convection heat transfer correlations for flow in pipes,
1220 past flat plates, single cylinders, single spheres, and for flow in packed beds
1221 and tube bundles. *AIChE Journal*, *18*, 361-371. Retrieved from [https://](https://onlinelibrary.wiley.com/doi/full/10.1002/aic.690180219)
1222 onlinelibrary.wiley.com/doi/full/10.1002/aic.690180219[https://](https://onlinelibrary.wiley.com/doi/abs/10.1002/aic.690180219)
1223 onlinelibrary.wiley.com/doi/abs/10.1002/aic.690180219[https://](https://aiche.onlinelibrary.wiley.com/doi/10.1002/aic.690180219)
1224 aiche.onlinelibrary.wiley.com/doi/10.1002/aic.690180219 doi:
1225 [10.1002/AIC.690180219](https://aiche.onlinelibrary.wiley.com/doi/10.1002/aic.690180219)
- 1226 Woo, S. E., & Hamielec, A. E. (1971). A numerical method of determining the
1227 rate of evaporation of small water drops falling at terminal velocity in air. *J.*
1228 *Atmos. Sci.*, *28*, 1448-1454. doi: 10.1175/1520-0469(1971)028<1448:ANMODT>
1229 [2.0.CO;2](https://doi.org/10.1175/1520-0469(1971)028<1448:ANMODT>2.0.CO;2)
- 1230 Zängl, G., Reinert, D., Rípodas, P., & Baldauf, M. (2015). The icon (icosahed-
1231 ral non-hydrostatic) modelling framework of dvd and mpi-m: Descrip-
1232 tion of the non-hydrostatic dynamical core. *Q. J. Roy. Meteor. Soc.* doi:

